Powerline Perching with a Fixed-Wing UAV

by

Joseph L. Moore

Submitted to the Department of Mechanical Engineering
in partial fulfillment of the requirements for the degree of

Master of Science in Mechanical Engineering

at the

MASSACHUSETTS INSTITUTE OF TECHNOLOGY

June, 2011

Signature of Author ....
Joseph L. Moore
Department of Mechanical Engineering
May 6, 2011

Certified By ....
Russ Tedrake
X Consortium Associate Professor of EECS
Thesis Supervisor

Certified By ....
H. Harry Asada
Ford Professor of Mechanical Engineering
Thesis Reader

Accepted By ....
David E. Hardt
Chairman, Committee on Graduate Students

Powerline Perching with a Fixed-Wing UAV

by Joseph L. Moore

Submitted to the Department of Mechanical Engineering
on May 6, 2011
in partial fulfillment of the requirements for the degree of
Master of Science in Mechanical Engineering
at the
MASSACHUSETTS INSTITUTE OF TECHNOLOGY

Abstract

Small and micro UAVs have enabled a number of new mission capabilities, including navigating in and around buildings and performing perch-and-stare surveillance. However, one of the primary limitations of these small vehicles is endurance, simply because they cannot carry sufficient power for long missions. Recent advances in fixed-wing perching have made it possible to consider a new solution to this problem - landing on a powerline to recharge. Furthermore, because a current carrying conductor generates a magnetic field, a unique opportunity exists to use the powerline not just for recharging, but for localization as well.

In this thesis, we seek to develop technologies that will enable a fixed-wing aircraft to land on a powerline using only the powerline's magnetic field and an inertial measurement unit for localization. To achieve this goal, an experimental set-up and preliminary sensing hardware are developed to detect the magnetic field at least 4 meters from the wire. Then, the necessary signal processing and state estimation algorithms are applied to achieve successful localization and overcome problematic field ambiguities. Following this, an on-board sensing system is developed and the high speed tracking of a perching trajectory is demonstrated experimentally. Finally, the position error associated with the aircraft tracking algorithm is analyzed carefully and assessed to be suitable for achieving closed loop perching. The work culminates in a light weight, 30 gram, on-board sensor system with the capability of estimating the position of a perching aircraft in real time at update rates up to 320 Hz, positional accuracies ranging from 2 to 20 centimeters, and delays of about 17 ms.

Thesis Supervisor: Russ Tedrake
Title: X Consortium Associate Professor of EECS

Thesis Reader: H. Harry Asada
Title: Ford Professor of Mechanical Engineering

Acknowledgments

Over the past few years, there have been many people whose support has been crucial to the success of this thesis. I would first like to thank my thesis advisor, Russ Tedrake, for his unparalleled insight and steady encouragement over the duration of this project. His vision for the future of robotics and his love for science never ceases to inspire. Secondly, I would like to thank the other members of the Robot Locomotion Group, who through frequent discussions, and sometimes quarrels, have helped to push this work forward through many roadblocks. I would also like to thank Harry Asada for his helpful discussion on state estimation, as well as Jim Hoburg for his help with modeling magnetic fields and all the intricacies therein. In addition, I would like to thank the members of the Distributed Robotics Group for their assistance with printed circuit board layouts and other electrical hardware related issues. Perhaps most importantly, I would like to thank my wife, Kayleen, who has been with me every step of the way, spurring me on by both word and deed, even when it meant helping to solder circuit components. Finally, I would like to thank my parents as well as my grandparents, without on whose shoulders to stand, I would not be where I am today.

Chapter 1

Introduction

1.1 Motivations for Powerline Perching

For some time, a great deal of effort has gone into the development of Unmanned Aerial Vehicles (UAVs) for a wide variety of applications, from military surveillance to measuring atmospheric conditions. Typically, these UAVs have ranged in wingspan from 10 to 60 feet [12] and have operated in a narrow, linear flight regime. In recent years, however, there has been significant interest in small and micro UAVs. Such UAVs have demonstrated the potential to enable a number of new mission capabilities, including navigating in and around buildings, flying through forests, and performing perch-and-stare surveillance. However, these small UAVs possess a significant drawback when being used in the field- they are simply unable to carry sufficient power for long missions. For this reason, developing ways for these aircraft to increase their mission duration capabilities is crucial to the practical deployment of small-scale UAVs.

One approach to increasing such mission duration is by using energy that already exists in the environment to recharge, or power the UAV. Some of the initiatives that have pursued this line of research have focused on methods such as gust soaring [49], while others have sought to use solar panels to boost the flight capabilities of their aircraft[36, 9]. Although exhibiting some potential for increasing mission duration, these methods restrict themselves to naturally occurring sources of energy. Many times, however, other man-made energy sources are also available. For instance, in urban areas, powerlines provide a unique opportunity for harvesting energy from the environment either through inductive coupling or direct connection. In the past few years, some successful research initiatives have resulted in technologies which allow soldiers to efficiently acquire electricity from existing power grids[13]. Thus, if a small UAV could successfully land on a powerline, it could recharge while also conducting perch and stare surveillance.

The notion of landing on a powerline poses several interesting challenges in the areas control and estimation. The first, and perhaps most relevant task to this thesis, is locating the wire itself. There are two primary approaches one could take to achieve this goal -

camera based vision systems or magnetic field sensing. However, after the two approaches are compared, magnetic field based sensing seems to provide several key advantages over camera based systems.

First of all, even if sufficient computational resources are available onboard the aircraft, locating a powerline can be a daunting task for computer vision in visually cluttered environments. Magnetic field sensing, however, has an advantage, since powerlines already provide a magnetic beacon that stands out from its surrounding environment. Another short coming of camera based systems is that in many cases it is unfeasible to accurately estimate the distance to the powerline which, at the maneuver's initial conditions, may appear only as a few pixels in an onboard camera. In contrast, a powerline with 50-100 amps of current passing through it provides signals strengths around 10 mG at these initial positions, which is enough to get a sufficient state estimate. Frame rate is another enormous shortfall of today's onboard camera systems, which in many cases max out around 30 fps at the desired resolutions. This is not acceptable at all for the perching maneuver, which executes in under a second. The update rate of an analog magnetometer is only limited by the sensor's bandwidth, which in the context of this paper, is around 1 kHz. Last of all, carmeras require a line of sight to the source. One would either need multiple cameras, or a camera mount capable of servoing fast enough to track the perch during the high angle of attack aircraft maneuver. In the case of the magnetic field measurements, line of sight is clearly not a factor.

The second challenge posed by recharging a UAV on a powerline is the landing maneuver itself. For certain types of UAVs, one could imagine such a task being solved quite simply. For instance, a rotorcraft system which is fully actuated should be able to easily execute a nearly arbitrary trajectory to land on the wire. However, the use of such a rotorcraft system would seem to undermine the very nature of the original problem, that is, increasing the mission duration of small scale UAVs. It is well known that rotorcraft systems use substantially more power during flight than their fixed-wing counterparts. A better solution would be to use a fixed-wing UAV. However, executing a landing maneuver for such a system is extremely challenging, requiring a nonlinear control design to stabilize the aircraft at very high angles of attack.

Fortunately, over the past few years, a number of advances have been made in the area of fixed-wing perching [6, 15, 50, 51]. In [6], significant progress was made in modeling and controlling an underactuated glider at high angles of attack during a perching maneuver by using a Vicon motion capture system to close the feedback loop. It seems as though perching on a powerline using magnetic field sensing for inductive recharging would be a natural extension of this control technology.

For this reason, the goal of this thesis is to summarize the efforts undertaken to develop a magnetic field based sensing and estimation system capable of providing reliable position feedback for a perching UAV, and to compare its performance with the original Vicon-based state estimation.

1.2 Approach and Outline of the Thesis

At the beginning of the investigation, it was hypothesized that the magnetic fields generated by a powerline could be used to localize a fixed-wing aircraft during a perching maneuver. It was then determined that this hypothesis could be evaluated by asking four key research questions. They are as follows:

1. "Can the magnetic field be detected along the length of the perching trajectory?"
2. "Can the powerline's magnetic field model be used to obtain position measurements?"
3. "Can fixed wing perching still be achieved with the instrumented aircraft?"
4. "Can the aircraft be tracked accurately enough during a perching maneuver?"

It was determined that each of these questions could be answered through a series of systematic steps, using both experiments and simulations. These steps taken to answer these questions are defined in greater detail below.

1.2.1 Question 1: Sensor Range

In order to answer the question, "Can the magnetic field be detected along the length of the perching trajectory?", one must first define the perching maneuver itself.

Aircraft and Perching Maneuver Specifications

Figure 1.1: Experimental Foam Glider

The fixed-wing perching maneuver referenced in this thesis is the same as that defined in [6]. The fixed-wing aircraft, shown in Figure 1.1, is a foam glider weighing about 80 grams and possessing a wingspan of about 60 cm. The wings are reinforced with carbon fiber strips, and a hobby servo motor controls the aircraft's elevator, the only control surface on the vehicle. Through optimal control theory, an open-loop perching trajectory was developed, as depicted in Figure 1.2. This trajectory requires the aircraft to be launched at about 7 m/s approximately 3.5 meters from the perch. As the elevator deflects, the aircraft pitches upward and lands within a few centimeters of the perch.

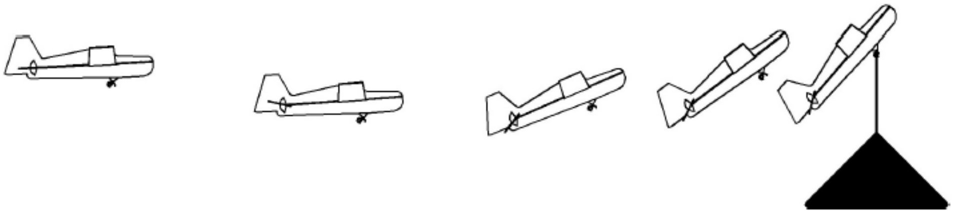

Figure 1.2: Fixed-Wing Perching Trajectory

Approach

In considering the dimensions of perching maneuver itself, it is evident that in order to address the first research question, as system capable of sensing magnetic field values at least 4 meters from the powerline will be required. In Chapter 3, an effort is made to move toward this goal by determining the properties of actual power lines. Then, in Chapter 4, these power line properties are used to develop an experimental indoor power line set-up with similar characteristics to those found in the field. In the same chapter, we then proceed to develop a preliminary sensor unit. Finally, in Chapter 5, we develop the signal processing methods necessary to detect the magnetic field's amplitude 4 meters from the wire.

1.2.2 Question 2: Magnetic Field Model

To answer the question, "Can a model of the powerline's magnetic field be used to obtain position measurements?", we develop a simple magnetic field model and seek to fuse measurements from a magnetometer and IMU to achieve position measurements. This is accomplished by developing and evaluating a magnetic field model through simulation in Chapter 8 and using state estimation methods to fuse sensor measurements in Chapter 7. Then, the state estimation methods are carried out on real data and compared to Vicon motion capture measurements.

1.2.3 Question 3: Modified Glider

The third question asked is, “Can fixed wing perching still be achieved with the instrumented aircraft?” Because the instrumented aircraft will be heavier, it is likely that the mass and inertia properties will change significantly. Furthermore, if the on board electronics are too heavy, the plane will be unable to perch at all. To address this question, in Chapter 10, we build a light-weight version of the system hardware, develop a new process model for the instrumented aircraft, and attempt to demonstrate fixed-wing perching in Chapter 11 with the heavier aircraft.

1.2.4 Question 4: High Speed Trajectory Tracking

The final question we must consider is, “Can the aircraft be tracked accurately enough during a perching maneuver.” In Chapter 12, we address this question by attempting to track the aircraft along an open-loop perching trajectory using the light-weight sensor module and compare the results to Vicon motion capture.

1.3 Contributions of this Thesis

This thesis makes a number of important contributions to field of sensing, state-estimation, and aircraft control. The first contribution is the development of hardware and signal processing methodologies to sense magnetic field signals down to a few hundred microVolts at rates above 500 Hz. Another contribution is the development of a state estimation formulation which allows the aircraft to be tracked through magnetic field measurement ambiguities. Furthermore, this thesis seeks to document the development of the practical, light weight sensing module used to estimate position measurements from magnetic field measurements on-board the aircraft. In addition to estimation, this thesis also makes some contributions to the modeling and control of an aircraft at high angles of attack. Last of all, this thesis describes some of the methods through which the experimental and theoretical findings presented can be generalized to the accommodate more complex scenarios which will arise when a UAV attempts to land on an actual outdoor powerline.

Chapter 2

Related Work

Before attempting to answer the research questions presented above, it is important to first review some of the work related to this thesis. Due to the interdisciplinary nature of this particular thesis, there is a substantial amount of previous work that exists as a foundation for the research contained in the following chapters. To limit the scope of this review, work will first be highlighted from four main areas - magnetic field sensing, state estimation, magnetic field modeling, and fixed-wing perching. Then, the use of magnetic fields in control and estimation will be examined. Hopefully these areas of past research will serve best to place this work in the context of history.

2.1 Magnetic Field Sensing

For almost two thousand years, mankind has sought to detect magnetic fields. Historical records indicate that the Chinese first noticed the directional qualities of loadstone with their "South Pointing Spoon" at the beginning of the first millennium [23]. By the end of the first millennium, the Chinese military had begun to use this compass technology to navigate on cloudy nights[27]. Not long after, it is hypothesized that this technology made its way to Europe, where the navigational compass was first mentioned in 1187 by Alexander Neckham of England[14]. Then, almost a hundred years later, in 1269, Pierre de Maricourt, also known as Peregrinus, wrote a letter to friend describing the properties of magnets as well as two novel compass designs [23]. Although this epistle is often seen as the first scientific treatise ever written, Peregrinus failed to provide a explanation as to why the loadstone aligns itself with the meridian, attributing the effect to some supernatural force of heaven[23]. Fortunately, a naturalistic explanation was finally provided in 1600 when William Gilbert published his scientific work "De Magnete" in which he hypothesized from a series of experiments that the earth itself was a giant loadstone and was responsible for the deflection of the compass needles[27].

Once it was discovered that the earth itself was producing a magnetic field, a whole new initiative to measure the strength of the earth's field began. The next great breakthrough in this area came in 1832, when Karl Friedrich Gauss and Wilhelm Eduard Weber collaborated to develop the first absolute magnetometer or ”magnometer”. Their device consisted of a bar magnet suspended by a wire from whose oscillations Guass could determine the absolute magnitude of the local magnetic field[23].

In the last century, nearly a hundred years after the development of the first magnetometer, a number of different types of magnetic field sensors have arisen to meet the needs of various applications. However, only those sensors categorized as ”Earth Field Sensors” (sensors which can measure from 1 microGauss to 10 Gauss) are relevant to this thesis. In this category, one will find that two primary types of sensors dominate the market.

The first type of sensor is known as the fluxgate magnetometer and was developed in the 1930s by Victor Vacquier at Gulf Research Laboratories[28]. This magnetometer consists of two coils wrapped around a ferromagnetic core. The primary coil drives the secondary coil through the core, which has the ability to change its inductive properties in the presence of external magnetic fields. If the inductive properties of the core do change, then the output signal on the secondary coil changes, providing one with the ability to sense the impact of an externally applied magnetic field.

The second type of ”Earth Field” magnetometer is the magnetoresistive sensor. These sensors exploit the magnetoresistive effect, or the tendency of some materials to change their resistance in the presence of a magnetic field. This property was was first discovered by Lord Kelvin in 1856 and can be observed in many thin film ferromagnetic materials such as Permalloy[4]. Oftentimes, these materials possess a preferred direction of magnetization which is parallel to the direction of current flow in the material. In the presence of a magnetic field, this magnetization direction will rotate away from the direction of current flow by an amount dependent on the amplitude of the applied field. Interestingly, as the material’s magnetization rotates away from the direction of the current, the amount electron scattering decreases in the material, which, in turn, also causes the material’s resistance to decrease. Such a decrease in resistance then causes a change in output voltage which can be easily measured to determine the magnitude of the applied magnetic field[24].

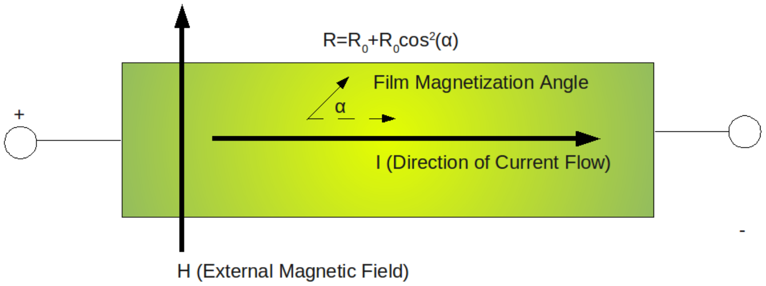

Figure 2.1: Diagram of Magnetoresistive Material

Both the fluxgate magnetometer and the magnetoresistive sensor have been used extensively in navigation and attitude control applications.

2.2 State Estimation

Like magnetic field sensing, state estimation is also a central component of this thesis. And, oddly enough, just like the early magnetometer, the foundation of state estimation can be traced back to Gauss, who, in 1795 when he was 18, developed the recursive least squares algorithm in his efforts to study planet and comet motion with data from telescopes[42]. Although Gauss's least squares formulation was independent of probability, in the early 1900s, techniques using probability to formulate the optimization problem began to emerge. In 1949 Norbert Wiener published his work on filtering, where he used Bayesian probability methods to develop an optimal finite impulse response filter[52]. Rudolph Kalman then went on in 1960 to build on Wiener's work by proposing a more generalized form of this filter which took into consideration non-stationary systems [22]. The filter assumes linear system dynamics and Gaussian noise distributions, however, it can be also be modified for nonlinear systems via the Extended Kalman Filter formulation.

For many, the Extended Kalman Filter exists as the major milestone in estimation techniques, and has certainly been used in numerous applications to track the position and orientation of a wide variety of bodies in flight, from autonomous aircraft, to missiles, to satellites and other spacecraft. With the practical success of the Kalman filter in the Apollo missions [40], the usefulness of recursive Bayesian estimation was clearly demonstrated. As time has gone on, a number of other recursive Bayesian estimation techniques have come to the forefront. One such method, known as the particle filter [11], keeps track of the probability distribution by propagating a large number of sample points through the system dynamics. This filter method does not require one to linearize nonlinear system dynamics or assume Gaussian noise distributions, and for this reason it can achieve better tracking performance by sacrificing computational efficiency. Another recursive Bayesian estimation technique, known as the Unscented Kalman Filter[21], serves as a half-way point between the computational complexity of the particle filter and the computational simplicity of the extended Kalman filter. By employing the unscented transform [20], the filter propagates a small number of "sigma" points through a system's dynamics and is able to recover the system mean and covariance. The Unscented Kalman Filter is more accurate for highly nonlinear systems than the Extended Kalman filter, but it still assumes a Gaussian probability distribution.

2.3 Magnetic Field Modeling

The drive to understand the nature of magnetic fields around current carrying conductors began when Hans Christian Oersted accidentally noticed a compass needle deflect when an electric current started flowing through a wire[23]. Although, this phenomenon was further investigated by both by Andre Marie Ampere and Michael Faraday, it was the mathematician James Clerk Maxwell who formulated the experimental findings of electricity and magnetism into a mathematical framework[23]. Ampere's Law, as shown in the equation below, is perhaps the most useful of these equations for modeling the magnetic field around a current carrying conductor.

$$\oint \mathbf{B} \cdot d\mathbf{l} = \mu_0 I_{enc} \tag{2.1}$$

However, it is difficult to use Ampere's law to model a current carrying conductor of arbitrary shape. For this, one must employ the Biot-Savart Law, which allows one to compute the static magnetic field generated by an infinitesimal section of wire. Recently, due the allegations made of health risks associated with extremely low frequency (ELF) mangetic fields, a number of researchers have begun using the Biot-Savart law to model the magnetic fields found around powerlines. In [10], the author has developed a flexible code to compute the magnetic field around arbitrary conductor configurations. In [25], the author explores in depth the impacts of sagging electrical conductors and seeks to use biot-savart laws to generate a more accurate magnetic model.

2.4 Fixed-Wing Perching

Over the last five or six years, there has been a substantial interest in the area of fixed wing perching. The ability to land autonomously in a confined space has been a task which has been beyond the capabilities of most conventional aircraft control systems.

At Cornell University, researchers have attempted to achieve fixed wing perching by the use of a platform with morphing wings [50, 51]. By rotating the wings down during the perching maneuver, the aircraft was able to maintain attached flow while using the drag of the pitched fuselage to slow down the vehicle. At Stanford, fixed wing perching has also been investigated [8]. By developing a novel spine technology, the researchers enabled the aircraft to perch robustly on rough vertical surfaces. Although clever approaches to solving the perching problem, both of these approaches avoided nonlinear nature of the high angle of attack landing maneuvers routinely executed by birds.

At MIT, researchers have developed a variety of tools, such as LQR Trees, for controlling complex nonlinear dynamics[43, 44, 37]. For this reason, MIT has taken a different approach to the perching problem by seeking to embrace the full nonlinear control to control a perching aircraft at very high angles of attack. For the past few years, research has been conducted to develop models for a fixed-wing aircraft[16, 6], as well as to stabilize the perching aircraft about an optimized trajectory[38, 7].

2.5 Control and Estimation using Magnetic Fields

Although there have been no efforts made to track an aircraft in a high angle of attack maneuver using magnetic field measurements, there has been a significant amount of work done to use magnetic field measurements obtained via magnetometers in feedback stabilization and estimation. In the beginning, magnetometers were first used on spacecraft to collect data on earth's magnetic field, and then, gradually, they were incorporated into feedback control. In [39], the author develops a closed loop control methodology which is able to recover a tumbling spacecraft based on magnetometer data. In [46], the author develops a magnetometer based control system to facilitate certain satellite maneuvers in space. Eventually, state estimation methods, such as the Kalman Filter, were applied to more accurately track the spacecraft using the earth's magnetic fields.[35]. As this spacecraft technology has advanced, it has been incorporated into UAVs, which have begun to utilize magnetometers for navigation in an effort to achieve more accurate heading measurements [26].

Surprisingly, only few a research initiatives have explored the navigational uses of magnetic fields other than those produced by the earth. One of these initiatives has taken place at MIT, where small magnetic dipoles were used to achieve collision avoidance within a group of UAVs through total field sensing[41]. Similarly, in [34], multiple Extremely Low Frequency (ELF) magnetic field beacons were used to localize a mobile robot in a factory setting. However, other than the work presented in [29] and [30], which describe the contents of this thesis, there has not been any work done involving the use of a powerline's magnetic field for UAV navigation.

Chapter 3

Powerline Class and Configuration

In addressing the question “Can the magnetic field be detected along the length of the perching trajectory?”, the first step was to consider the various types of powerlines used in the world’s power distribution grids. It was reasoned that by reviewing the different classes and configurations of powerlines that exist, a more accurate indoor experimental power-line set-up could be developed and used to test the feasibility of sensing magnetic field values at 4 meters from a current carrying wire.

3.1 Powerline Voltage Classes

In most power distribution grids, the powerlines can be divided into three main categories based on voltage. After electricity is generated by the power plant, it is stepped up to extremely high voltages. These high voltage lines, also known as transmission lines, carry electricity long distances at voltages from 69-765 kV [2].

Figure 3.1: High Voltage Transmission Lines (Source: Richard Williams, geograph.org.uk)

As with all power lines, the current through these lines varies with load. For instance, if there is a 10 MW load on a transmission line at 155 kV, the current through the wire will be about 64 A. The transmission lines typically run into a power substation where the voltage levels are stepped down . The first step down results in voltages between 34.5 and 69 kV, which are known as sub-transmission lines. Eventually, the subtransmission line voltages are stepped down again to distribution voltage levels, and carried on what are known as distribution lines [2].

Figure 3.2: Typical Distribution Lines

In many cases, distribution line voltage levels are between 12.5 and 24.9 kV, and can often permit high currents. For instance, a 10 kV distribution line serving a 1 MW load will produce 100 Amps of current. Finally, to deliver power from the distribution lines to individual residences, a transformer is used to create a 240 volt service line [2]. Of the three main power-line voltage classes - transmission, distribution, and service - distribution lines seem to possess the best characteristics for inductive recharging, since they often conduct the highest currents. High currents also generate the largest magnetic fields, and for this reason, distribution lines would also seem appealing for UAV localization tasks.

3.2 Conductor Configuration

Today, most of the world uses three-phase power systems. These polyphase systems require three conductors to carry alternating currents of the same frequency but offset by 120 degrees in phase. The benefit of three phase systems can be found in their ability to deliver nearly constant power to a load, as well as being able to create a rotating magnetic field which is convenient in electric motor design. Thus, it is important to realize that this three phase system is reflected in most power line conductor configurations [3].

Figure 3.3: Service Line Running from Distribution Lines to House

Different voltage level transmission lines tend to possess slightly different conductor configurations.

In high voltage transmission lines, three main conductors are used. These main conductors are used to actually transmit the three phase alternating currents, while other conductors are sometimes strung between the transmission towers above the main lines to serve as lightning attractors.

In the case of the main distribution lines, the wire configuration is similar even though power line voltage levels are lower. The main difference between high voltage transmission lines and lower voltage distribution lines is that distribution lines typically lack static wires while possessing a fourth wire which is connected to neutral [2]. Usually, if the three phases are balanced, no current should be flowing in this fourth, neutral wire. This assumption typically holds for transmission lines, but does not hold for distribution wires, whose phases are often not balanced, causing some current to flow in the neutral wire.[3].

In addition to these primary distribution lines, there are also secondary distribution lines which carry only one or two of the three phases carried by the primary distribution lines. This is achieved by the use of three-phase to two-phase taps or two-phase to one-phase taps. In the single phase case, a single-phase wire and neutral wire will be strung between telephone poles.

The final conductor configuration to be examined is that of the service line, which runs directly to the consumer. These lines break off from the single-phase distribution lines into two 120 volt conductors whose current is 180 degrees out of phase [2].

At first glance, it seemed as though an experimental set-up using a single conductor carrying a current of a single phase would be the best choice. Not only would such a

Figure 3.4: Three-Phase Powerline Configuration

configuration reflect some of the existing distribution lines already in use, but it would also allow for the simplest magnetic field model to be developed. However, this set-up poses some difficulty, for it would require the shielding of the return path.

3.2.1 Shielding Electromagnetic Fields

The subject of shielding electromagnetic fields can be an area of study all on its own, and depends heavily on a knowledge of electromagnetism. Therefore, a brief review of electromagnetism and electromagnetic shielding was deemed necessary for this thesis.

3.2.2 Electromagnetic Radiation

Electromagnetic radiation is common phenomenon in many electrical engineering applications. The relationship between electric and magnetic fields is well defined by Maxwell's Equations. These equations are made up of four physical laws: Gauss's law, Gauss's law of magnetism, Faraday's Law, and Ampere's Law with Maxwell's correction [47]. The differential form of the equations are:

$$\boldsymbol{\nabla} \cdot \mathbf{E} = \frac{\rho_v}{\epsilon_0} \tag{3.1}$$

$$\boldsymbol{\nabla} \cdot \mathbf{B} = 0 \tag{3.2}$$

$$\boldsymbol{\nabla} \times \mathbf{E} = -\frac{\partial \mathbf{B}}{\partial t} \tag{3.3}$$

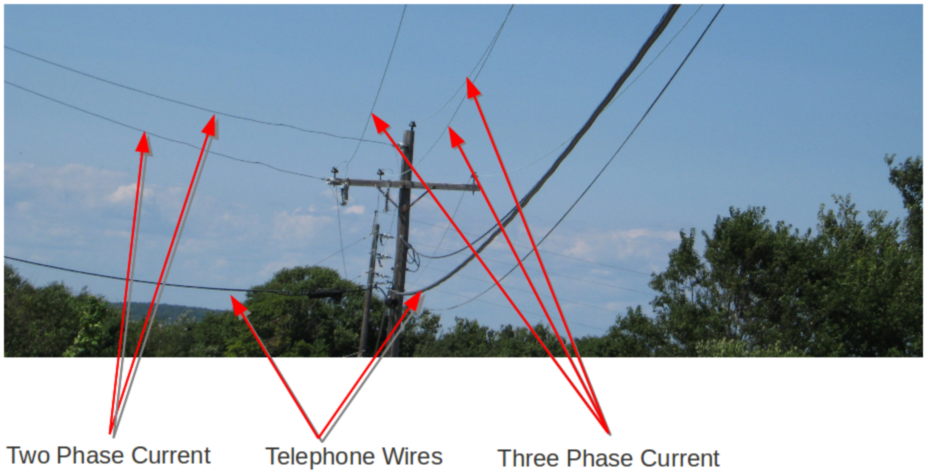

Figure 3.5: Three-Phase to Two-Phase Powerline Configuration

$$\boldsymbol{\nabla} \times \mathbf{H} = \mu_0 \mathbf{J} + \mu_0 \epsilon_0 \frac{\partial \mathbf{E}}{\partial t} \tag{3.4}$$

Integrating the equations yields

$$\oint \mathbf{E} \cdot d\mathbf{S} = \frac{Q}{\epsilon_0} \tag{3.5}$$

$$\oint \mathbf{B} \cdot d\mathbf{S} = 0 \tag{3.6}$$

$$\oint \mathbf{E} \cdot d\mathbf{l} = -\frac{\partial \mathbf{\Phi}}{\partial t} \tag{3.7}$$

$$\oint \mathbf{B} \cdot d\mathbf{l} = \mu_0 I + \mu_0 \epsilon_0 \frac{\partial \mathbf{\Phi}}{\partial t} \tag{3.8}$$

From Ampere's law one can deduce that a time-varying electric field will create a magnetic field and from from Faraday's law one can deduce that a time-varying magnetic field will create an electric field. In the case of a powerline, one has an alternating current flowing through a conductor. If this current was constant, a constant magnetic field would arise. However because the current is changing with time, this creates a changing magnetic field, which, in turn, also creates an time varying electric field. In many ways, this makes the powerline very similar to a closed loop antenna.

Oftentimes, when dealing with electromagnetics, electrical engineers refer to the electromagnetic field surrounding the antenna as having both inductive and radiative components. The inductive field refers to the region where the field is dominated by inductive characteristics, that is, all power is reactive and is returned to the source. In contrast, the far-field region is where radiation dominates, and in this case, the power is actually being dissipated by the source, as in a resistor. It is important to note that in the inductive, or near-field, region, the current and voltage are typically 90 degrees out of phase, where as in the far-field region, the electric and magnetic fields are in phase with one another. It is this far-field region of an antenna where the field begins to exhibit the true characteristics of an electromagnetic wave.

In most cases, radiative characteristics begin to dominate at a wavelength from the source. For a system operating near 60 Hz, this would be equivalent to 3100 miles. Therefore, it is adequate to assume that an extremely low frequency field is quasistatic, and therefore, can be treated purely as inductive in nature. Furthermore, this indicates that in the regions of operation for the UAV, the electric and magnetic fields are effectively decoupled [1].

3.2.3 Shielding Low Frequency Electric Fields

In many engineering applications, Electric Fields can be easily shielded, especially if they are low frequency. For instance, to shield the electric field generated by single wire carrying a low frequency current, one would merely have to enclose the wire in a grounded conductor. Because electric fields begin at positive charges and terminate on negative charges, the electric fields would be contained by the conductor [32].

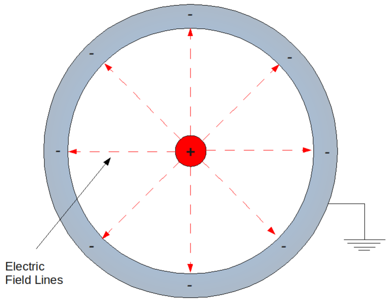

Figure 3.6: Shielding Electric Fields

3.2.4 Shielding Low Frequency Magnetic Fields

The method of shielding magnetic fields is often dependent of the frequency of the field. For instance, many times a conductor is sufficient to shield high frequency magnetic fields, since the skin effect is able to very effectively produce opposing eddy currents capable of canceling out the applied field [5]. However, most engineering literature holds that the inherent resistances in typical conductive metals such as aluminum prevents the generation of substantial eddy currents in frequencies below a few kHz [33]. For static magnetic field shielding, typically high permeability metals must be used to redirect the field lines away from a magnetically sensitive area as shown in Figure 3.7. This method also works well for low frequency magnetic fields. However, if one attempted to surround a single conductor with a ferromagnetic tube, no shielding would occur at all. Such a shield is ineffective because the magnetic field generated by the wire is tangential and continuous at the shield's surface [48], and these boundary conditions do not result in an altered magnetic field. It is possible to redirect the magnetic field somewhat using a partial ferromagnetic shield, however, this will still not attenuate the magnetic field entirely.

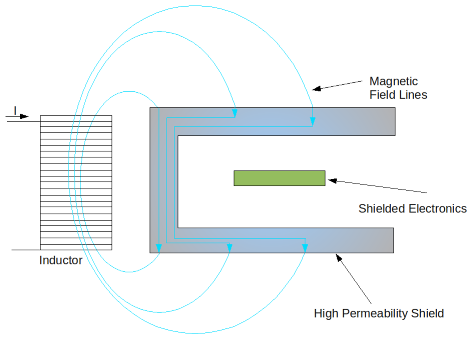

Figure 3.7: Shielding Low Frequency Magnetic Fields

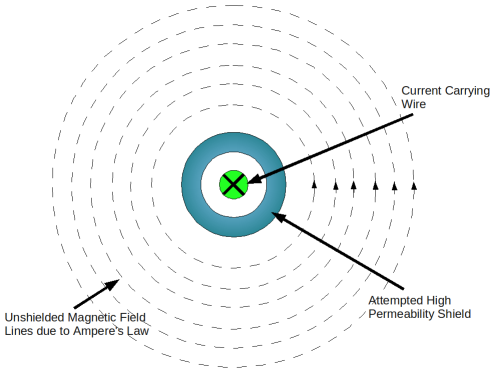

Figure 3.8: Shielding Low Frequency Magnetic Fields Produced by Single Conductor

3.3 Rectangular Current Loop

Because low frequency magnetic fields of single conductors can not be easily shielded, the best configuration for an experimental powerline set-up was deemed to be that a rectangular current loop, initially to be approximated as two parallel wires carrying currents 180 degrees out of phase. In addition, this configuration, because of its dipole characteristics, more accurately represents the magnetic field geometry of the three phase configuration typically observed in the majority of distribution lines. If around 100 Amps of current can be passed through the conductors, the indoor power-line set up would provide a reasonable means of assessing signal pick-up at 4 meters from the source.

Chapter 4

Experimental Set-Up

By converging on the rectangular current loop configuration, the first step was made toward meeting the sensing range requirement. The next step was to actually construct the indoor powerline set-up, to select the necessary sensing hardware, and to demonstrate signal measurement. From a rough, preliminary magnetic field analysis it was determined that a current of 40 amps would be enough get the range required. It was also reasoned, that because of the surrounding 60 Hz noise often found in indoor environments, it would be beneficial to be able to vary the frequency of the wire's current to avoid interference.

4.1 Experimental Powerline Set-Up

To implement the rectangular current loop, 4 gage high current welding wire was selected. To achieve the variable frequency functionality, a PWM current controller DC Motor amplifier from Advanced Motion Devices capable of carrying out sinusoidal commutation and generating currents around 50 Amps peak-to-peak was connected in series with a twelve foot loop of the 4 gage wire and a 1 mH inductive load. The motor amplifier was then fed by a 600 watt DC power supply and driven by a conventional signal generator capable of adjusting the frequency, amplitude, and offset of the current. To create the dipole configuration, a wooden stand was built to support a rectangular loop of wire 2.4 meters long by 0.3 meters wide. Furthermore, the wire leads bringing current to and from the power electronics were arranged in a twisted pair configuration so as to ensure that the only magnetic field being generated by the wire would be due to the loop. Figure 4.1 shows the rectangular current loop powerline stand and Figure 4.2 shows a block diagram of the power electronics used to generate the 80 Hz alternating current.

4.2 Preliminary Sensing Hardware

After the powerline set-up was constructed, preliminary sensing hardware was developed for the purpose of beginning the experimental process. It was deemed that if the field of a

Figure 4.1: Rectangular Current Loop Powerline Experimental Set-Up

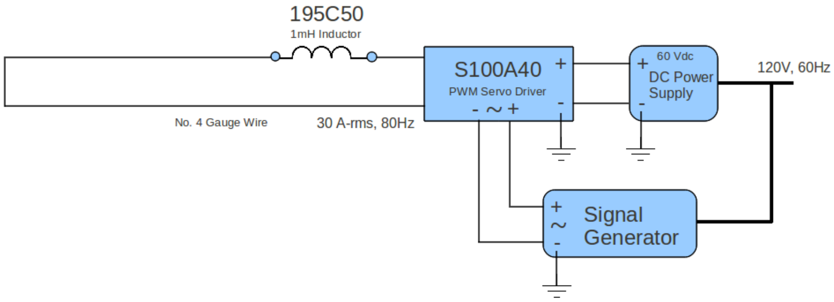

Figure 4.2: Power Electronics Used to Generate Alternating Current

power line carrying 40 Amps of current could be adequately measured from a distance of 4 meters from the wire, this would be the first step in assessing the feasibility of perching on a powerline using only magnetic field measurements.

4.2.1 Magnetometer Selection

The magnetometer used in this project was the HMC2003 from Honeywell [18], which was suggested by the project's sponsor. This magnetometer unit provides three axes of measurement, each of which has the capability of measuring +/- 2G down to 40 uG. Furthermore, the relationship between the sensor's voltage output and magnetic field measurement is stated to be linear. The HMC2003 is actually composed of two magnetorestive sensors, one of which has the ability to measure a magnetic field in two dimensions, while the other only allows for single axis measurements. Magnetoresistive sensors were chosen over fluxgate magnetometers because these sensors are characterized by very high sensitivity in direction of the external magnetic field and perform well under a wide range of environmental conditions [17]. Furthermore, they are far less fragile than fluxgate magnetometers. Very frequently, they are used to measure the earth's magnetic field in magnetic compass systems for various navigation tasks.

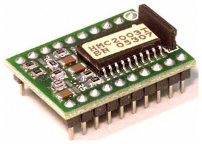

Figure 4.3: HMC2003 Magnetometer

4.2.2 Analog to Digital Converter

Because the 60 Hz alternating magnetic field has a frequency far below the sample rates available among current analog to digital converters, it was decided that processing the magnetic field signals digitally would be the best choice. Today, digital signal processing is greatly preferred over its analog counterparts in most engineering applications. Not only do DSP methods offer greater robustness, they permit fewer components, and are more easily updated and/or modified.

However, although the bandwidth of our system is well within the specifications of most analog to digital converters, the dynamic range of the system is not. Over the span of 4 meters, magnetic field signals will range from a few hundred microGauss to several Gauss in magnitiude due to the magnetic field $\frac{1}{r^2}$ decay rate. For this reason, it was determined that an extremely high resolution analog to digital converter with close to 20 bits of resolution would be required to capture both range and precision. To meet the required specifications, the ADS1256 TI Delta-Sigma 24-bit analog to digital converter was selected. This device has a maximum sampling rate of 30,000 samples per second, a built in multiplexer for switching seven channels, and has the capability of measuring down to about 0.1 uV. Furthermore, the ADS1256 has a topology which is designed specifically for low-noise applications. The device provides the aircraft with the ability to measure the magnetic field values ranging from 100 uV to 2.5V with incredible accuracy and prevents the need of a logarithmic amplifier which would require additional circuitry to account for bi-polar measurements. The ADS1256 also has the ability to communicate with any microcontroller via a SPI protocol.

4.2.3 Microcontroller

To communicate with the analog to digital converter and to manage the low level signal processing tasks, the ATMEGA128 AVR microcontroller was selected. This microcontroller is extremely common, well documented, and a reasonable choice for embedded applications where computation is limited.

4.2.4 Preliminary Sensing Platform

For the initial investigation, a sensing test platform which could be easily moved around in the magnetic field by hand was developed. Using evaluation boards, the sensing test platform allowed the analog to digital converter, the microcontroller, and the magnetometer to be assembled together. A photo of the preliminary sensing hardware can be found in Figure 4.4

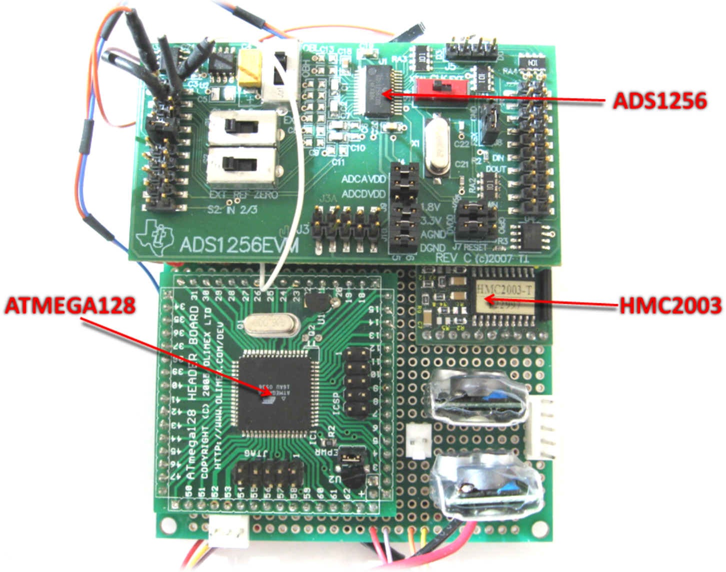

Figure 4.4: Original Magnetic Field Sensing Device

Once the sensor platform was developed, several preliminary sensing trials were conducted in the presence of a magnetic field oscillating at 10Hz by moving the sensor platform through a range of x and z positions and then processing the data off line. This preliminary test yielded promising results, and the raw data can be found in Figure 4.5. Already, it seemed as though the range requirements of the first question would be met.

4.2.5 60 Hz Noise

In addition to the position sweep, an effort was made to examine the noise present in the indoor magnetic field measurements. At about 4 meters from the powerline set-up a Fourier transform was taken of the raw magnetometer data. The Fourier transform revealed that the main frequency components present in the magnetometer data were the 60 Hz line noise, its odd harmonics, and the 80 Hz powerline signal. This can be observed in figure 4.6.

4.2.6 System Calibration

During the course of the design phase, several system tests were developed. One test developed sought to verify the linear nature of the magnetometer measurements. By placing

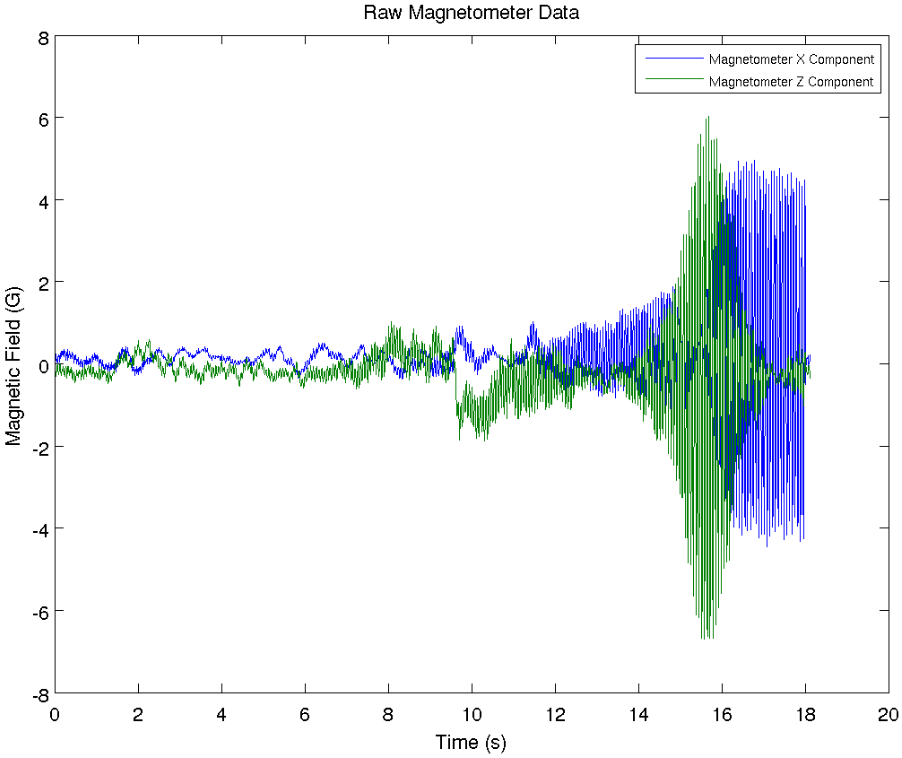

Figure 4.5: Raw Magnetometer Data

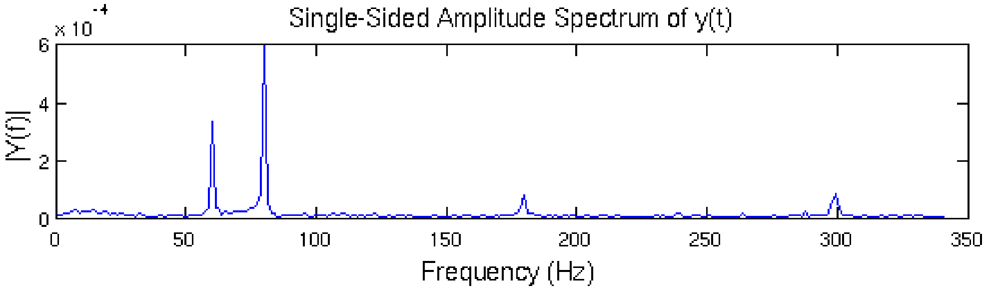

Figure 4.6: Fourier Transform of Magnetometer Signal

the magnetometer at a stationary position in the magnetic field, the current in the wire was varied. If the magnetometer was indeed linear in its response, based upon the magnetic field equations derived, one should see a linear relationship between current and measured magnetic field. The magnetometer response is indeed linear, even down to very small voltage levels, as can be seen in Figure 4.7

A second test devised used a signal generator to test the linearity of the analog to digital converter. A variety of 80 Hz signal amplitudes from 0-2.5 volts were applied, and the analog to digital converter demonstrated a non-linear response. In figure 4.8, one can see a clear change in slope when the applied voltage is 1V peak. The system shows that a gain of 1.48

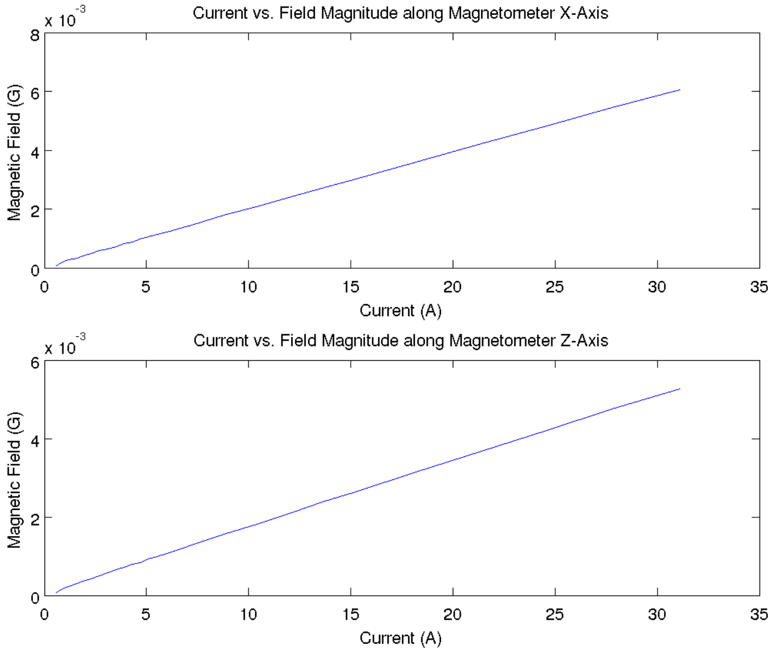

Figure 4.7: Current vs. Magnetometer Voltage at Stationary Field Position

exists for voltages from 0-1v, and this was the gain on the signal used in verifying the state estimation, since most often the magnetic field does not exceed 1G, except very very close to the wire.

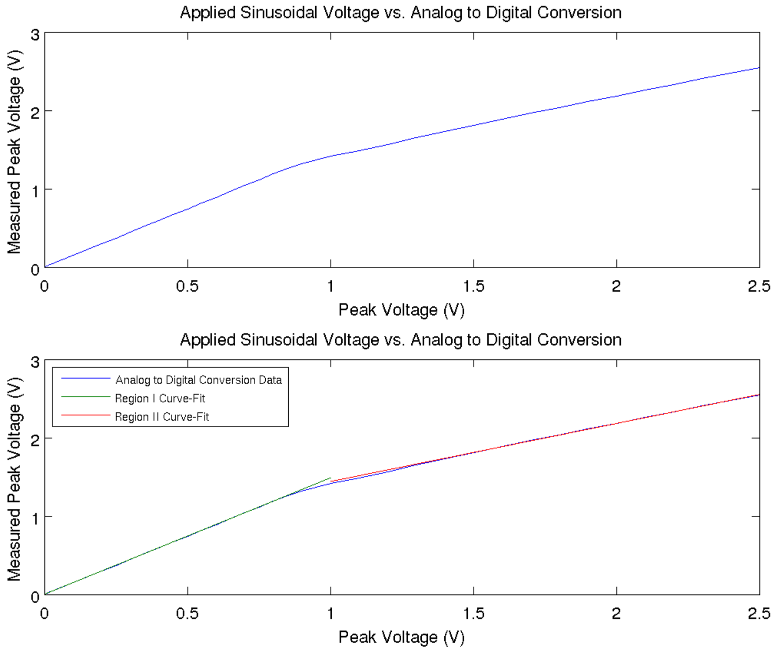

Figure 4.8: Nonlinearity of Analog to Digital Conversion

4.3 Summary of Initial Experimental Results

In this Chapter, we demonstrated that it is in fact possible to sense the magnetic field at 4 meters from a current carrying wire. Since our experimental set-up is similar in current level and geometry to what is found in reality, we have made significant process in addressing the first research question. Nevertheless, we do not consider the question "Can the magnetic field be detected along the length of the perching trajectory?" answered, since we have not demonstrated the ability to separate the magnetic field amplitude from its oscillating component. Since our aircraft dynamics are below 10 Hz, it is not desirable to include the 60 Hz carrier frequency into the magnetic field model. For this reason, we assert that successful magnetic field detection is characterized by the isolation of the amplitude of the magnetic field signals 4 meters from the wire, not merely the measurement of the alternating magnetic field signal.

Chapter 5

Digital Signal Processing

The final step in answering the question “Can the magnetic field be detected along the length of the perching trajectory?” requires the separation of the magnetic field amplitude from its oscillating carrier signal. By avoiding the temptation to incorporate the alternating nature of the magnetic field into our magnetic field model, we are able to reduce the update rate required by our state estimator to track the magnetic field signals.

Consider a 60 Hz signal being tracked by a state estimator. To prevent aliasing, the state estimator would be required to have an update rate of at least 120 Hz, which would most likely exhibit poor noise rejection. As sample rate increases, noise rejection will improve. However, at some point, as the update rate increases, computational efficiency will become an issue for the state estimator. By employing a demodulation algorithm to measure the magnetic field’s amplitude, we are able to significantly reduce the update rate required by the state estimator and thus alleviate much of the computational burden placed on the system.

5.1 Envelope Detection

There are two main amplitude demodulation methods commonly used in for signal processing tasks. The first method is known as envelope detection, or asynchronous detection [31]. By far the simpler method, envelope detection obtains the values of the peaks of a modulating signal, bandpassed at the desired frequency. In analog circuitry, this method requires an incoming signal to be rectified via a diode and lowpass filtered so as to obtain the envelope of the signal. The same can also be done in software by creating a moving window which takes the maximum value of the incoming peaks. There are, however, several disadvantages to using this method. Envelope detectors often exhibit distortion, especially when the carrier frequency is not strong enough, and they also perform poorly with respect to noise when the signal values are low. Furthermore, envelope detection provides only amplitude information, and thus completely neglects the phase of the signal, which is necessary to have a complete field measurement [31].

A graphical representation of envelope dectection can be seen in Figure 5.1.

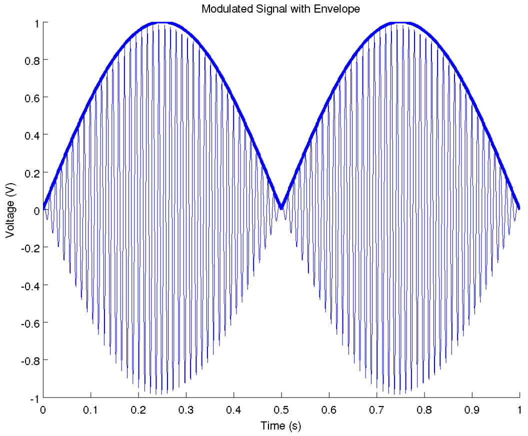

Figure 5.1: An Example of Envelope Detection

5.2 Synchronous Demodulation

The second method of amplitude demodulation is synchronous demodulation [31]. In this method, after the signal is bandpass filtered at the frequency of choice, it is multiplied by a local oscillator having the same frequency and phase as the incoming signal. This forces the band-limited signal to be centered around the origin instead of being centered around the original frequency of modulation. The resulting signal can then be low passed filtered to remove the higher frequency noise injected into the signal during the demodulation process [31].

The derivation below corresponds to the frequency domain representation of synchronous demodulation as represented in figures 5.2 and 5.3.

The carrier frequency is given by $c(t)$ which, in our case, is 80 Hz.

$$c(t) = e^{j\omega_c t} \tag{5.1}$$

$v(t)$ represents the signal after it is modulated with the carrier. A sinusoidal function with the envelope of the message signal has been created.

$$v(t) = m(t)e^{j\omega_c t} \tag{5.2}$$

Now use the Fourier Transform to transform $v(t)$ into the frequency domain.

$$V(j\omega) = \frac{1}{2\pi} M(j\omega) * \pi(\delta(\omega - \omega_c) + \delta(\omega - \omega_c)) \tag{5.3}$$

Because the signal $M(j(\omega - \omega_c))$ is being convolved with a delta function at a frequency of 80 Hz, the message signal is shifted by 80 Hz in each direction, and now becomes centered around +/- 80 Hz.

$$V(j\omega) = \frac{1}{2}M(j(\omega - \omega_c)) + \frac{1}{2}M(j(\omega + \omega_c)) \tag{5.4}$$

Next the signal is multiplied by $v(t)$ in the time domain by a sinusoid at the frequency of the carrier. This becomes convolution in the time domain

$$W(j\omega) = \frac{1}{2}(M(j(\omega - \omega_c)) + M(j(\omega + \omega_c))) * \pi(\delta(\omega - \omega_c) + \delta(\omega - \omega_c)) \tag{5.5}$$

Again, the delta function causes the signal to shift by ω_c. A low pass filter can now be used to remove the high frequency components, thus recovering the message signal.

$$W(j\omega) = \frac{1}{2}M(j\omega) + \frac{1}{4}M(j(\omega + 2\omega_c)) + \frac{1}{4}M(j(\omega - 2\omega_c)) \tag{5.6}$$

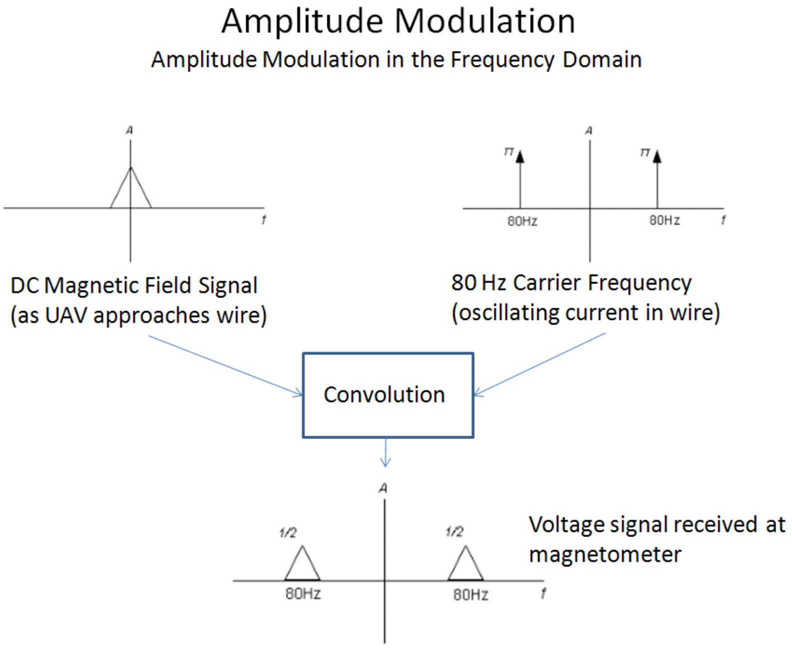

Figure 5.2: Modulation of Magnetic Field Signal

Unlike asynchronous demodulation, pure synchronous demodulation does not merely yield the true signal's amplitude, but actually reconstructs the true signal. However, it can only do so if it has exact knowledge of the modulating signal's amplitude and phase. Thus, the major disadvantage of the synchronous detection method is that it is very difficult to obtain an exact representation of the modulating sinusoid (phase and amplitude) at the receiver [31]. In many cases, especially in analog circuit design, a phase-lock loop is used to obtain the local oscillator with the correct magnitude and phase. These phase locked loops are essentially feedback loops which drive the phase of the local oscillator to match

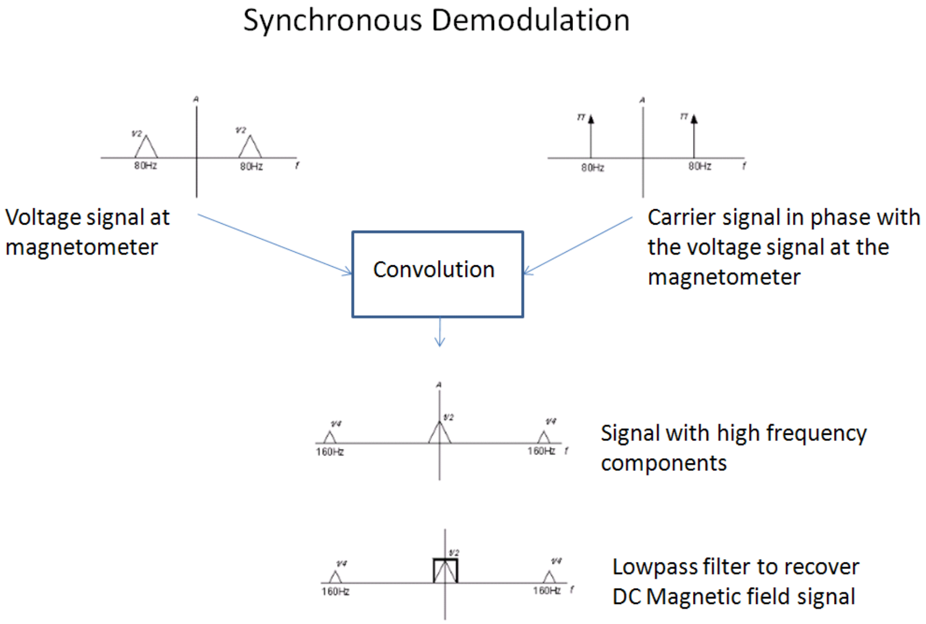

Figure 5.3: Demodulation of Magnetic Field Signal

that of the incoming waveform. In some cases these methods are effective, but sometimes, the methods of phase reconstruction can lead to waveform distortion or instability.

There is, however, an alternate method of obtaining an exact representation of the message signal which does not necessarily require a phase locked loop. This method is know as Complex Synchronous Detection, or Quadrature Demodulation, and is particularly well suited to embedded implementation.

It is well known that any sinusoidal signal with a given phase can be decomposed into both a cosine component and sine component. Therefore, if instead the incoming magnetic field signal is multiplied by both a cosine wave and a sine wave at the same frequency, and the independent, resulting signals are low pass filtered, these two filtered signals one can have access to both the real (cosine) and imaginary (sine) components of the original signal [31]. Instead of carrying out the mathematics using the Fourier Transform, knowledge of Euler's identity will be used instead.

From Euler's identity, we know that the modulated message signal is equivalent to:

$$m(t)cos(\omega_c t + \phi) = m(t)\frac{e^{j(\omega_c t+\phi)} + e^{-j(\omega_c t+\phi)}}{2} \tag{5.7}$$

We also know that:

$$cos(\omega_c t) = \frac{e^{j(\omega_c t)} + e^{-j(\omega_c t)}}{2} \tag{5.8}$$

$$sin(\omega_c t) = \frac{e^{j(\omega_c t)} + e^{-j(\omega_c t)}}{2j} \tag{5.9}$$

Multiplying the message signal by a cosine and sine signal at the same frequency yields:

$$m(t)cos(\omega_c t + \phi)cos(\omega_c t) = \frac{e^{j(2\omega_c t+\phi)} + e^{-j(2\omega_c t+\phi)} + e^{j\phi} + e^{-j\phi}}{4} \tag{5.10}$$

$$m(t)cos(\omega_c t + \phi)sin(\omega_c t) = \frac{e^{j(2\omega_c t+\phi)} - e^{-j(2\omega_c t+\phi)} + e^{j\phi} - e^{-j\phi}}{4j} \tag{5.11}$$

These exponential equations can then be transformed back into their sinusoidal counterparts as follows:

$$\frac{e^{j(2\omega_c t+\phi)} + e^{-j(2\omega_c t+\phi)} + e^{j\phi} + e^{-j\phi}}{4} = m(t)\frac{cos(2\omega_c t + \phi) + cos(\phi)}{2} \tag{5.12}$$

$$\frac{e^{j(2\omega_c t+\phi)} - e^{-j(2\omega_c t+\phi)} + e^{j\phi} - e^{-j\phi}}{4j} = m(t)\frac{sin(2\omega_c t + \phi) + sin(\phi)}{2} \tag{5.13}$$

After these signals are low-pass filtered, the results are

$$y_c(t) = m(t)\frac{cos(\phi)}{2} \tag{5.14}$$

$$y_s(t) = m(t)\frac{sin(\phi)}{2} \tag{5.15}$$

Notice that these two signals which are 90 degrees out of phase with one another and together they represent the real and complex components of the message signal. For instance, by taking the magnitude of these component signals, the magnitude of the true message signal is recovered. A simulation of this process can be observed in Figure 5.4.

Fortunately, the complex synchronous demodulation method alleviates many of the disadvantages of envelope detection. It does not have the same level of distortion and it is also more robust to signal noise. More importantly, it provides some of the phase information which envelope detection discards. There is, however, still one significant disadvantage with even this demodulation method, and that is the notion of phase-amplitude ambiguity, which will be discussed later in the report.

Using the data collected in the previous section, this complex synchronous demodulation algorithm was carried out off-line, and the results can be seen in Figure 5.5. It is evident that we have indeed shown successful detection of the magnetic field signal at 4 meters from the wire.

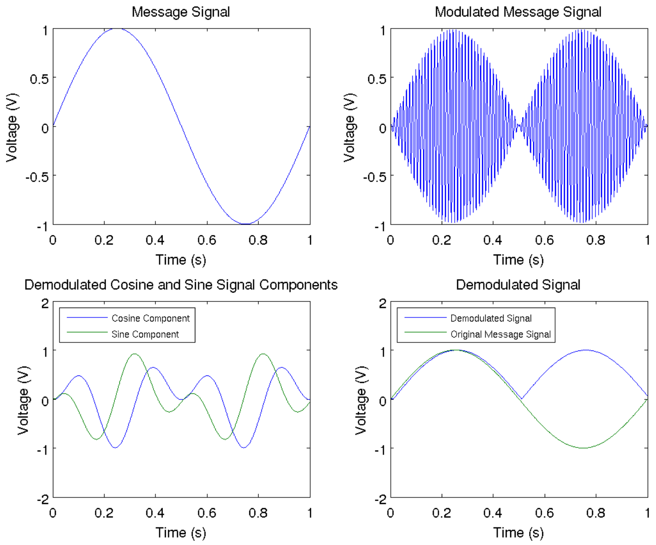

Figure 5.4: Simulation of Synchronous Demodulation

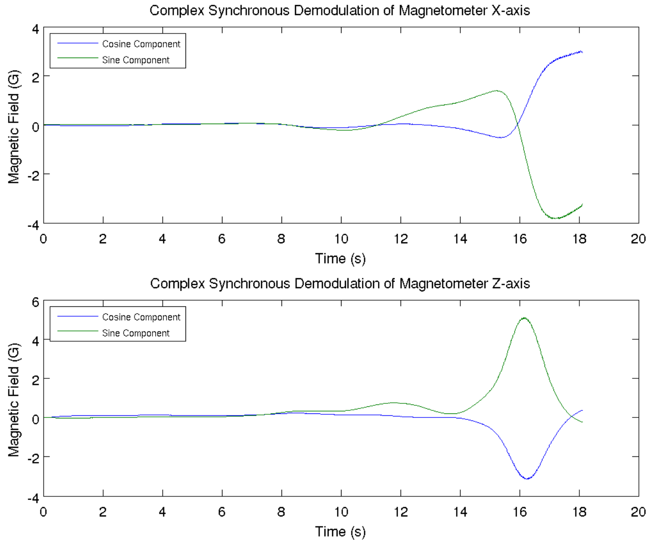

Figure 5.5: Complex Synchronous Demodulation of Raw Magnetometer Data

Chapter 6

Magnetic Field Modeling

Having answered the first research question, we proceed to the second, which is, "Can the powerline's magnetic field model be used to obtain position measurements?". In the previous chapter, we transformed the alternating magnetic field to its constant current counterpart through complex synchronous demodulation. In this chapter we begin to address the second question by considering the DC magnetic field generated by the rectangular current loop.

6.1 Infinite Parallel Wire Model

Initially, to simplify the magnetic field analysis, the rectangular current loop model was treated as two parallel conductors carrying opposing currents. This approximation ignores the small end wires and considers the longer wires to be infinite in length, yielding a version of a magnetic dipole which is somewhat mathematically simpler than the complete loop.

There are several benefits to using a dipole magnetic field model. First of all, it is a well-studied structure in electromagnetic theory. Both its far-field and near field characteristics are well known and documented. As stated in the previous section, however, because of the extremely low frequency of operation, the far-field radiative effects can be completely ignored.

The vector and magnitude plots of the Infinite Parallel Wires model can be viewed in Figures 6.1 and 6.2.

6.1.1 Magnetic Field Model Derivation

When considering this dipole magnetic field, it is useful to consider the magnetic field around a single conducting wire of infinite length. The diagram for this is shown in Figure 6.3. Using ampere's law, the field around a single straight wire can be derived as follows:

The integral form of Ampere's law, now simplified for a quasi-static case is:

$$\oint \mathbf{B} \cdot d\mathbf{l} = \mu_0 I \tag{6.1}$$

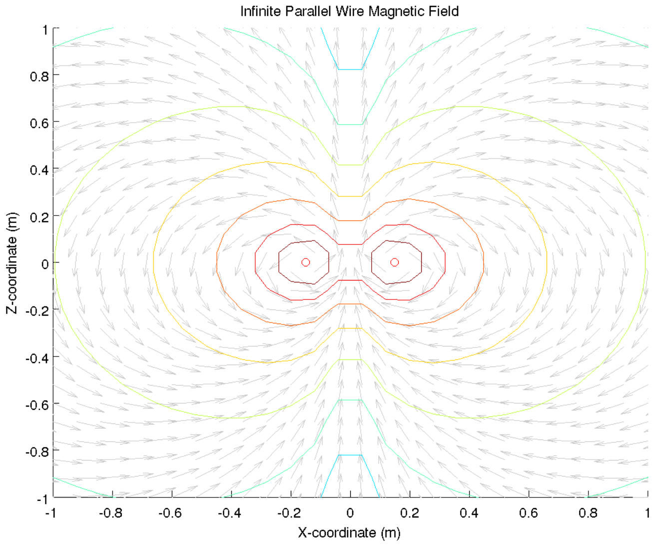

Figure 6.1: Parallel Wire Magnetic Field Vector Plot

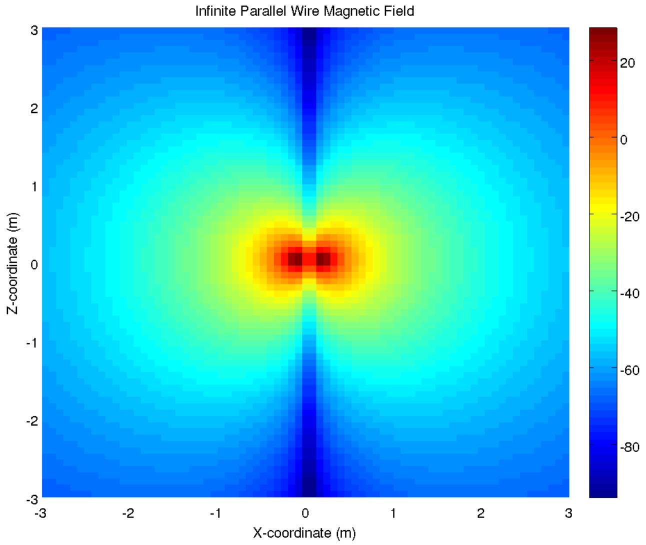

Figure 6.2: Parallel Wire Magnetic Field Magnitude Plot

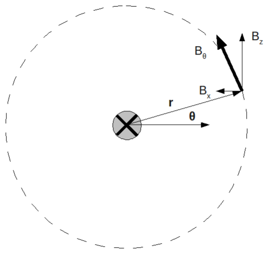

Figure 6.3: Diagram of Ampere's Law Derivation

Using polar coordinates, where the variables are r and θ:

$$d\mathbf{l} = r d\theta \tag{6.2}$$

If $\mathbf{B}$ is parallel with $d\mathbf{l}$, then

$$\oint \mathbf{B} \cdot d\mathbf{l} = B dl \tag{6.3}$$

where the Bdl is in the direction of d$\mathbf{l}$.
Then,

$$\int B r d\theta = \mu_0 I \tag{6.4}$$

$$\int_0^{2\pi} B r d\theta = \mu_0 I \tag{6.5}$$

$$B = \frac{\mu_0 I}{2\pi r} \tag{6.6}$$

$$\mathbf{B} = \frac{\mu_0 I}{2\pi r} \hat{\boldsymbol{\theta}} \tag{6.7}$$

We also know that this vector can be transformed from polar to rectangular coordinates as follows,

$$\hat{\boldsymbol{\theta}} = -\frac{x}{\sqrt{x^2 + z^2}} \hat{\mathbf{i}} + \frac{z}{\sqrt{x^2 + z^2}} \hat{\mathbf{k}} \tag{6.8}$$

$$r = \sqrt{x^2 + z^2} \tag{6.9}$$

$$\mathbf{B} = B_x \hat{\mathbf{i}} + B_z \hat{\mathbf{k}} \tag{6.10}$$

$$B_x = -\frac{\mu_0 I_c z}{2\pi(x^2 + z^2)} \tag{6.11}$$

$$B_z = \frac{\mu_0 I_c x}{2\pi(x^2 + z^2)} \tag{6.12}$$

Using this single wire field equation, the dipole equation can be derived through superposition.

$$B_z = -\frac{\mu_0 I (x - d)}{2\pi((x - d)^2 + z^2)} + \frac{\mu_0 I (x + d)}{2\pi((x + d)^2 + z^2)} \tag{6.13}$$

$$B_x = \frac{\mu_0 I z}{2\pi((x-d)^2+z^2)} - \frac{\mu_0 I z}{2\pi((x+d)^2+z^2)} \tag{6.14}$$

where d represents the distance between the wires carrying opposite currents $I+$ and $I-$.

If one solves for the positions x and z in terms of the field components B_x and B_z, one will find multiple analytical solutions. In fact, for a single pair of field components, if only the magnitudes of the magnetic field signals are known, eight possible solutions will exist.

6.2 Field Ambiguity

As stated in the previous section, one of the major challenges associated with magnetic field-based localization is that a single instantaneous magnetic field measurement can map to multiple different position values. Depending on the amount of information known about the signal measured at the magnetometer, the number of ambiguous cases range from two to eight. In this section, we hope to describe more thoroughly the origins of these ambiguous cases.

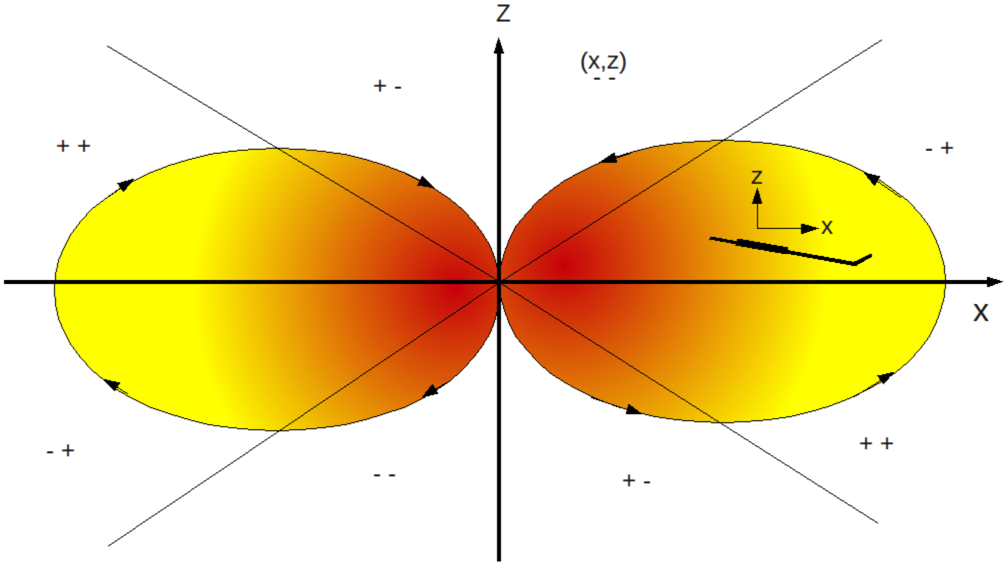

Figure 6.4: Phase Ambiguity Diagram

6.3 Model Symmetry

The first source of ambiguity can be attributed to the symmetry inherent in the magnetic field model. Consider figure 6.4, a two-dimensional diagram of the dipole magnetic field separated into octants based on the signs of the magnetic field vectors. Each of these octants contain pairs of field vectors with the same magnitudes but with a different sign combination. One can observe that, due to the symmetry, equivalent field measurements can be found in octants I and V. This indicates that *with* complete information about the magnetic field signal observed at the magnetometer, two ambiguous cases already exist.

6.4 Phase-Amplitude Ambiguity

The next source of the ambiguity arises from the alternating nature of the magnetic field. Because the phase of the current in the wire is unknown, perfect synchronous signal demodulation is impossible. For this reason, one will never be able to determine if a particular magnetometer signal is negative in value or 180 degrees out of phase. Without any phase information, eight possible ambiguous cases arise, as shown by the eight sections in Figure 6.4 and the trajectories in Figure 6.5.

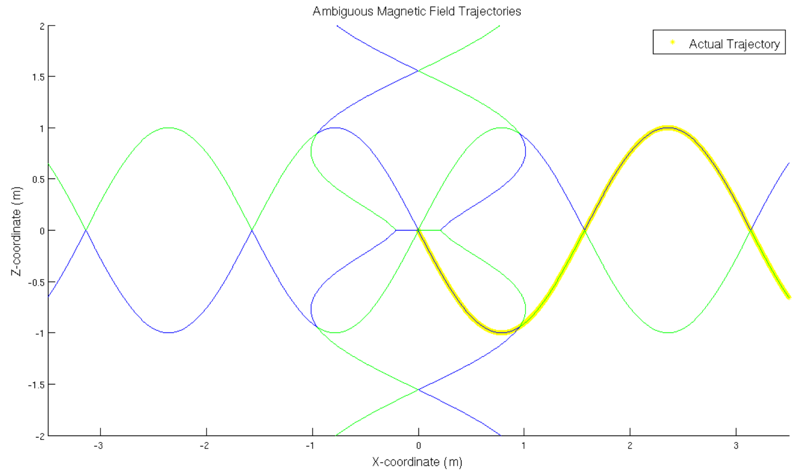

Figure 6.5: Ambiguous Trajectories Computed Using Inverse Field Equations

6.5 Reducing Ambiguity

There are several ways in which one could reduce the number of ambiguous cases. One method is to track the aircraft position using a state estimator. With knowledge of initial conditions as well as an aircraft model, some of the ambiguity, especially the ambiguity associated with model symmetry, should be able to be resolved. Another approach might involve making use of *relative phase*. By measuring the phase difference between the x and z components of the magnetic field, one could detect whether the magnetic field vectors have the same sign or opposite signs. This additional information reduces the number of ambiguous cases from eight to four- which is a significant advantage. For instance, instead of the ambiguous positions for a magnetic field value obtained in octant I spanning all octants, the ambiguous cases would only exist in octants III, V, and VII. Thus a state estimator, with initial conditions starting close to the x-axis on the far right in Figure 6.4, would be able to easily differentiate between octant I and octant VIII.

6.6 The Impact of Ambiguity on Position Estimation

In conclusion, due to the field ambiguities, it is not possible to obtain position measurements directly from the magnetic field model. Any pair of measured magnetic field components will map to at most eight and at least four (if relative phase is considered) ambiguous positions. However, there is a possibility that state estimation could overcome this obstacle. Therefore, in order to fully address the second research question, we must investigate state estimation methods.

Chapter 7

State Estimation

In order to address the question “Can we develop a model of the powerline’s magnetic field to obtain position measurements?”, state estimation must be investigated as a means to overcome some of the magnetic field model’s short comings. This chapter describes what is known as recursive Bayesian estimation as well as highlights the main recursive Bayesian filtering techniques used today. These techniques are then applied to the magnetic field-based localization problem, first in simulation, and then on actual data.

7.1 Recursive Bayesian Filtering

All of the state estimation techniques outlined in this paper are based on Recusive Bayesian Filtering. Bayes rule, which forms the foundation for this filtering technique is stated as follows:

$$p(x|y) = \frac{p(y|x)p(x)}{p(y)}. \tag{7.1}$$

Using this rule, we can write the probability distribution of the current state, x_t, in terms of the history of measurements $z_{1:t-1}$ and inputs $u_{1:t-1}$, where t represents time.

$$p(x_t|z_t, z_{1:t-1}, u_{1:t}) = \frac{p(z_t|x_t, z_{1:t-1}, u_{1:t})p(x_t|z_{1:t-1}, u_{1:t})}{p(z_t|z_{1:t-1}, u_{1:t})} \tag{7.2}$$

By taking into consideration conditional independence, this equation can be rewritten as,

$$p(x_t|z_t, z_{1:t-1}, u_{1:t}) = \eta p(z_t|x_t)p(x_t|z_{1:t-1}, u_{1:t}) \tag{7.3}$$

where η achieves normalization. We can then find $p(x_t|z_{1:t-1}, u_{1:t})$ by using the total probability theorem. The theorem of total probability is typically defined as

$$p(x) = \int p(x|y)p(y)dy \tag{7.4}$$

Substituting in appropriately we find,

$$p(x_t|z_{1:t-1}, u_{1:t}) = \int p(x_t|x_{t-1}, z_{1:t-1}, u_{1:t})p(x_{t-1}|z_{1:t-1}, u_{1:t-1})dx_{t-1} \tag{7.5}$$

which, in assuming conditional independence, can be rewritten as

$$p(x_t|z_{1:t-1}, u_{1:t}) = \int p(x_t|, x_{t-1}, u_t)p(x_{t-1}|z_{1:t-1}, u_{1:t-1})dx_{t-1} \tag{7.6}$$

Equations 7.3 and 7.6, when used together, are recursive in nature and constitute Bayes Filter Algorithm [45]. Typically, limitations are placed on recursive Bayesian estimation due to the difficultly in finding a solution for equation 7.6. Extended Kalman Filtering, Unscented Kalman Filtering and Particle Filtering are the three most common methods used to implement recursive Bayesian estimation. Each method has a different means for approximating equation 7.6, typically trading off computational efficiency with accuracy in representing the probability distributions.

7.1.1 Extended Kalman Filter

The Extended Kalman Filter is one form of recursive Bayesian estimation where the probability distributions are approximated as Gaussian distributions and the nonlinear system equations are linearized. For this situation, there is an analytical solution for the integral in the recursive Bayesian estimation equations, which will allow one to track the probability distribution of the system as it evolves over time. This analytical solution is contained in the Extended Kalman Filter algorithm, which has found widespread use in many estimation applications.

Extended Kalman Filter Algorithm

To implement the Extended Kalman Filter, compute the forward plant dynamics using the nonlinear model,

$$\hat{x}_{t|t-1} = f(\hat{x}_{t-1}, u_t) \tag{7.7}$$

where $\hat{x}$ is the system state, t is time, f represents a nonlinear function, and u_t is the system input. Then, determine the error covariance matrix as well as the Kalman gains in the following manner:

Compute the *a priori* error covariance matrix as,

$$P_{t|t-1} = F_t P_t F_t^T + Q_t \tag{7.8}$$

where Q_t is the process covariance matrix and F_t represents the process gradients. The observer gain matrix K_t can the be computed as,

$$K_t = P_{t|t-1} H_t^T [H_t P_{t|t-1} H_t^T + R_t]^{-1} \tag{7.9}$$

where, R_t is the measurement covariance and H_t represents the measurement gradients. Then compute the *a posteriori* error covariance matrix,

$$P_t = (I - K_t H_t) P_{t|t-1} \tag{7.10}$$

Finally, update the state estimate by multiplying Kalman gain matrix by the measurement error as shown,

$$\hat{x}_t = \hat{x}_{t|t-1} + K_t(y_t - y(\hat{x}_{t|t-1})) \tag{7.11}$$

where y is the output of the measurement model and y_t is the actual measurement at time t.

7.1.2 Unscented Kalman Filter

The Unscented Kalman Filter is a recursive Bayesian estimation technique which uses the unscented transform and a collection of sample points (also known as sigma points) to compute the covariances. By deterministically sampling a Gaussian distribution, one can pass these sigma points through the system dynamics and measurement equations and then use the resulting outputs to compute the system's mean and covariance [21]. Unlike the Extended Kalman Filter, one does not have to rely on a linearized system model. However, like the EKF, one is restricted to Gaussian distributions.

Unscented Kalman Filter Algorithm

The first step in carrying out the Unscented Kalman Filter is to define a series of constants for the *unscented transform*. Here, λ is defined by L, the size of the state, x, and the arbitrary constant α which determines the spread of the sigma points.

$$\lambda = L(\alpha^2 - 1) \tag{7.12}$$

$$\eta = \sqrt{L + \lambda} \tag{7.13}$$

The weights for the unscented transform are computed as follows, where $\beta = 2$ represents a Gaussian distribution.

$$W_0^s = \frac{\lambda}{L + \lambda} \tag{7.14}$$

$$W_0^c = \frac{\lambda}{L + \lambda} + (1 - \alpha^2 + \beta) \tag{7.15}$$

$$W_i^s = \frac{1}{2(L + \lambda)} \tag{7.16}$$

$$W_i^c = \frac{1}{2(L+\lambda)} \tag{7.17}$$

Here, the index i represents an individual sigma point, and when $i = 0$, the weight corresponds to the sigma point at the mean of the distribution. Once all the constants are defined for the transform, an augmented state vector is formed, where x is the process model state, w is the process noise, and v is the measurement noise.

$$x^a = [x^T w^T v^T] \tag{7.18}$$

An augmented covariance matrix,P^a, is also created by combining the covariance matrix ,P, with the measurement and process noise covariance matrices Q and R, as follows:

$$P^a = \begin{pmatrix} P & \mathbf{0} & \mathbf{0} \\ \mathbf{0} & Q & \mathbf{0} \\ \mathbf{0} & \mathbf{0} & R \end{pmatrix} \tag{7.19}$$

The filter begins by computing values for the sigma points, X_{t-1}^a, which are distributed about the mean.

$$X_{t-1}^a = \left[\begin{array}{cc} x_{t-1}^a & x_{t-1}^a \pm \sqrt{(\eta+\lambda)P_{t-1}^a} \end{array} \right] \tag{7.20}$$

The state and process noise sigma points X_{t-1}^x and X_{t-1}^v are then propagated through the nonlinear system dynamics, f:

$$X_{t|t-1}^a = f(X_{t-1}^x, X_{t-1}^v) \tag{7.21}$$

The average state estimation is weighted sum of the sigma points after they have been propagated through the system dynamics.

$$\bar{x}_{t|t-1} = \sum_{i=0}^{2L} W_i^s X_{t|t-1}^x \tag{7.22}$$

The prior probability distribution, $P_{t|t-1}$, can then be computed as follows:

$$P_{t|t-1} = \sum_{i=0}^{2L} [X_{i,t|t-1}^x - \bar{x}_{t|t-1}][X_{i,t|t-1}^x - \bar{x}_{t|t-1}]^T \tag{7.23}$$

Next, the predicted measurements, $Y_{t|t-1}$, are computed by propagating the sigma points through the nonlinear measurement equations, h.

$$Y_{t|t-1} = h(X_{t|t-1}^x, X_{t-1}^v) \tag{7.24}$$

The nominal measurements,$\bar{y}_{t|t-1}$, can be computed by taking an average of the measurement values relating to the sigma points.

$$\bar{y}_{t|t-1} = \sum_{i=0}^{2L} W_i^s Y_{i,t|t-1}^x \tag{7.25}$$

The predicted measurement covariance, P_{yy}, and the state-measurement cross covariance, P_{xy}, can be determined respectively as follows:

$$P_{yy} = \sum_{i=0}^{2L} W_i^c [Y_{i,t|t-1} - \bar{y}_{t|t-1}][Y_{i,t|t-1} - \bar{y}_{t|t-1}]^T \tag{7.26}$$

$$P_{xy} = \sum_{i=0}^{2L} W_i^c [X_{i,t|t-1} - \bar{x}_{t|t-1}][X_{i,t|t-1} - \bar{x}_{t|t-1}]^T \tag{7.27}$$

Finally, the Kalman gain,K_t, the updated state estimate, $\bar{x}_t$ and the updated covariance matrix, P_t, can be computed as

$$K_t = P_{xy} P_{yy}^{-1} \tag{7.28}$$

$$\bar{x}_t = \bar{x}_{t|t-1} + K_t(y_t - \bar{y}_{t|t-1}) \tag{7.29}$$

$$P_t = P_{t|t-1} - K_t P_{yy} K_t^T \tag{7.30}$$

7.1.3 Particle Filter

Particle filtering is a computationally intensive method of approximating the recursive Bayesian Filter. By representing the probability distribution of the system as a collection of particles, one can avoid solving the integral in the recursive Bayesian estimation equations analytically. For this reason, one is not required to make any assumptions about system dynamics or probability distributions [45]. Initially, the particle filter seemed particularly applicable to the magnetic field sensing application. As previously mentioned, the ambiguity between the phase and amplitude of a magnetometer reading allows for eight possible locations if a magnetic field measurement is propagated through equations relating the magnetic field vectors to the x and z coordinates. Because of its ability to manage multi-modal probability distributions, the particle filter is able to reason about these possible locations and determine the most probable estimation for the vehicle's center of mass given a knowledge of the system dynamics.

The particle filter algorithm is described as follows:

1: Sample x_t^i particles from the distribution $p(x_t|u_t, x_{t-1}^i)$

2: Weight particles based on assumed distribution of $p(z_t|x_t)$

3: Normalize the weights

4: Estimate the current state as the mean of the particles corresponding to that state

5: Resample to eliminate samples with low weights.

The re-sampling section of the algorithm merely draws, with replacement, particles from the current set of particles with a probability proportional to the weights of the particles. This newly drawn set of particles then replaces the current set of particles, thus causing the probability density to contract. The weights are then reset to $\frac{1}{N}$ [45]. A diagram of the particle filtering process can be seen in Figure 7.1.

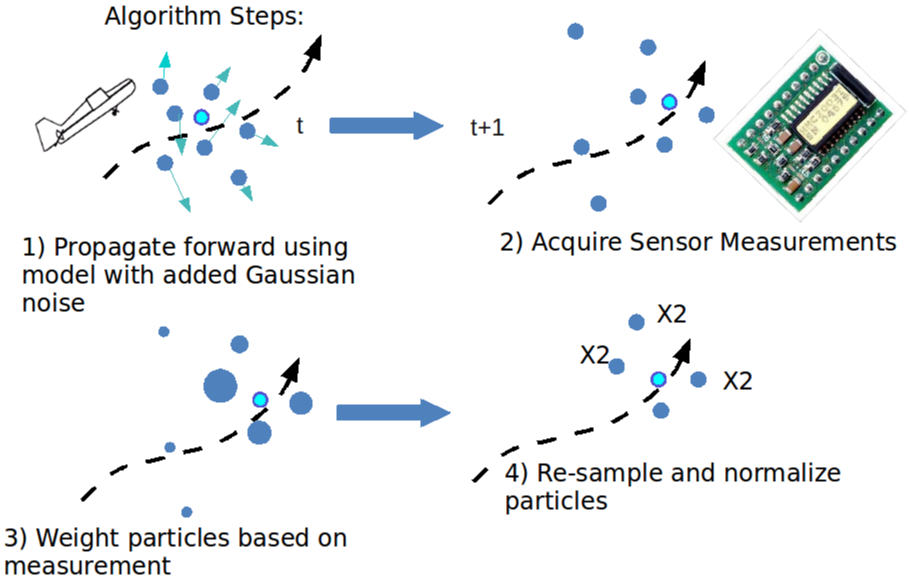

Figure 7.1: Particle Filter Algorithm

7.2 Simulation

To investigate our state estimation methods in simulation, we must first identify the process model and measurement model used. In all simulations, the infinite parallel wire model derived in the previous chapter is used as the measurement model along with a direct measurement of aircraft pitch, which is assumed to come from the inertial measurement unit. For the process model, a flat plate glider model is used.

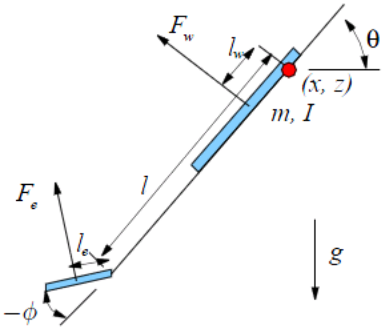

Figure 7.2: Flat Plate Glider Model

7.2.1 Flat Plate Glider Process Model

The flat plate glider model, which is shown in Figure 7.2, represents two dimensional aircraft dynamics with only an elevator for actuation. The aerodynamic forces are assumed to act perpendicular to both the surfaces of wing and the elevator. These forces have the form,

$$F_D = \frac{C_D \rho V^2 A}{2} \tag{7.31}$$

$$F_L = \frac{C_L \rho V^2 A}{2} \tag{7.32}$$

$$C_L = 2\sin\alpha\cos\alpha \tag{7.33}$$

$$C_D = 2\sin^2\alpha \tag{7.34}$$

where α is the angle of attack of the surface, V is velocity of the surface with respect to the air, ρ is the density of air, and A is the area of the surface. With these forces defined, the full system dynamics can be written as,

$$\dot{x}_w = \dot{x} - l_w\dot{\theta}sin(\theta) \tag{7.35}$$

$$\dot{z}_w = \dot{z} + l_w\dot{\theta}cos(\theta) \tag{7.36}$$

$$\alpha_w = \theta - \arctan\frac{\dot{z}_w}{\dot{x}_w} \tag{7.37}$$

$$F_w = \rho S_w sin(\alpha_w)(\dot{z}_w^2 + \dot{x}_w^2) \tag{7.38}$$

$$\dot{x}_e = \dot{x} + l\dot{\theta}\sin(\theta) + l_e(\dot{\theta} + \dot{\phi})\sin(\theta + \phi) \tag{7.39}$$

$$\dot{z}_e = \dot{z} - l\dot{\theta}\cos(\theta) - l_e(\dot{\theta} + \dot{\phi})\cos(\theta + \phi) \tag{7.40}$$

$$\alpha_e = \theta + \phi - \arctan\frac{\dot{z}_e}{\dot{x}_e} \tag{7.41}$$

$$F_e = \rho S_e \sin\alpha_e(\dot{z}_e^2 + \dot{x}_e^2) \tag{7.42}$$

$$\dot{\phi} = u \tag{7.43}$$

$$\ddot{x} = -\frac{F_w \sin\theta + F_e \sin\theta + \phi}{m} \tag{7.44}$$

$$\ddot{z} = \frac{F_w \cos\theta + F_e \cos\theta + \phi}{m} - g \tag{7.45}$$

$$\ddot{\theta} = \frac{F_w l_w - F_e(l\cos\phi + l_e)}{I} \tag{7.46}$$

where $\dot{x}_w$ and $\dot{z}_w$ are the wing velocities in the x and z directions respectively, $\dot{x}_e$ and $\dot{z}_e$ are the elevator velocities in the x and z directions respectively, α_w is the angle of attack of the wing, α_e is the angle of attack of the elevator, F_w is the aerodynamic force exerted on the wing, and F_e is the aerodynamic force exerted perpendicular to the elevator.

7.2.2 Extended Kalman Filter

The first estimator investigated was the Extended Kalman filter, since it is by far the simplest method of the three presented above. However, in order to successfully execute the Extended Kalman Filter, one must ensure that the system is observable. To do this, the observability matrix was computed over the simulated trajectory of an aircraft in the power line's magnetic field.

Observability Analysis

An Observability Analysis can provide valuable insight into the conditioning of the Kalman Filter. A poorly conditioned observability matrix indicates that the Extended Kalman Filter may be inadequate to track a given system's states. The observability matrix can be constructed for each time t as,

$$\mathbf{O} = \begin{pmatrix} H_t \\ H_t F_t \\ H_t F_t^2 \\ H_t F_t^{n-1} \end{pmatrix} \tag{7.47}$$

where H_t is the measurement gradients matrix and F_t is the process gradients matrix. If the rank of this matrix is ever less than the total number of states in the system, then the system is not observable. Occasionally, even though the matrix is still full rank, the difference between the largest and smallest eigenvalues/singular values is so great that the observability matrix will effectively loose rank. To better characterize this effect, the condition of the observability matrix was defined as follows:

$$cond(\vec{\mathbf{O}}) = \frac{\lambda_{max}}{\lambda_{min}} \tag{7.48}$$

The condition of the observability matrix was then plotted over the aircraft's trajectory, and is displayed in Figure 7.3. It is important to notice how the observability improves as the aircraft moves closer to the wire. This analysis does indicate that the system is in fact observable, and indicates that the Extended Kalman Filter will be successful.

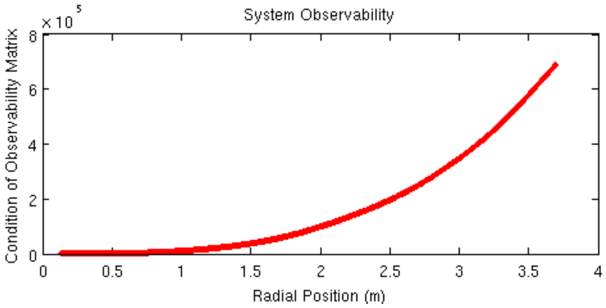

Figure 7.3: Observability Analysis

Simulation of EKF with Glider Process Model

Initially, the Extended Kalman Filter was applied using only the absolute value of the magnetic field signal and a very accurate aircraft model. Even in throwing away the phase information, tracking was shown to be successful in simulation as displayed in Figure 7.4. Such results were not expected and they testify to the strength of recursive Bayesian estimation.

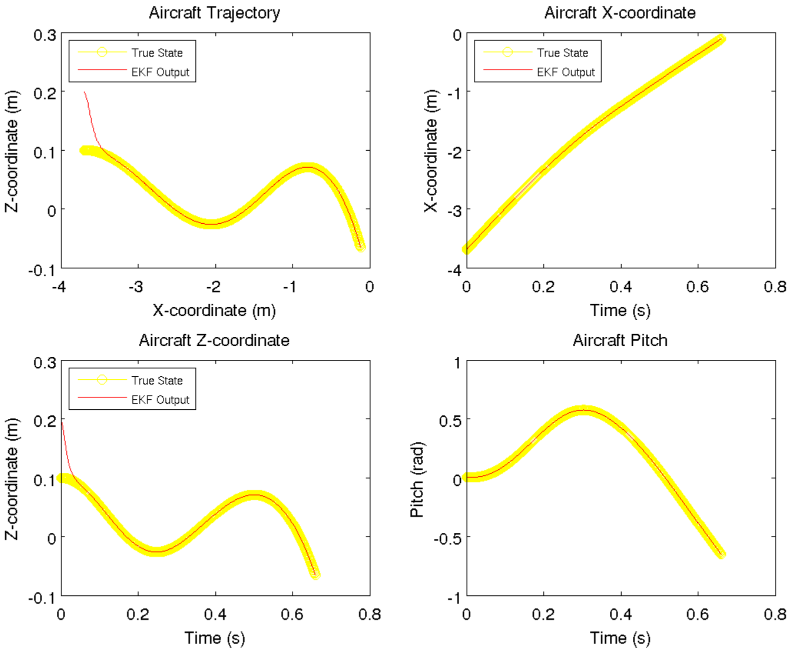

Figure 7.4: Extended Kalman Filter Simulation

Simulation of EKF with Double Integrator Process Model

To test the performance of the EKF, the system model was changed to that of a double integrator and the overall noise of the system was increased slightly. Sure enough, as the model was changed to a simple double integrator and the estimator was required to reject more noise, the Extended Kalman Filter failed, as shown in Figure 7.5.

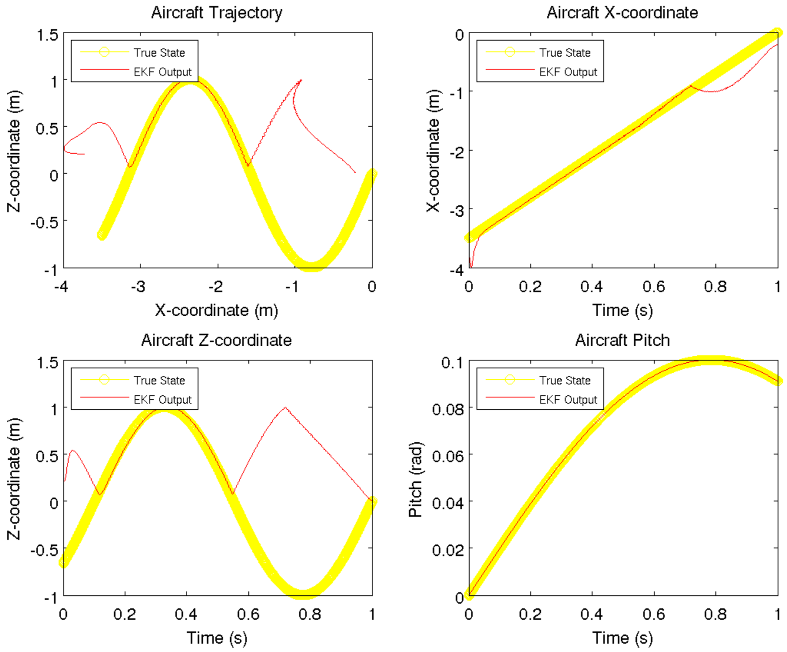

Figure 7.5: Extended Kalman Filter Simulation with Double Integrator Process Model

It is important to note that the state estimation failed as hypothesized at the zero-crossing due to the phase-amplitude ambiguity.

7.2.3 Unscented Kalman Filter and Particle Filter

Since the extended Kalman filter exhibited failure modes, both the Unscented Kalman Filter and the Particle Filter were implemented in simulation to determine if these more advanced methods could overcome the problematic effects of ambiguous measurements. In these investigations, the absolute magnetic field values were used as measurements while the double integrator served as the process model. However, when implemented, both the Unscented Kalman Filter and the particle filter demonstrated similar failure modes as shown in Figures 7.6 and 7.7.

7.3 Phase Tracking

In order to remedy the failure modes from ambiguous field positions, methods of incorporating measurement phase into the state estimators were investigated. It was reasoned

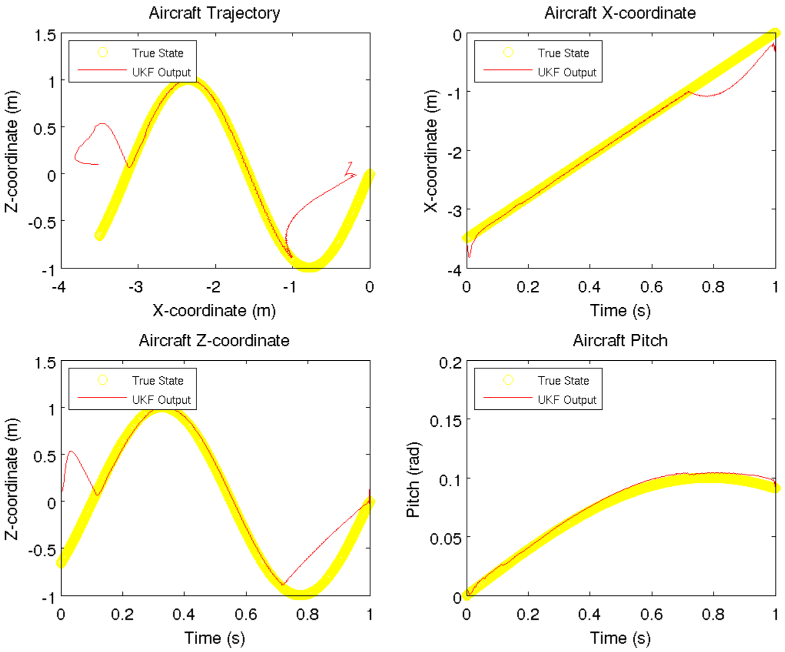

Figure 7.6: Unscented Kalman Filter Simulation with Double Integrator Process Model

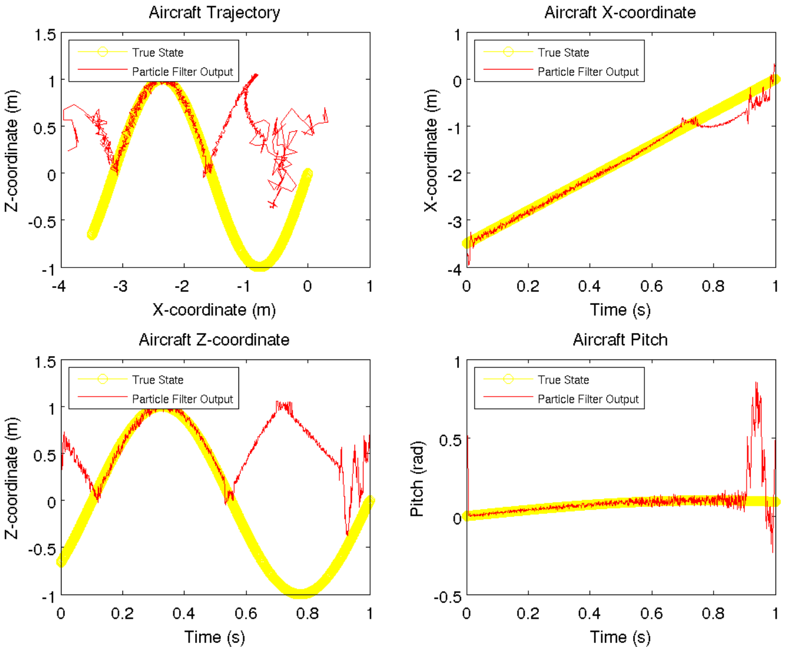

Figure 7.7: Particle Filter Simulation with Double Integrator Process Model

that such an approach would reduce the ambiguous states from eight to four. In this way, adjacent octants would no longer include ambiguous position measurements, and for this reason, it was hypothesized that the overall tracking robustness would be greatly improved.

7.3.1 Minimum Error Tracking

One approach to incorporating phase information involved measuring the phase difference, ϕ_e, between the x and z magnetic field vectors, evaluating all possible ambiguous cases, and selecting the case that minimizes the measurement error. This technique, known as Minimum Error Tracking, was formulated as follows:

Given the current state $\mathbf{x_t}$ and the current measurement value $\mathbf{y_t}$, compute

$$B_x = |y_x(\mathbf{x_t})| \tag{7.49}$$

$$B_z = |y_z(\mathbf{x_t})| \tag{7.50}$$

If $\phi_e < \pi$

$$\begin{aligned} B_{x,a} &= B_x \\ B_{z,a} &= B_z \\ B_{x,b} &= -B_x \\ B_{z,b} &= -B_z \end{aligned} \tag{7.51}$$

Otherwise if $\phi_e \geq \pi$

$$\begin{aligned} B_{x,a} &= -B_x \\ B_{z,a} &= B_z \\ B_{x,b} &= B_x \\ B_{z,b} &= -B_z \end{aligned} \tag{7.52}$$

After considering the value of ϕ_e, we can then construct the vectors

$$\mathbf{B_a} = \begin{pmatrix} B_{x,a} \\ B_{z,a} \end{pmatrix} \tag{7.53}$$

$$\mathbf{B_b} = \begin{pmatrix} B_{x,b} \\ B_{z,b} \end{pmatrix} \tag{7.54}$$

Next, the two ambiguous error cases can be computed as

$$\mathbf{e_a} = \mathbf{B_a} - \mathbf{y_t} \tag{7.55}$$

$$\mathbf{e_b} = \mathbf{B_b} - \mathbf{y_t} \tag{7.56}$$

Finally, the minimum error can be chosen by comparing the norm of e_a and e_b. It is this minimum error which is then used in the Extended Kalman Filter. This technique was implemented in simulation and the results can be observed in Figure 7.8. Although this method seemed unaffected by the measurement ambiguities, under conditions of high system noise, a great deal of position measurement would result.

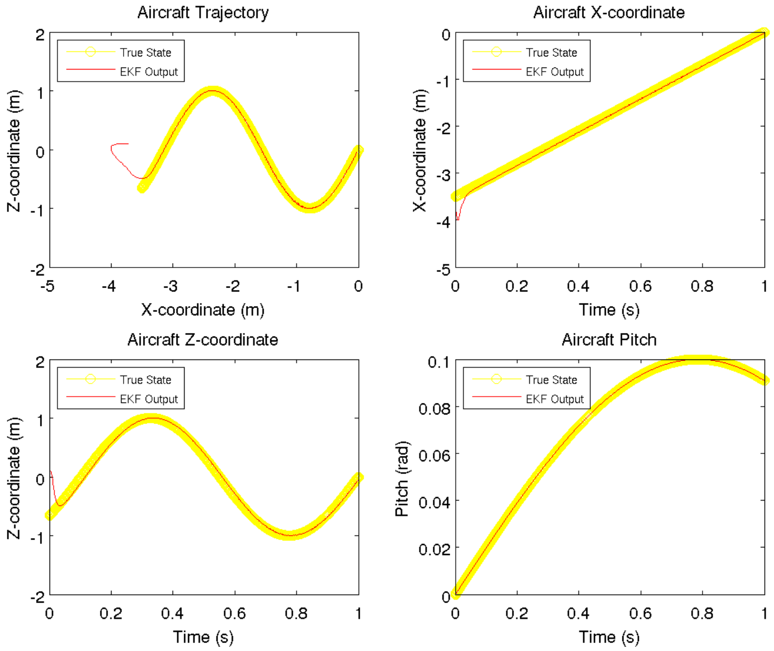

Figure 7.8: Simulation of Extended Kalman Filter with Minimum Error Tracking

7.3.2 Complex Signal Tracking

The second method of reducing ambiguity involves incorporating the real and imaginary components of the magnetometer signal directly into the measurement model. In this way, the magnetic field model can be written as,

$$B_{x,c} = B_x cos(\phi) \tag{7.57}$$

$$B_{x,s} = B_x sin(\phi) \tag{7.58}$$

$$B_{z,c} = B_z cos(\phi) \tag{7.59}$$

$$B_{z,s} = B_z sin(\phi) \tag{7.60}$$

$$\phi = mt + b \tag{7.61}$$

where ϕ is the phase, m and b are linear parameters, and t is time.

In this way, m and b can be treated as states in the process model which vary slowly with time. The augmented state vector can then be written as

$$\dot{\mathbf{X}} = \begin{pmatrix} \dot{\mathbf{x}} = f(\mathbf{x}) \\ \dot{m} = 0 \\ \dot{b} = 0 \end{pmatrix} \tag{7.62}$$

The key here for reducing ambiguity lies in realizing that the phase for both magnetic field vectors is the same. This method was also implemented and the results can be observed in Figures 7.9 and 7.10.

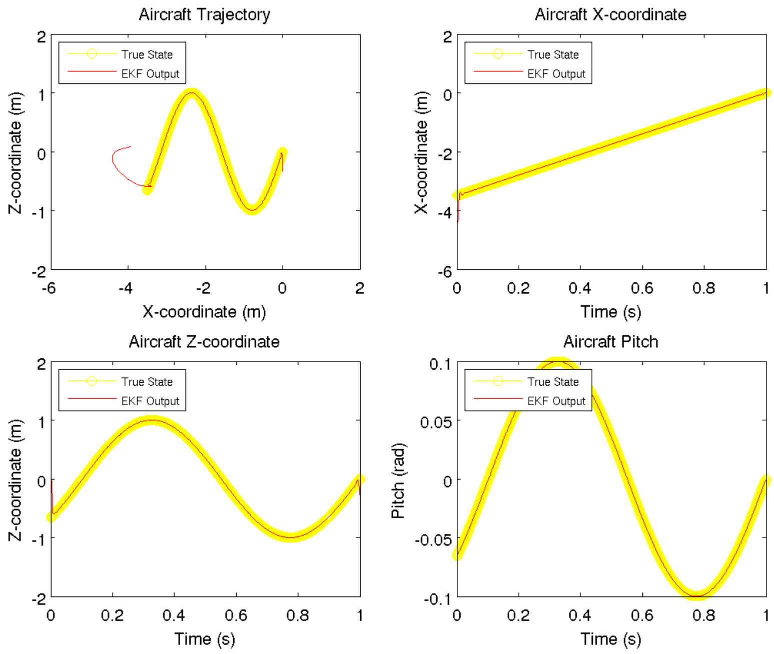

Figure 7.9: Simulation of Extended Kalman Filter Tracking using Complex Measurements

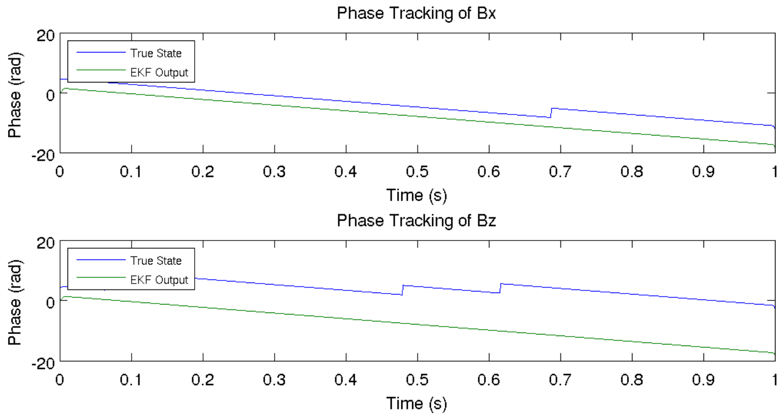

Figure 7.10: Simulation of Extended Kalman Filter Phase Tracking

7.4 Experimental Results

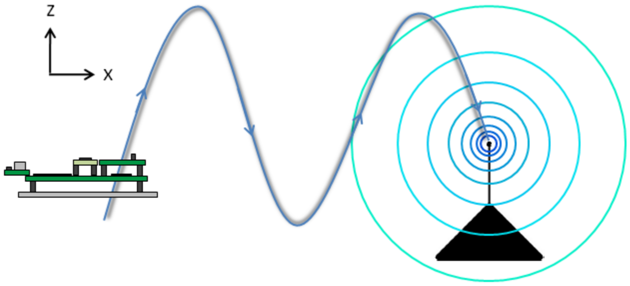

Figure 7.11: Depiction of Trajectory Followed By Sensor Sweep

Once successful position tracking was demonstrated in simulation, data was collected using the preliminary sensor hardware. A sinusoidal-like trajectory (see Figure 7.11) was traced through x and z positions in the field while both the magnetometer data and Vicon motion capture data were collected. Once the data was collected, the extended Kalman filter with complex signal tracking was applied using the infinite parallel wire magnetic field model. However, as seen in Figure 7.12, this model did not prove to be accurate enough far from the wire. At 1.5 meters from the center of the current loop, the error is almost a half meter. Although the state estimation would provide position estimates, these values would be extremely inaccurate especially at the beginning of the aircraft's perching trajectory, where the vehicle has the most control authority. However, instead of answering the second research question based on these results, an effort was made to develop a more accurate magnetic field model.

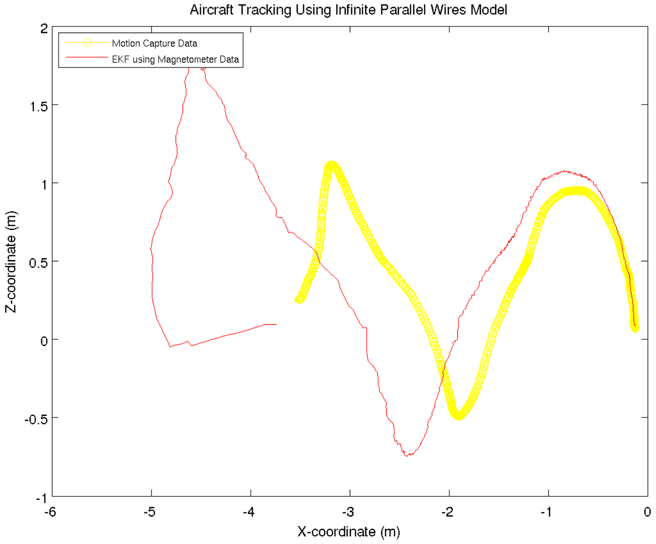

Figure 7.12: EKF using Infinite Parallel Wire Model

Chapter 8

Improved Magnetic Field Model

If no effort was made to revise the infinite parallel wire model, the answer to the second research question, "Can a model of the powerline's magnetic field be used to obtain position measurements?" would be "no". It is evident from the final plot in the previous chapter, that the model is only valid very close to the current loop. Fortunately, however, this original model was an approximation. Although it did provide substantial intuition about the geometry of the magnetic field, it neglected both the finite length of the main wires as well as the impact of the end wires.

8.1 Rectangular Current Loop Model

A more accurate model of the magnetic field from the full rectangular current loop can be derived by taking into consideration the finite nature of the wires and by incorporating the short end wires. However, in order to construct this model, one must employ the Biot-Savart Law.

8.1.1 Biot-Savart Law

To model the rectangular current loop, the Biot-Savart law was applied as shown in Figures 8.1 and 8.2, since this law allows one to compute the magnetic field generated by an infinitesimal section of wire. The Biot-Savart Law can be formulated as,

$$\mathbf{B} = \int \frac{\mu_0 I d\mathbf{l} \times \mathbf{r}}{4\pi r^3} \tag{8.1}$$

where μ_0 is the magnetic permeability of free space, I is the current in the wire, $\mathbf{l}$ is the vector from the origin of the wire to the infinitesimal wire segment of interest in the direction of the current, and $\mathbf{r}$ is the vector from the infinitesimal wire segment to the aircraft location. In figure 8.2, x_0, y_0, and z_0 define the position of the aircraft, and $\hat{\mathbf{i}}$, $\hat{\mathbf{j}}$, and $\hat{\mathbf{k}}$ represent the Cartesian unit vectors.

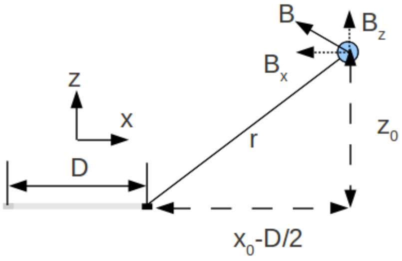

Figure 8.1: Side View of Rectangular Current Loop

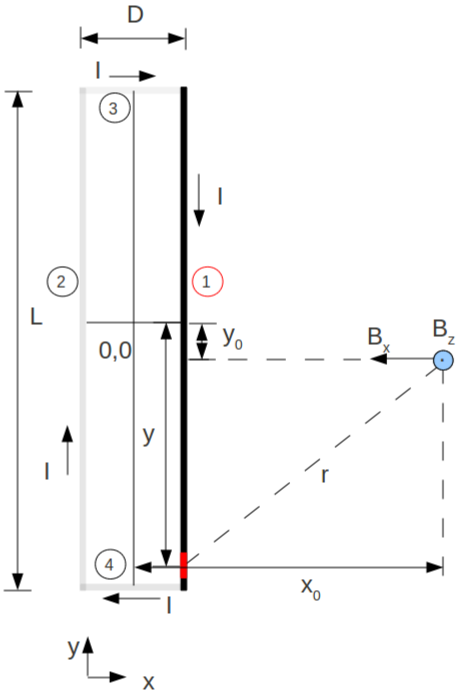

Figure 8.2: Top View of Rectangular Current Loop

In the case of the first wire, as shown in Figure B.2,

$$\mathbf{l} = -y\hat{\mathbf{j}} \tag{8.2}$$

$$d\mathbf{l} = -dy\hat{\mathbf{j}} \tag{8.3}$$

$$\mathbf{r} = (x_0 - \tfrac{D}{2})\hat{\mathbf{i}} + (y_0 - y)\hat{\mathbf{j}} + z_0\hat{\mathbf{k}} \tag{8.4}$$

$$d\mathbf{l} \times \mathbf{r} = (-z_0\hat{\mathbf{i}} + (x_0 - \tfrac{D}{2})\hat{\mathbf{k}})dy \tag{8.5}$$

Substituting into the Biot-Savart Integral gives,

$$\mathbf{B_1} = \int_{-\frac{L}{2}}^{\frac{L}{2}} \frac{\mu_0 I(-z_0\hat{\mathbf{i}} + (x_0 - \frac{D}{2})\hat{\mathbf{k}})dy}{4\pi(\sqrt{(x_0 - \frac{D}{2})^2 + (y_0 - y)^2 + z_0^2})^3} \tag{8.6}$$

which is a vector containing the x and z components of the magnetic field, $B_{x,1}$ and $B_{z,1}$, as a function of position from first wire. It is important to note that this integral can be evaluated analytically.

In the same way, integrals can be constructed for wires 2,3, and 4 as

$$\mathbf{B_2} = \int_{-\frac{L}{2}}^{\frac{L}{2}} \frac{H(z_0\hat{\mathbf{i}} - (x_0 + \frac{D}{2})\hat{\mathbf{k}})dy}{(\sqrt{(x_0 + \frac{D}{2})^2 + (y_0 - y)^2 + z_0^2})^3} \tag{8.7}$$

$$\mathbf{B_3} = \int_{-\frac{D}{2}}^{\frac{D}{2}} \frac{H(z_0\hat{\mathbf{j}} - (y_0 + \frac{L}{2})\hat{\mathbf{k}})dx}{(\sqrt{(x_0 - x)^2 + (y_0 + \frac{L}{2})^2 + z_0^2})^3} \tag{8.8}$$

$$\mathbf{B_4} = \int_{-\frac{D}{2}}^{\frac{D}{2}} \frac{H(-z_0\hat{\mathbf{j}} + (y_0 - \frac{L}{2})\hat{\mathbf{k}})dx}{(\sqrt{(x_0 - x)^2 + (y_0 - \frac{L}{2})^2 + z_0^2})^3} \tag{8.9}$$

These integrals can be evaluated to obtain $B_{x,2}, B_{z,2}, B_{y,3}, B_{z,3}, B_{y,4}$ and $B_{z,4}$, which are the vector field contributions from the three remaining wires. The full magnetic field equations then become

$$B_x = B_{x,1} + B_{x,2} \tag{8.10}$$

$$B_y = B_{y,3} + B_{y,4} \tag{8.11}$$

$$B_z = B_{z,1} + B_{z,2} + B_{z,3} + B_{z,4} \tag{8.12}$$

Last of all, we must take into consideration the rotation of the sensor, where R_ϕ is the rotation matrix representing roll, R_θ represents pitch, and R_ψ represents yaw. The measurement equations then become,

$$\mathbf{B'} = R_\phi R_\theta R_\psi \vec{B} \tag{8.13}$$

For the full magnetic field derivation see Appendix B.

8.2 Experimental Results with Revised Model

Once the magnetic field model was developed for a rectangular current loop, this model was incorporated into the Extended Kalman Filter algorithm described previously. The state estimation algorithm was then carried out once again with this new model in place, and the results were much more successful. These results can be observed in Figure 8.3. For multiple trials, the error of the position estimates was plotted with distance from the wire, as can be seen in Figure 8.4. The error in position ranges from a few centimeters at the power line to an average of 20 centimeters at four meters from the current loop. In this way, it has been demonstrated that a model of the powerline's magnetic field can be used to obtain accurate position measurements.

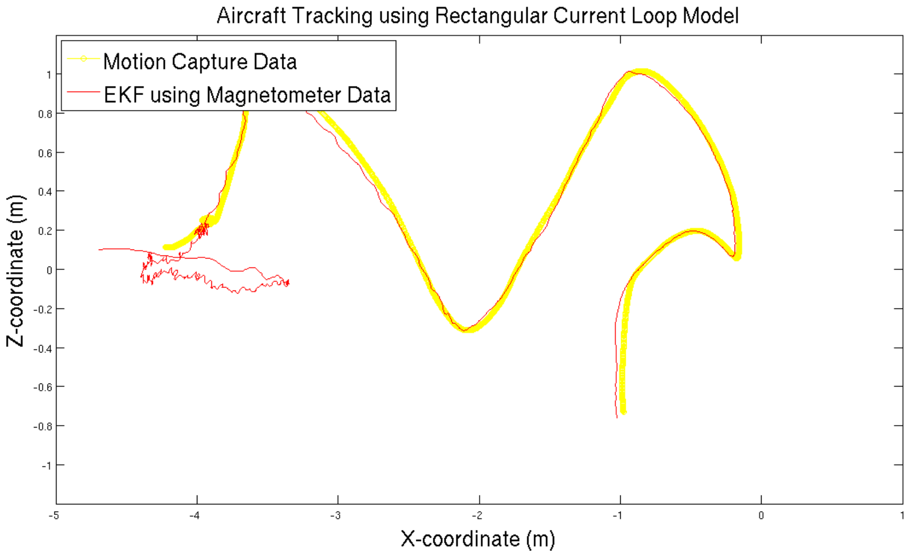

Figure 8.3: Offline Processing of Real Magnetometer Data using the EKF with Phase Estimation

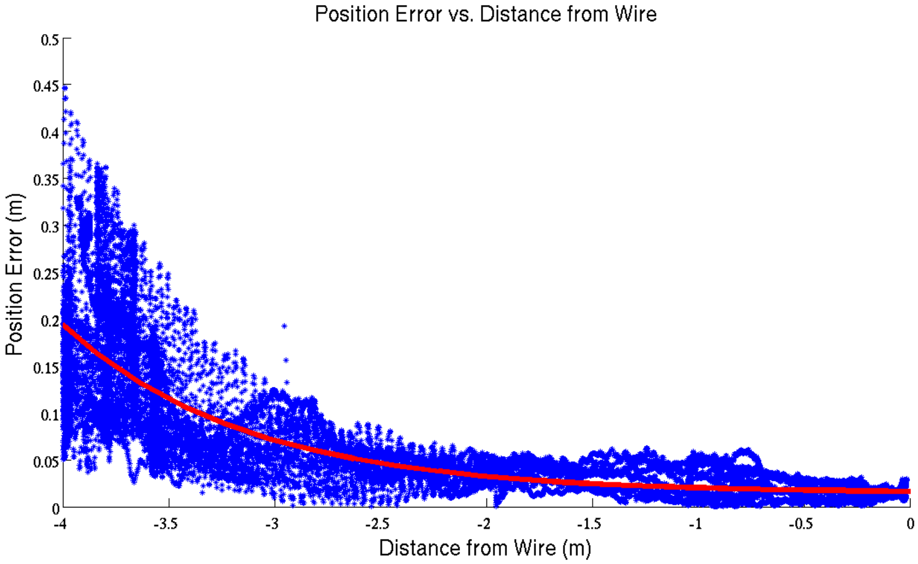

Figure 8.4: Error between Magnetic Field-based Position Estimation and Vicon Motion Capture

Chapter 9

On-board System Development

Once it was demonstrated that accurate position measurements could be obtained from magnetic field measurements, attention was directed at addressing the third research question, “Can fixed wing perching still be achieved with the instrumented aircraft?”. From experimental trials, it was determined that an 80 gram glider of the same size as the one described in Chapter 1, would still be able to achieve lift with 40 grams of additional payload. Therefore, since the original electronics system was well over 40 grams, the first step in answering the third research question involved revising the sensing hardware so that estimation could be carried out on-board the perching aircraft. In the end, the GOSHAWK magnetic sensing system, which can be seen in Figures 9.1 and 9.2, emerged as a low-cost, light-weight solution.

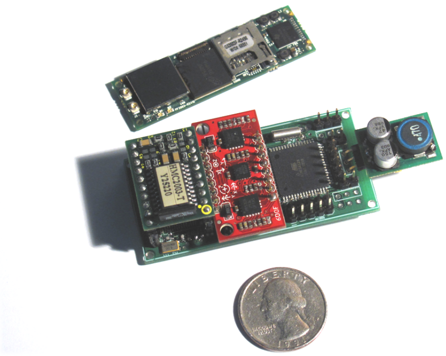

Figure 9.1: Top-View of GOSHAWK Sensing Board

9.1 Hardware Revisions

9.1.1 Legacy Components

To maintain performance consistency, the HMC2003 magnetometer, the ADS1256 analog to digital converter, and the ATMEGA128 were preserved during the revision process. How-

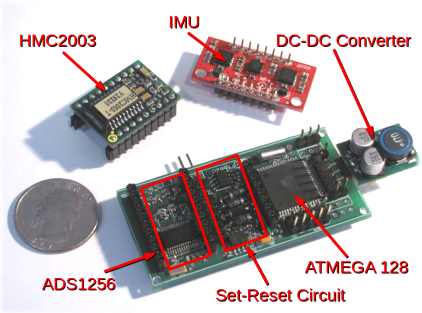

Figure 9.2: Exploded-View of GOSHAWK Sensing Board

ever, a number of additional components needed to be added to achieve a fully functioning on-board system. Furthermore, to reduce system weight, a printed circuit board layout was deemed necessary.

9.1.2 OMAP3 Processor

The TI OMAP3 arm module was selected to carry out the bulk of the state estimation and control processing on-board the aircraft. This 600 MHz processor is utilized in many hand held devices today, and allows one to operate with an embedded version of Linux known as Angstrom. Linux provides incredible opportunities to simplify code development. In many cases, the same code which is written for a PC running Linux can be recompiled for the OMAP3. This makes the OMAP3 very appealing to end users in the research community who must prototype code quickly in C, C++, and Java.

9.1.3 Power Electronics

Unfortunately, the OMAP3 requires a significant portion of power with respect to the other components. Therefore two DC-DC converters, one regulating voltages to 3.3V and the other regulating voltages to 5V were selected to manage the board's power. (Note: The 3.3 volt regulator provides power to the OMAP3 while the 5 volt regulator has the ability to provide power to the aircraft's servo.) Unfortunately, these devices are somewhat heavy, weighing close to 5 grams each. However, the power savings they provide enable the autonomous flight tests possible for up to 20 minutes with the same, lightweight, 300 ma/Hr lithium polymer batteries.

9.1.4 Inertial Measurement Unit

A 6-DOF analog inertial measurement unit from Sparkfun electronics (see Figure 9.2) was selected to provide acceleration and angular rate information for the magnetic sensor board. A simple linear Kalman filter was developed to keep track of the pitch angle of the aircraft. This filter tracked pitch by integrating the gyro measurements and correcting for the bias drift of the gyros by using measurements from the accelerometer. As expected, in high acceleration environments, such as the perching maneuver, this method failed. For this reason, when the sensor unit detects an extremely large accelerometer input, as when the glider is launched, it relies only on the integrated gyro pitch information for a duration of one second before switching back to its normal operation. In this way, accurate pitch information can be obtained during the high acceleration perching maneuvers.

9.2 Printed Circuit Board Design

Once the components were selected and the power management systems were designed, a printed circuit board layout was created using EagleCAD. This layout, show in Figure 9.3, was then sent to Advanced Circuits for fabrication. Once the board was fabricated and populated, the system itself was weighed at 31 grams.

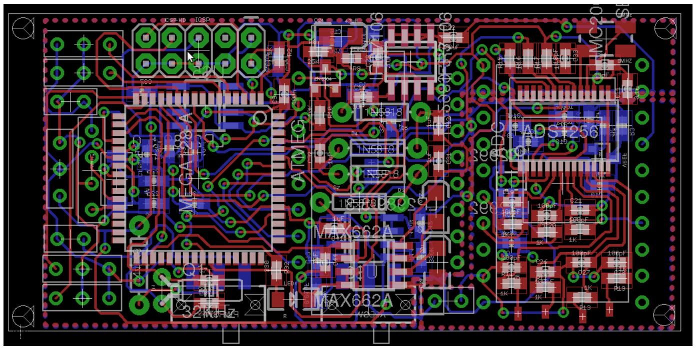

Figure 9.3: GOSHAWK Magnetic Sensing Board

9.3 Magnetometer Signal Corruption

During the course of electronics testing, several discrepancies were observed in the magnetometer sensor data. These discrepancies could be accounted for by two separate factors- magnetic field measurement distortion and signal noise.

9.3.1 Set-Reset Circuit

During the course of the state estimation experiments, it was noticed that occasionally a magnetometer's axis would slip out of calibration. Upon reviewing some of the manufacturer's documentation, it was discovered that occasionally the magnetic domains in magnetoresistive sensors would lose calibration in the presence a large magnetic disturbance. This, in turn, would cause the sensitivity of the sensors to suffer, and occasionally would cause the sensor polarity to flip. To alleviate this problem, a Set-Reset Circuit was developed as per Honeywell's documentation.

The Set-Reset Circuit is essentially a type of power electronics circuit meant send a 4 Amp pulse of current through the magnetoresistive sensor's set-reset strap. The set-reset strap consists of coils that wrap around the magnetoresistive elements and allow a known magnetic field to be applied to the films. Because the straps measure close to 5 Ω of resistance, a 20 V pulse is required. The circuit achieves this essentially by storing charge in a capacitor and then releasing that charge by means of a MOSFET through the coils that surround each magnetoresistive sensor and generating the "corrective" magnetic field. The 20 V source is created by stepping up the 5 volt regulator voltage to 20 volts via a conventional diode charge pump.

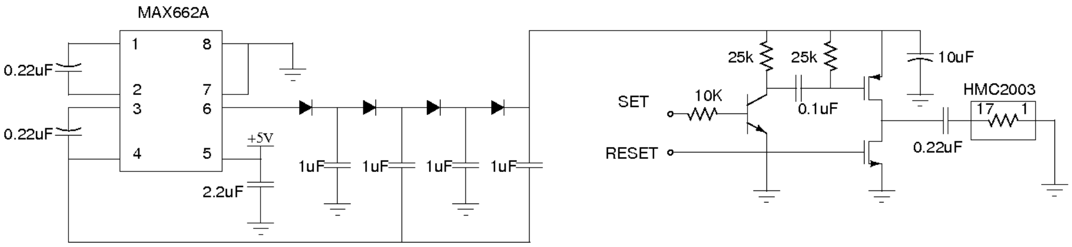

Figure 9.4: Set Reset Circuit with Charge Pump

9.3.2 Power Electronics Noise

When the on-board electronics were undergoing tests, it was noticed that often times there would be varying levels of noise present in the magnetometer data. One of the first sources of this noise was the dc-dc converters since they use high frequency switching to regulate voltage levels. In fact, it was determined that there were different noise levels when the OMAP3 was booting, when it was idle, and when it was running the state estimation program. It was surmised that an increase in current draw from the OMAP3 was actually causing noise to be injected into the voltage supply lines of the magnetometer. This problem was addressed by moving the magnetometer to a separate, extremely small, lithium polymer battery as a power supply. Attempts were also made to improve the EMI filters on the DC-DC converters by designing a LC tank circuit. Although this helped reduce the noise some, it was still not optimal for the level of performance required by the magnetic sensing system.

9.3.3 Antenna Noise

It was also observed that noise was appearing in the magnetometer during wireless data transmission. In this case, the position of the antenna with respect to magnetometer seemed to have an impact on the signal noise level. This problem was addressed by moving the wireless antenna as far from the magnetometer as possible, and orienting the antenna so that the Electromagnetic field was the weakest in the vicinity of the magnetometer.

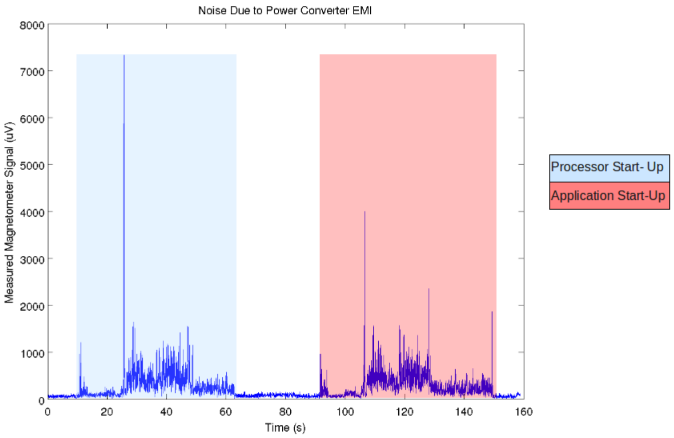

Figure 9.5: Noise Due EMI from Power Converters

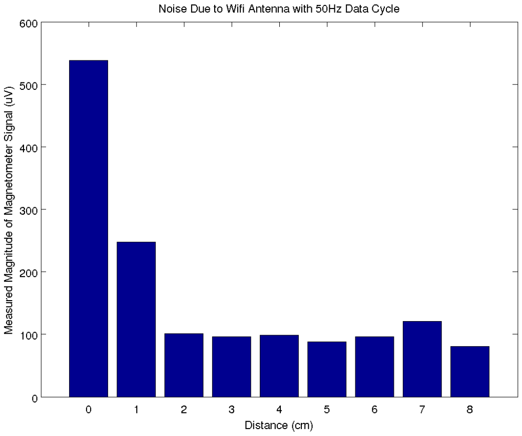

Figure 9.6: Wifi Data Transfer at 50 Hz

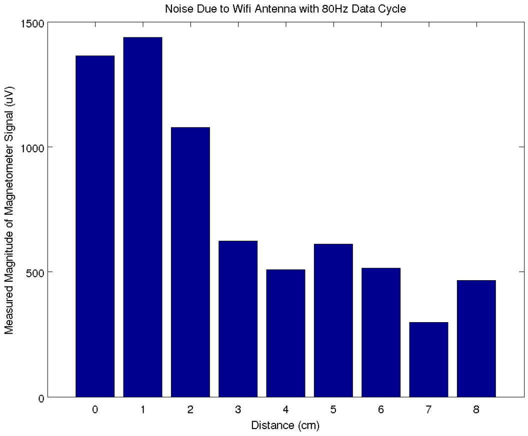

Figure 9.7: Wifi Data Transfer at 80 Hz

9.3.4 Layout Iterations

During the sensor board design process, a number of iterations were made on the system design. The set-reset circuit was eventually included in the layout, and a number of modifications to reduce noise were also made. In the end, however, the performance of the hardware system was at least, if not more, satisfactory than the original prototype.

9.4 System Architecture

The system architecture for the the overall system architecture can be seen in Figure 9.8. It has been divided into two primary parts- low level digital signal processing and the high level computation.

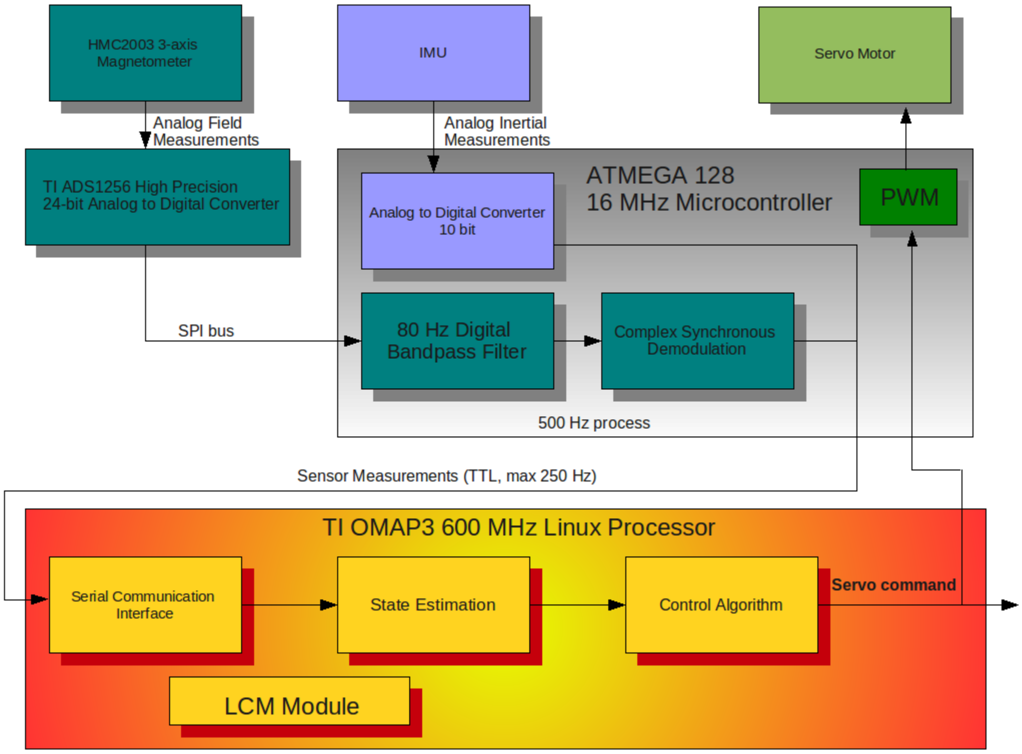

Figure 9.8: System Block Diagram

9.4.1 Low-level Signal Processing

Most of the low-level signal processing occurs on the ATMEGA128 microcontroller. It is here that the magnetometer signals are sampled and undergo the complex synchronous demodulation process previously described. In addition to the complex synchronous demodulation algorithm, a bandpass filter is used to attenuate high frequencies and the magnetometer DC bias before demodulation occurs. A notch filter is also used to remove the 60Hz noise, since it is fairly close in frequency to the 80hz carrier frequency.

It is important to note that when implementing the digital signal processing on board the microcontroller it is necessary to sample at least 4x the carrier frequency in order to prevent the residual $2\omega_c$ terms from aliasing down.

9.4.2 High Level State-Estimation and Control

Both of the computationally intensive state-estimation and control are located as C programs on the Gumstix Overo processor. These programs receive magnetic field and IMU data from the microcontroller at speeds up to 340 Hz, and use that data to control the aircraft during a perching maneuver. To communicate between processes and to stream data over wireless, Lightweight Communications and Marshalling [19] was used.

9.5 On-board System Summary

In conclusion, a light-weight sensing system capable carrying out the localization of an aircraft in a magnetic field was developed. This system, through many iterations, ended up being nearly 10 grams below the payload threshold for the vehicle and contained the computational power to handle advanced state estimation and control algorithms. With the sensor system developed, the next step was to achieve fixed-wing perching with the instrumented aircraft. The entire instrumented aircraft can be seen in Figure 9.9.

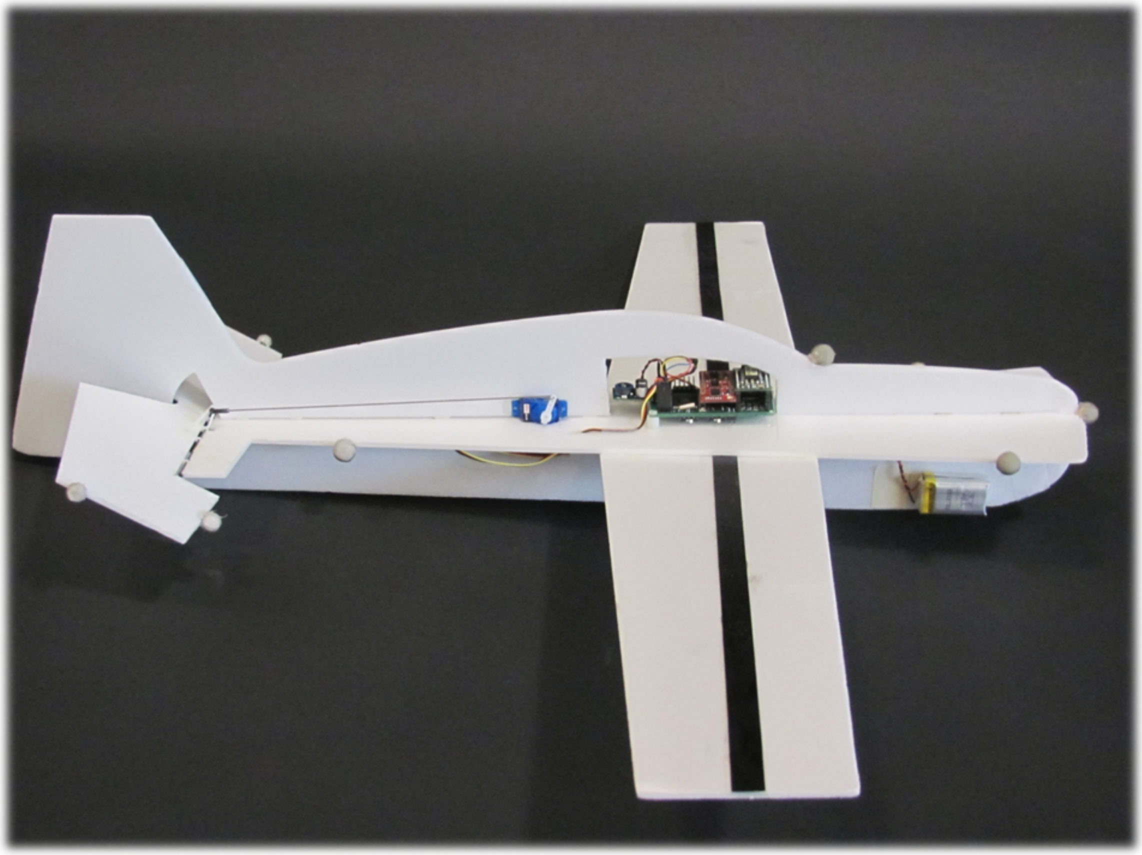

Figure 9.9: The Instrumented Aircraft

Chapter 10

Fixed-Wing Aircraft Modeling

Once the sensing system was revised to meet the payload weight requirements, the next step in answering the question "Can fixed wing perching still be achieved with the instrumented aircraft?", was to develop an optimal trajectory and feedback control design for the heavier, instrumented aircraft. However, the optimization methods used previously failed to find an optimal perching trajectory a flat plat model with a 30 gram payload. However, in experimental, open loop perching trials, successful perching were clearly observed for hand tuned elevator motion. This discrepancy led to the hypothesis that the glider was generating more lift than what was predicted by flat plate theory. Therefore, instead of continuing with the control design, steps were taken to improve the aircraft model.

It is crucial to realize that for both state estimation and model predictive control, the model of the aircraft is of the utmost importance. In state estimation, many methods, such as the Kalman Filter, specify a certain type of probability distribution for the plant. In model-predictive control, the entire feedback design is based solely on the behavior of the aircraft model. Therefore, in both cases, poor modeling can very easily lead to poor performance. For this reason, a substantial amount of time was dedicated to developing an accurate aircraft model.

10.1 Initial Flat-Plate Model

In the early stages of the perching project at MIT, Vicon motion capture was used to develop a model of a fixed wing aircraft. After the data was analyzed, it was deemed that quasi-steady flat-plate theory was accurate enough to represent the data[6].

As stated previously in Chapter 7, from literature, the lift and drag coefficients of flat plate theory are defined as,

$$C_L = 2 \sin \alpha \cos \alpha \tag{10.1}$$

$$C_D = 2 \sin^2 \alpha \tag{10.2}$$

where α is the angle of attack.

The two dimensional dynamic aircraft model that arises when these lift and drag coefficients are applied to both the aircraft elevator and the aircraft wings can be seen in Chapter 7.

10.2 Deviations From Flat Plate Theory

As mentioned above, during the course of the perching experiments, it was hypothesized that the glider did not adhere to flat plate theory in the early stages of the launch. Therefore, to explore this hypothesis, the current version of the glider was launched multiple times at different initial speeds, data was collected using the Vicon motion capture system, and the aircraft's lift and drag coefficients were plotted against flat plate theory. To obtain the accelerations and velocities to required for computing the lift and drag coefficients, the Vicon motion capture position data was differentiated acausally.

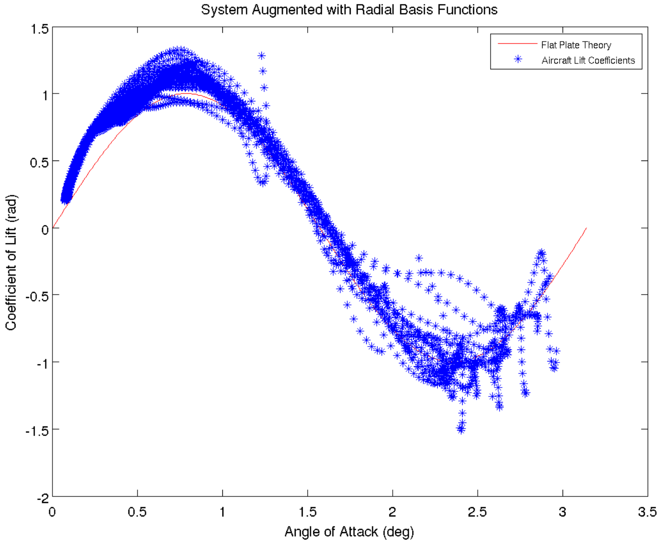

Figure 10.1: Glider Lift Coefficients

As can be observed in Figure 10.1, there is a significant mismatch between flat plate theory and the aircraft's lift coefficient in the early stages of the trajectory. This can also be clearly observed in the aircraft's acceleration data shown in Figure 10.7. There appears to be far more lift present in the early stages of the trajectory than what was predicted by flat plate theory.

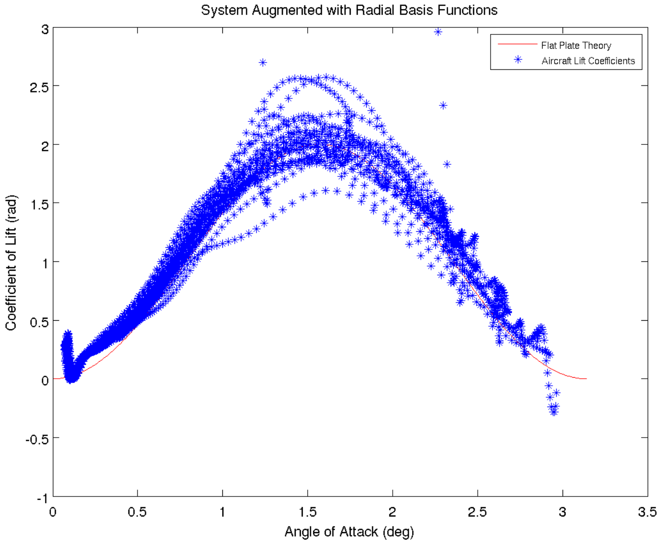

Figure 10.2: Glider Drag Coefficients

10.3 Improved Aircraft Model

10.3.1 Radial Basis Functions

Radial basis functions have been shown to be an extremely powerful tool when attempting to build a dynamic model. The most common radial basis function is the gaussian distribution, whose mean and covariance parameters are nonlinearly involved, but whose magnitude is a linear constant multiplied by the classic normalized gaussian distribution.

10.3.2 Augmented Aerodynamic Coefficients

To improve the aircraft model, an effort was made to augment the aircraft lift and drag coefficients with Guassian radial basis functions, using flat plate theory as a baseline. To achieve this, data was collected by launching the aircraft from 6 m/s to 8 m/s using a handful of optimal elevator trajectories shown in 10.3. To obtain the aircraft accelerations, the position measurements produced by the Vicon motion capture system were differentiated twice and filtering acausally.

Once all the data was collected, the accelerations predicted by flat plate theory were subtracted from the aircraft's accelerations. These residual accelerations were then assumed to contribute to residual lift, drag, and moment coefficients of the entire aircraft. In other words, residual aerodynamic coefficients $C_{l,r}$, Cd, r and $C_{m,r}$ were modeled as functions of both wing angle of attack and elevator position as follows:

$$C_{l,r} = f(\alpha_w, \phi) \tag{10.3}$$

$$C_{d,r} = f(\alpha_w, \phi) \tag{10.4}$$

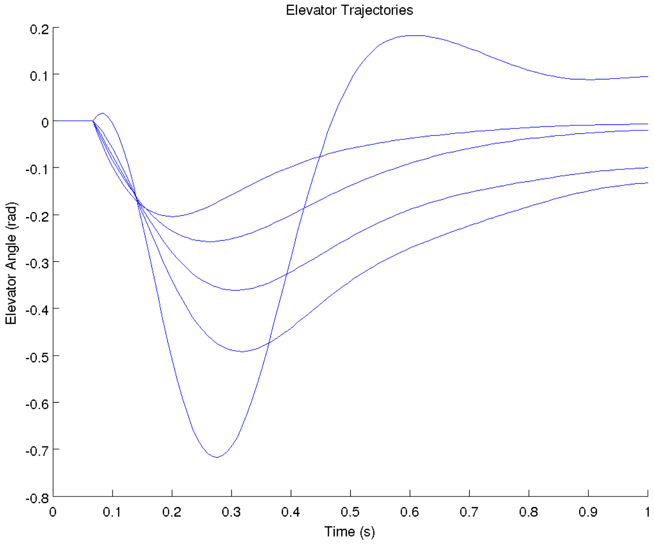

Figure 10.3: Elevator Trajectories

$$C_{m,r} = f(\alpha_w, \phi) \tag{10.5}$$

To fit these functions, Gaussian radial basis functions were specified on a two dimensional grid over a range of wing angle of attacks from 0 to π radians and elevator angles from $-\frac{\pi}{4}$ to $\frac{\pi}{4}$. Least squares was then used to fit the magnitude parameters to develop a better aircraft model.

10.3.3 Regularized Least Squares

In order to use the flat plate theory as a baseline, the classic least squares algorithm needed to be adjusted to minimize the magnitudes of those radial basis functions in the areas where data is sparse. Least squares can be transformed into regularized least squares as follows:

If the θ vector contains the linear components of the radial basis functions, the matrix Φ contains the nonlinear components of the radial basis functions, and the vector y contains aircraft data, then least squares can be written as,

$$0 = \frac{\partial}{\partial \theta}(||\Phi\theta - y||^2 + \gamma||\theta||^2) \tag{10.6}$$

where the term $\gamma||\theta||^2$ uses an arbitrarily chosen constant γ to make the linear parameters θ as small as possible. Using matrix algebra, one can solve for θ as shown in the following equations.

$$0 = (\Phi\theta - y)\Phi + \gamma\theta^T \tag{10.7}$$

$$0 = \theta^T\Phi^T\Phi - y^T\Phi + \gamma\theta \tag{10.8}$$

$$\Phi^T y = (\Phi^T \Phi + \gamma I)\theta \tag{10.9}$$

By modifying least squares in this manner, one minimizes the weights of the Gaussian functions that lie outside collected data set. In this way, least squares can be carried out using data that does not cover the entire parameter space.

10.4 Results

As can be seen in 10.7, the developed model fits the data both in acceleration and in integrated position much more closely than the flat plate model. The lift, drag and moment coefficient plots (Figures 10.4, 10.5, and 10.6) are a projection of the plots along the angle of attack axis. The position trajectory plot, Figure 10.8, compares the forward simulation of the improved model against a data set which is not part of the training data set. As can be observed, the new model tracks incredibly well, while the flat plate theory model does not follow the actual trajectory closely at all. In addition, an examination of the acceleration error computed for the new model also shows a much more clear Gaussian distribution, which is important for many the state estimation methods.

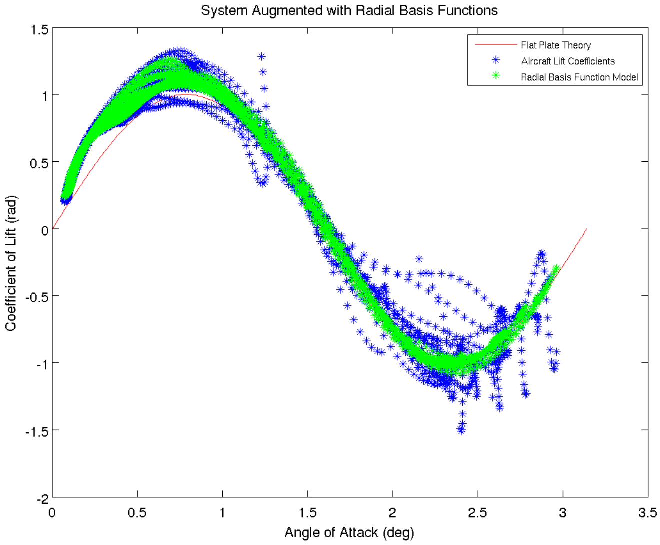

Figure 10.4: RBF fit of Lift Coefficient

10.4.1 Generalization of Modeling Method

Once this modeling method was successfully used to model the original perching aircraft, the method was extended to model a heavier, fully instrumented version of the same aircraft. The results can be observed in 10.9 to 10.11.

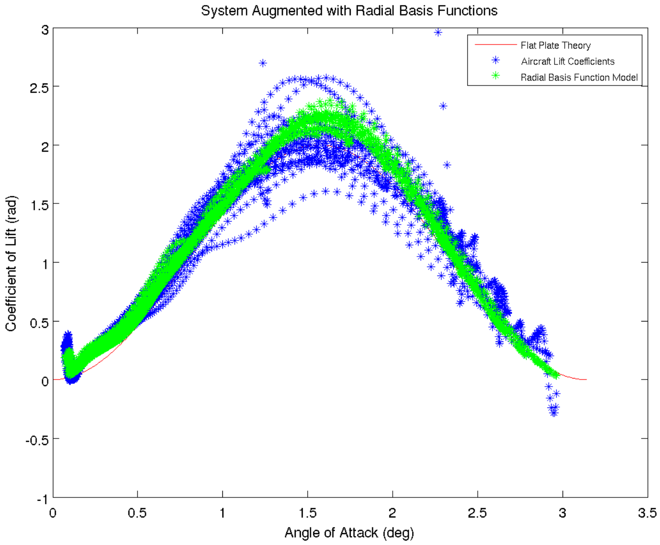

Figure 10.5: RBF fit of Drag Coefficient

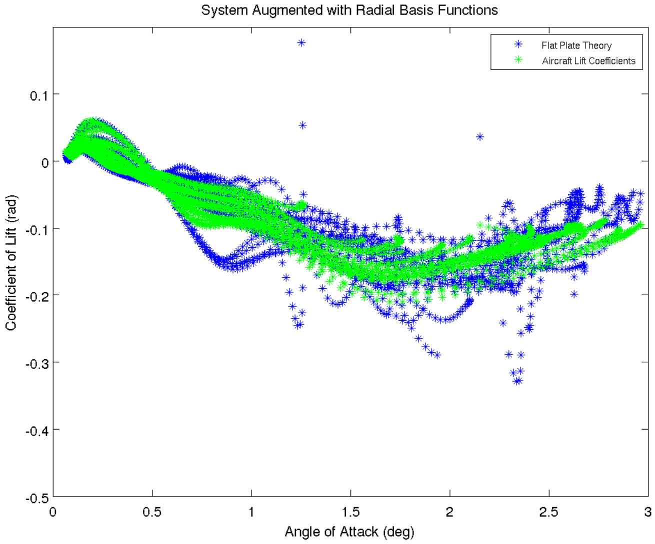

Figure 10.6: RBF fit of Moment Coefficient

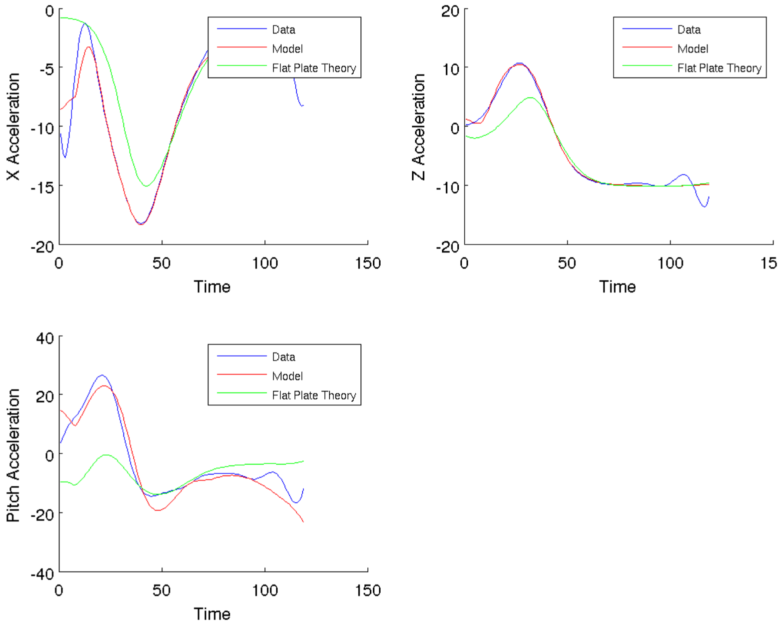

Figure 10.7: Accelerations of Aircraft Models

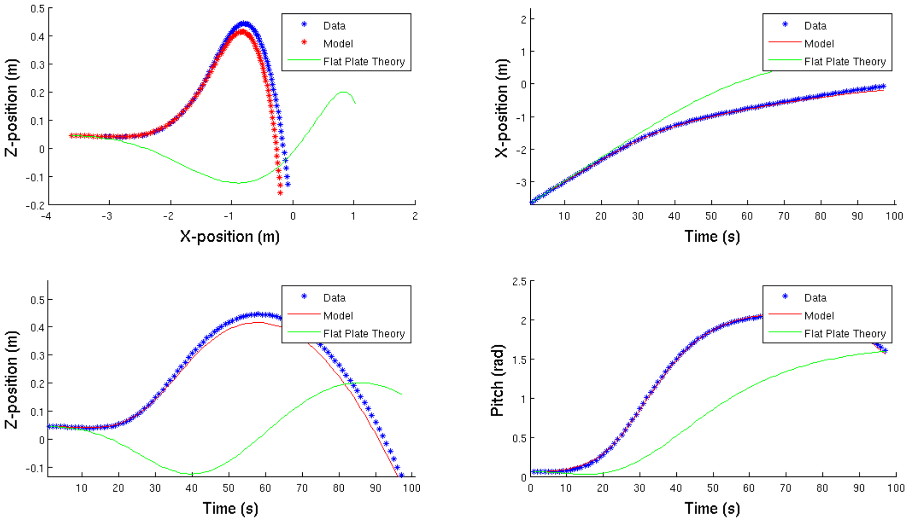

Figure 10.8: Position Trajectories of Aircraft Models

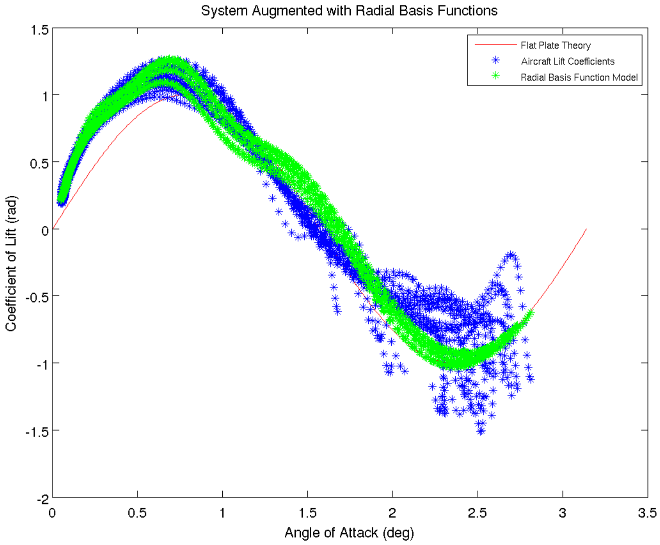

Figure 10.9: RBF fit of Lift Coefficient for Instrumented Glider

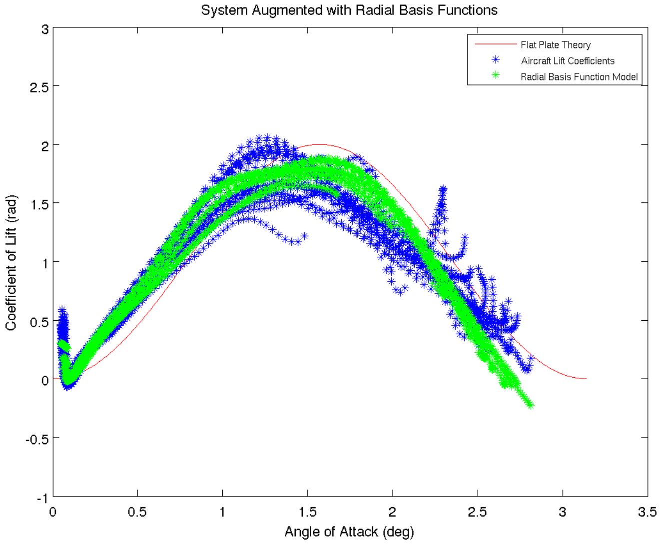

Figure 10.10: RBF fit of Lift Coefficient for Instrumented Glider

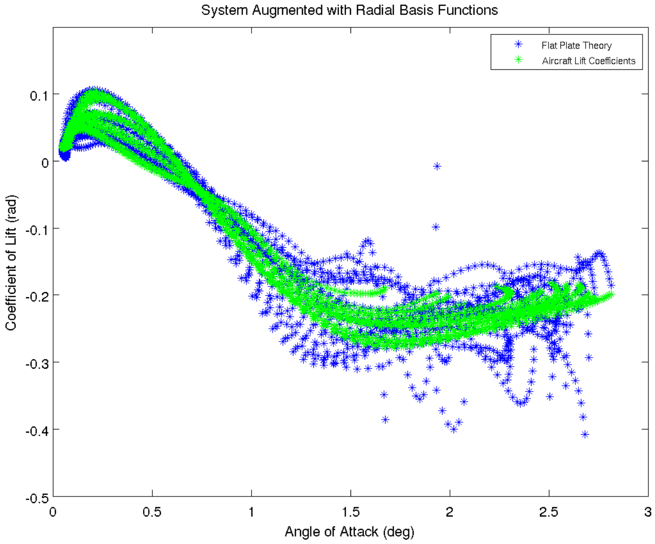

Figure 10.11: RBF fit of Moment Coefficient for Instrumented Glider

10.5 Elevator Modeling

In the initial closed loop perching experiments, delay was not taken into consideration in the elevator model. This section highlights efforst made to improve the aircraft model even further by enhancing the elevator model.

10.5.1 Kinematic Mapping

Due to the slight nonlinear kinematic mapping that exits between the servo and the elevator, a polynomial function was used to map between servo position and elevator position.

10.5.2 Elevator Delay

Upon investigating the aircraft model, it was also noticed that a significant loop delay of 66 ms existed in the actuator command (see Figure 10.13). This delay was measured by sending a command to the elevator and observing the response using the Vicon motion capture system. Because the perching trajectory is so short (0.8 s in duration) it was reasoned that this delay, which is close to 10 percent of the total trajectory, should contribute to the perching performance.

To model the delay, extra states were added to the discretized aircraft model, since delay can be modeled as a linear system in the discrete domain. Because the glider can only update its elevator command every 22 ms, only three extra states were needed. These three extra states allowed for a much more accurate elevator fit, as can be observed in Figures 10.13 and 10.15. The new elevator model can be written as

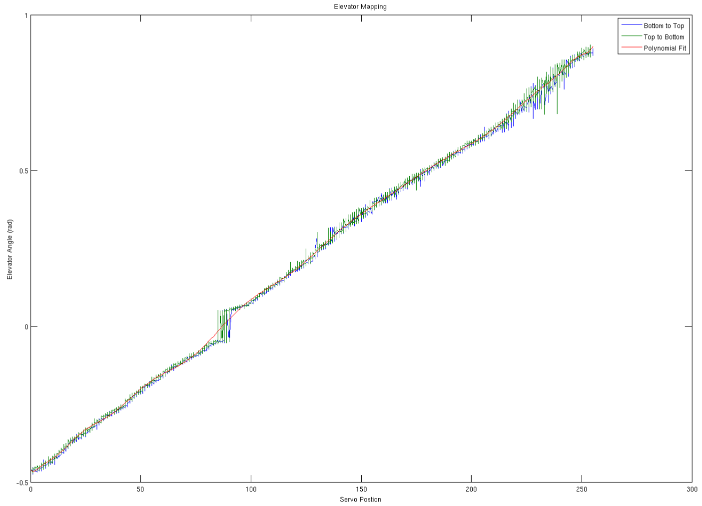

Figure 10.12: Elevator Mapping

$$\dot{\phi}_{k+1} = A\dot{\phi}_k + Bu_k \tag{10.10}$$

where

$$A = \begin{pmatrix} 0 & 1 & 0 \\ 0 & 0 & 1 \\ 0 & 0 & 0 \end{pmatrix} \tag{10.11}$$

$$B = \begin{pmatrix} 0 \\ 0 \\ 1 \end{pmatrix} \tag{10.12}$$

10.6 Conclusions

As can be observed, significant success in aircraft modeling was obtained by merely augmenting the lift and drag coefficients with radial basis functions. It is interesting to note, that as hypothesized, the majority of the difference in the flat plate model arises in the lift coefficients. It is further hypothesized that this additional lift is due to effects of delayed stall. Although delayed stall will not be addressed in this thesis, some preliminary investigations demonstrate that this phenomena could be the source of the discrepancy. Nevertheless, with an improved aircraft model, the research was finally able to proceed in designing a perching trajectory for the instrumented glider.

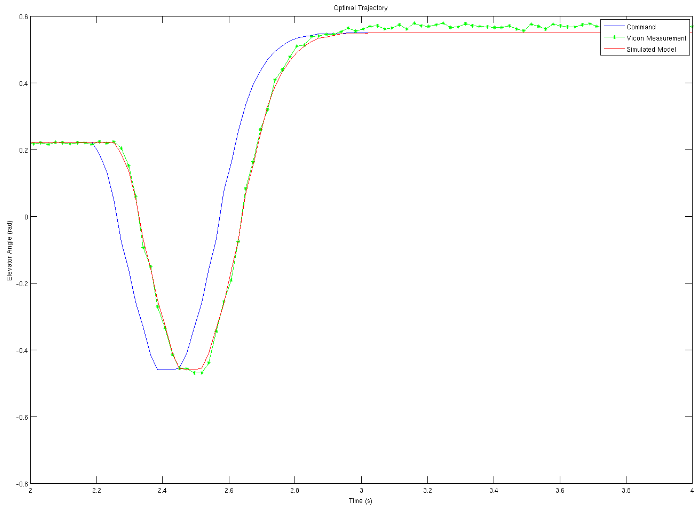

Figure 10.13: Elevator Delay

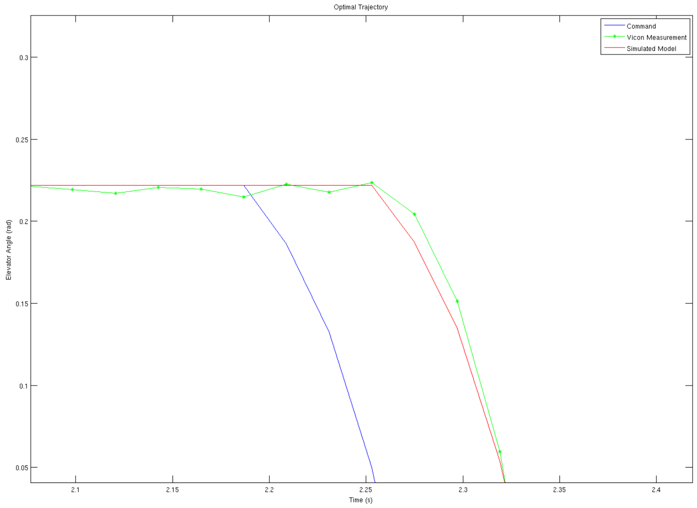

Figure 10.14: Elevator Delay

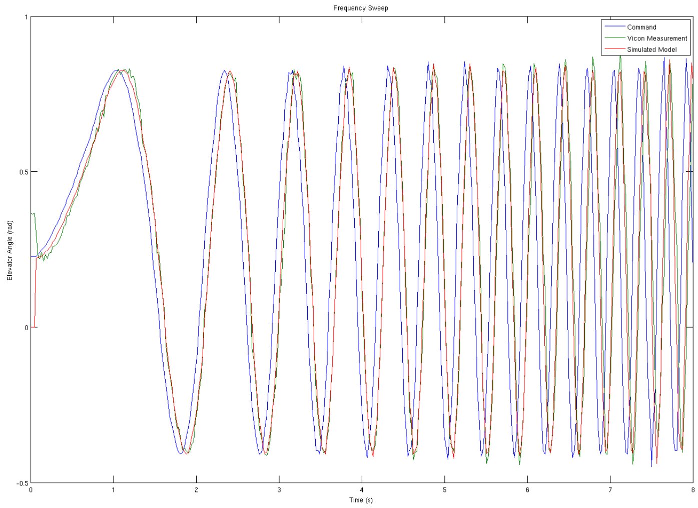

Figure 10.15: Elevator Frequency Sweep

Chapter 11

Control Design

Once an improved aircraft model was obtained, progress could continue to be made in addressing the third research question, "Can fixed wing perching still be achieved with the instrumented aircraft?". In this chapter, we present the methods used to design an optimal trajectory as well as the methods used to construct the optimal feedback design. Furthermore, we demonstrate the successful perching of the uninstrumented aircraft and the instrumented aircraft using the new model. Although the methods presented here do not differ from the perching work previously carried out by the Robot Locomotion Group, the control problem formulation is still crucial to the eventual success of the power line perching project and therefore should be reviewed in light of the new sensing techniques.

11.1 Optimal Trajectory Design

Because the fixed-wing glider is highly underactuated, optimal trajectory design is critical to the solution of the control problem. To carry out this optimal control design, a technique known as back-propagation-through-time, or BPTT, was used. This method allows one to specify a final condition to the optimization problem as a final cost and to determine the fixed tape of elevator actions that minimize that cost by a series of iterative steps.

The formulation of back-propagation-through-time is as follows:

Given a long term cost function,

$$J(x_0) = \int_0^T g(x(t), u(t))dt \tag{11.1}$$

integrate the equations of motion,

$$\dot{x} = f(x, \pi_\alpha(x, t)) \tag{11.2}$$

forward in time from $x(0) = x_0$.

Then, integrate the adjoint equations,

$$\dot{y} = F_x^T y - G_x^T \tag{11.3}$$

back in time from $y(T) = 0$ to $y(0)$, where

$$F_x(t) = \frac{\partial f}{\partial x(t)} - \frac{\partial f}{\partial u(t)} \frac{\partial \pi_\alpha}{\partial x(t)} \tag{11.4}$$

and

$$G_x(t) = \frac{\partial g}{\partial x(t)} - \frac{\partial g}{\partial u(t)} \frac{\partial \pi_\alpha}{\partial x(t)} \tag{11.5}$$

.

In these equations $x(t)$ is the state and $u(t)$ is the input as a function of time. The gradients can then be computed as,

$$\frac{\partial J(x_0)}{\partial \alpha} = \int_0^T (G_\alpha^T - F_\alpha^T y) dt \tag{11.6}$$

.

where,

$$F_\alpha(t) = \frac{\partial f}{\partial u(t)} \frac{\partial \pi_\alpha}{\partial \alpha} \tag{11.7}$$

and

$$G_a(t) = \frac{\partial g}{\partial u(t)} \frac{\partial \pi_a}{\partial \alpha} \tag{11.8}$$

A simple gradient method, shown in the the following equation, was used to optimize the trajectory from the iteration step i to the next iteration step $i + 1$, where u is the tape of actions, J is the cost, and λ is a small constant, chosen using the armijo rule.

$$u_{i+1} = u_i - \lambda \boldsymbol{\nabla} J \tag{11.9}$$

The trajectories which emerge out of this optimal control design are similar to the ones depicted in Figure 11.1.

11.2 Feedback Design

Oftentimes, there are a number of methods one could choose to stabilize an optimal trajectory. However, in this situation where the system is highly underactuated, linear-time-varying LQR stabilization seems to provide the best results. Furthermore, in the future, this method can be easily extended to more advanced control methods such as LQR-Trees. The continuous version for TVLQR is as formulated as follows:

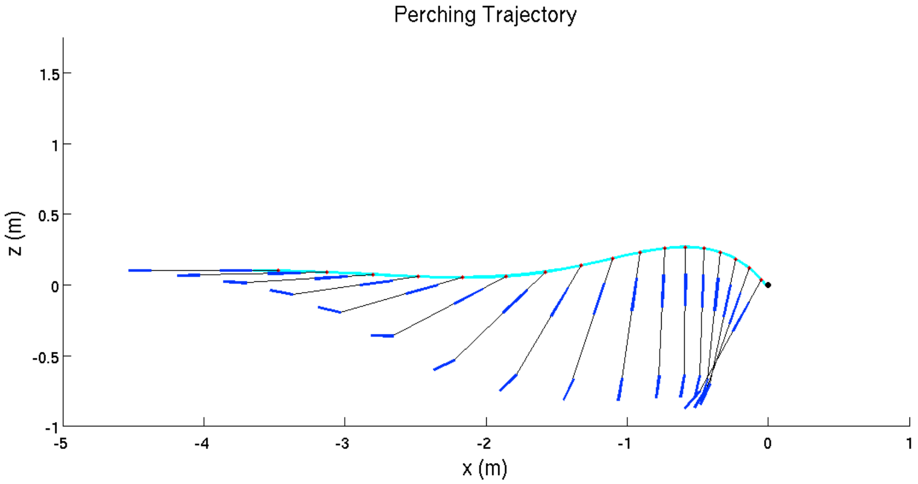

Figure 11.1: Optimal Perching Trajectory

All nonlinear dynamic systems can be represented as a collection of linear systems linearized about a given trajectory. These systems are often written as,

$$\dot{x} = A(t)x + B(t)u \tag{11.10}$$

,

where the A and B matrices vary with time. A trajectory can then be stabilized by minimizing the cost function

$$J(x_0, 0) = x(t_f)^T Q_f x(t_f) + \int_0^T (x(t)^T Q x(t) + u(t)^T R u(t))dt \tag{11.11}$$

.

By assuming $J(x,t) = x^T S(t) x$, the Hamiltonian-Jacobi-Bellman equation can be solved to yield

$$-\dot{S} = Q - S(t)B(t)R^{-1}B^T S(t) + S(t)A(t) + A^T(t)S(t) \tag{11.12}$$

and

$$u(t) = u_0(t) - R^{-1}B^T(t)S(t)x(t) \tag{11.13}$$

.

11.3 Perching Results

Before using the magnetic field sensing system, the perching performance was evaluated using the newly developed models and the current Vicon motion capture system. The figures below highlight the perching results, displaying the final distance between the glider and the perch. A successful landing is designated as a final distance less than 5cm away from the perch. At such distances, the glider is able to hook onto the string or wire. It can be clearly observed that the new model improves the perching performance a great deal, both in distance from the perch and actuator cost. In this way, we determine that we can in fact still perch with the instrumented aircraft so long as the aircraft model is adjusted accordingly.

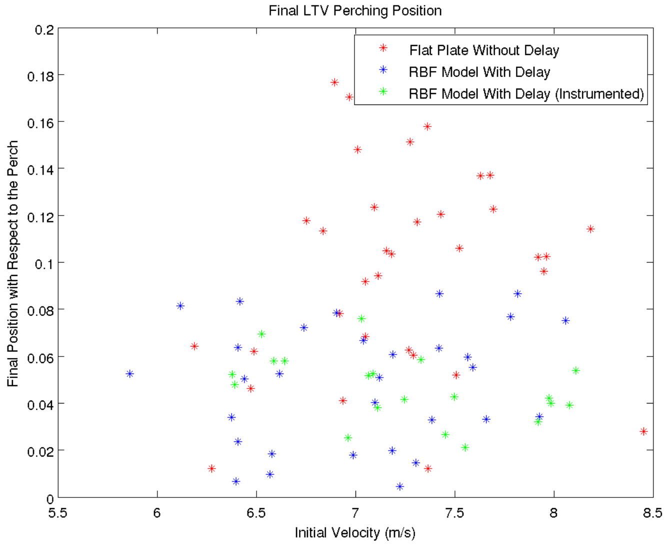

Figure 11.2: Final Perching Position of Various Aircraft Models

Chapter 12

Final Results

12.1 Aircraft Localization Results

With the first three research questions answered successfully, all that remains is addressing the final research question, “Can the aircraft be tracked accurately enough during a perching maneuver?”. To answer this question, an open loop perching trajectory was executed by the instrumented glider and the magnetic field measurements were recorded on board. Initially, the data was merely recorded online and then processed off line. However, eventually, the state estimation algorithms were implemented in C-code and carried out in real time during flight. As seen in Figure 12.1 and 12.2, the state estimation demonstrated tracking with a reasonable accuracy up to 4m from the wire.

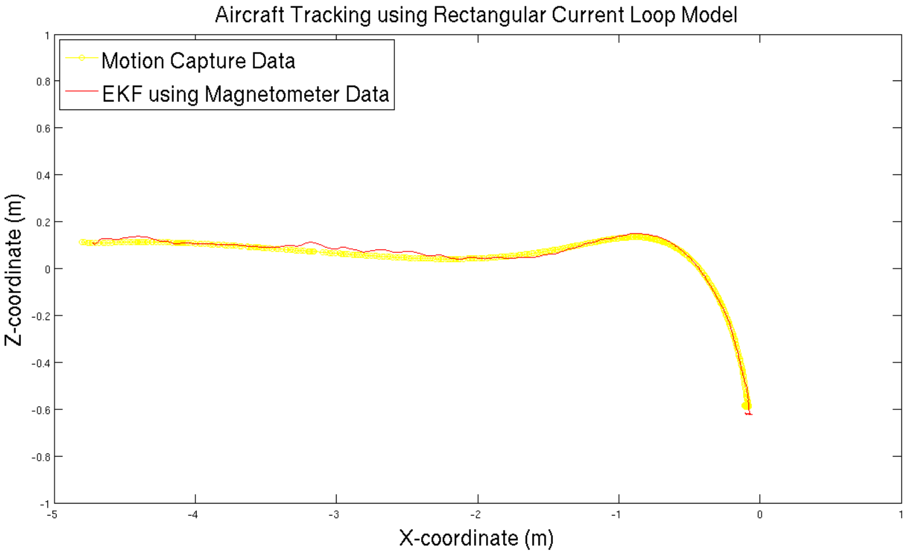

Figure 12.1: Glider Tracking in Position

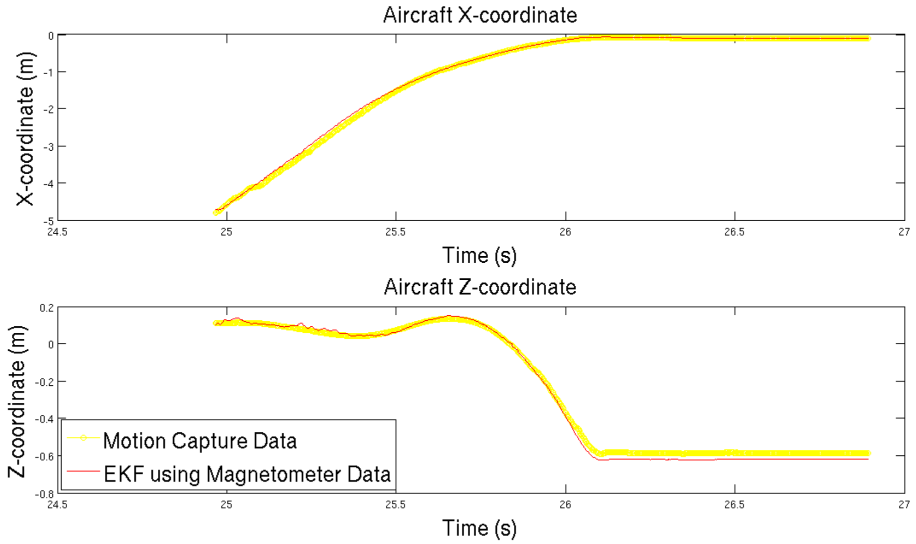

Figure 12.2: Glider Tracking in Position and Time

12.2 Position Error Analysis

To analyze the position error along the perching trajectory, magnetic field data was recorded from multiple open loop perching maneuvers. This data was then compared with the Vicon motion capture data collected concurrently. Figure 12.4 shows a plot of the position error as a function of distance from the wire for a series of perching trajectories. We observe, that at 4 meters from the wire the average error is close to 0.2 meters while at the wire, the error is a only few centimeters.

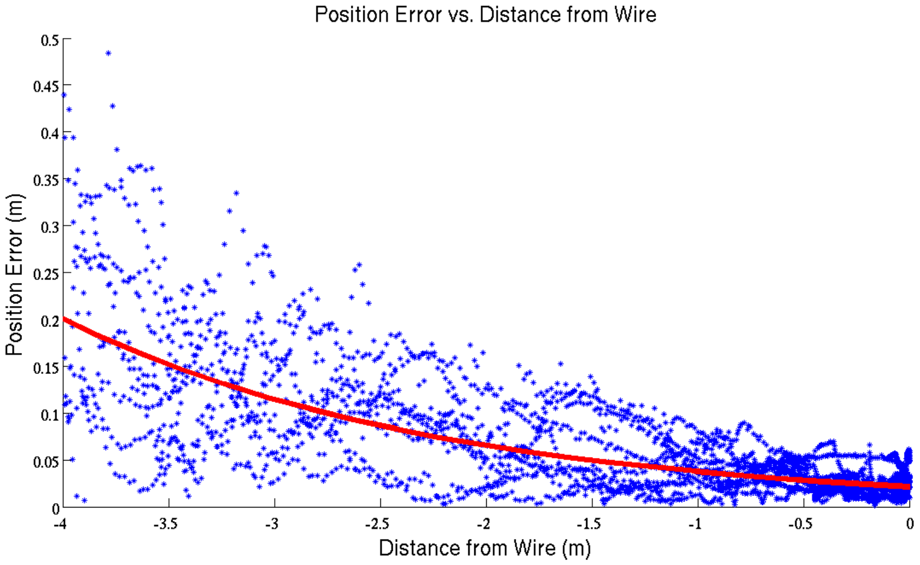

Figure 12.3: Position Estimation Error as a Function of Position

It is difficult to know how drastically this error will impact closed-loop perching performance. However, it is possible to explore the impact of the distorted position measurements by simulating of the closed-loop perching glider and adding in the position measurement distortions. The results of this simulation can be found in Figure 12.4. In this analysis we use the improved glider model to simulate closed loop perching for the case where the magnetic field distortion produces x-position measurements with a magnitude greater than predicted and the case where the distortion produces x-position measurements with a magnitude less than predicted. The perching results for true measurements are also plotted as a reference. It is interesting to note that when the position distortion generates an x position measurement magnitude which is greater than expected, closed loop perching fails. It is hypothesized that the reason for this failure is due to the over estimation of velocity which is a result of these position measurements. To test this theory, the closed loop perching simulation is run where the position measurements are distorted but the velocities are not. In agreement with our hypothesis, these results exhibit successful closed loop perching.

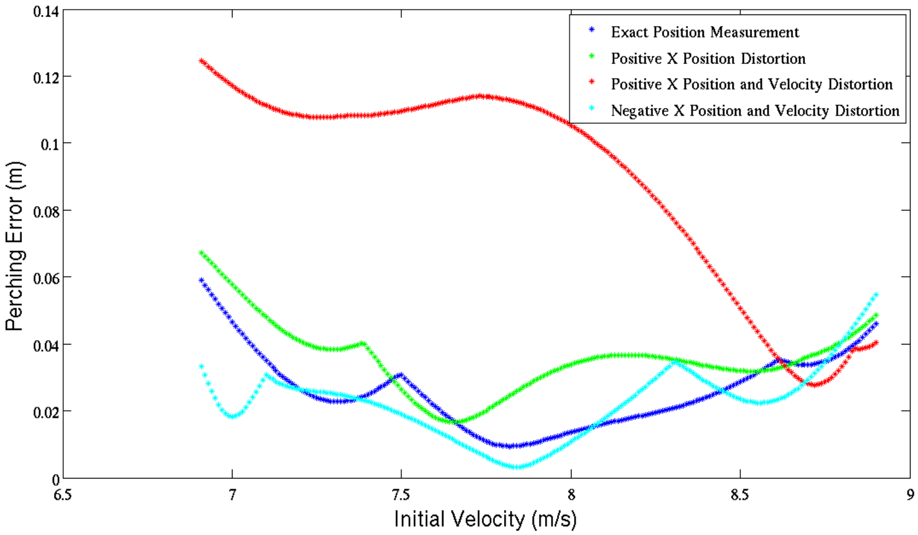

Figure 12.4: Effect of Position Distortion on Closed Loop Perching (Simulation)

12.3 Insights from Error Analysis

By conducting error analysis on the magnetic field-based aircraft position estimation, we observe that for certain field distortions the aircraft should be able to perch successfully. Fortunately, it appears that the magnetic field measurements result in an underestimation of the magnitude of the x-position values. In this case, simulation indicates that closed-loop perching will still be possible. If our magnetic field measurements resulted in an overestimation of the magnitude of the x-position values, placing a high confidence on the acceleration inputs to the double integrator model might help in tracking the correct velocity and thus prevent perching failure. In conclusion, we answer our final research question, asserting

Table 12.1: Comparison of Vicon Motion Capture and GOSHAWK Magnetic Sensing System

Specifications	Vicon Motion Capture	GOSHAWK Magnetic Sensing System
Sample Rate	120 Hz	340 Hz
Accuracy	0.001m	$0.0216e^{0.5576r}$m
Delay	20 ms	17 ms
Power Consumption	1000 W*	0.25 W
Weight	50 kg*	0.030 kg

*Parameters are rough estimates

that it is possible to track the aircraft accurately enough during a perching maneuver. In addition, to facilitate the comparison of our system with Vicon motion capture, we include Table 12.1.

Chapter 13

Discussion

Although this thesis has demonstrated that using the magnetic field generated by a powerline for the localization of a perching aircraft is possible, there are still a number of aspects that must be investigated before powerline perching UAVs become a reality in the field. First of all, the current prototype is still limited primarily to two dimensional state estimation. Secondly, this sensing system has not been yet generalized to an arbitrary powerline configuration, and there are several parameters that are assumed to be known in state estimation experiments which may not be directly measurable in the field. Last of all, the impact of brushless motors on the sensing system is still unknown.

13.1 Three-dimensional Considerations

Initially, this research has limited the movement of the aircraft to two dimensions. Since indoors our aircraft remains almost entirely straight during its 0.8s flight, there has not been a need for three dimensional tracking. However, since our rectangular current loop is a three dimensional field model, it would reasonable to use this model to track longitudinal position. Furthermore, with some slight modifications, aircraft roll and yaw could also be tracked.

13.1.1 Roll Tracking

To keep track of aircraft roll, the acceleration and rate-gyro measurements from the IMU could be combined using a Kalman filter, just as was done in the case of obtaining pitch measurements.

13.1.2 Yaw Measurement

To obtain an approximation of vehicle yaw, once again the magnetic field was assumed to be two finite wires without the end wires. In this way, all of the field could be assumed to be in the x-z plane. By using the third axis of the magnetometer, the yaw angle could be estimated as follows:

$$\gamma = sin^{-1}(\frac{B_y}{B_x}) \tag{13.1}$$

This approximation is demonstrated in the diagram shown in Figure 13.1.

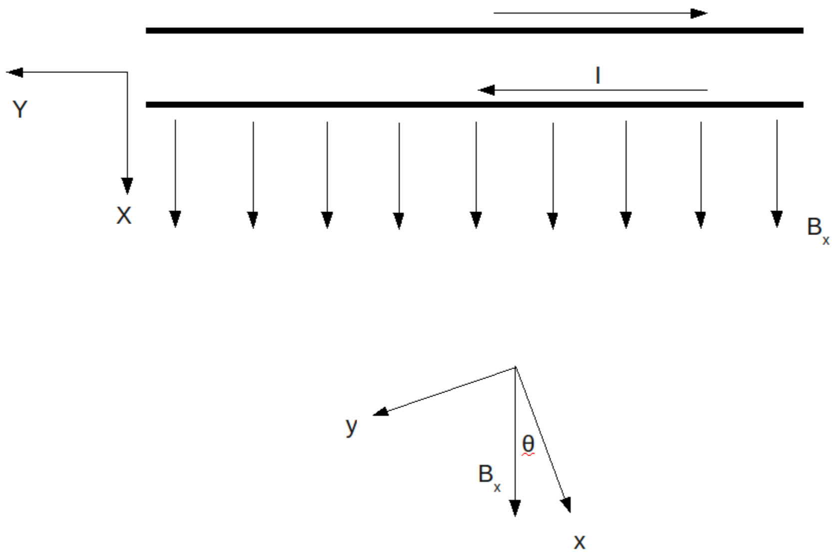

Figure 13.1: Yaw Measurement Diagram

The results of this technique applied to real data is shown in 13.2.

13.2 Real-World Considerations

Though achieving power-line perching with an aircraft has yielded successful results indoors using a powerline replica whose parameters are well known, the question still remains whether or not such a method would actually work on an outdoor powerline. Assuming that the powerlines are spaced far enough apart and are not surrounded by any neighboring magnetic field sources, there are still some issues remaining.

13.2.1 Powerline Current and Distance Between Conductors

Both the current in the powerline and the distance between the wires will almost always be unknown as the aircraft flies in for a landing. For this reason, a method for both

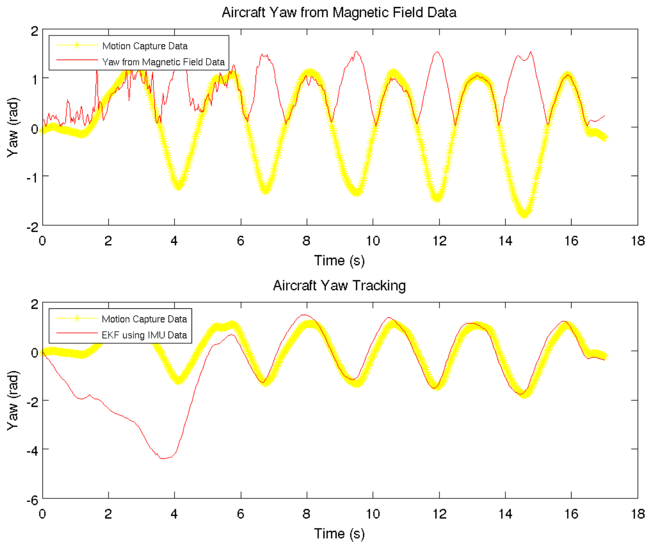

Figure 13.2: Yaw Measurement Verification

estimating the current in the wire and and distance between the wires has been developed in simulation. By using two magnetic sensors, and treating the effective peak current and the spacing between the conductors as a slowly changing state variable, similar to the way in which phase tracking was described earlier in this paper, both values can be accurately estimated as the aircraft approaches the wire. These results can be seen if Figures 13.3 and 13.4.

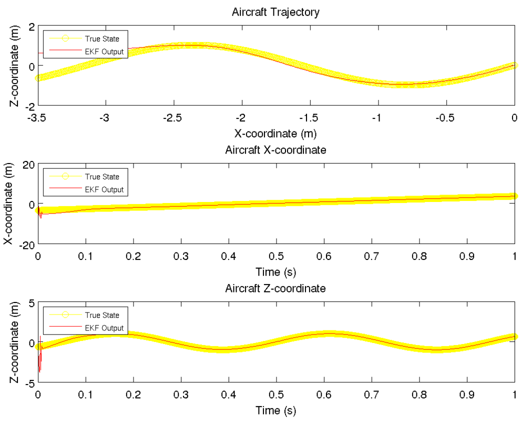

Figure 13.3: State Estimation for Unknown Current and Wire Spacing

13.2.2 Catenary Curve

Since, in the real world, powerlines are strung between two poles, they will exhibit a catenary curve as the wire's own weight causes it to sag. Fortunately, for small angles of deflection,

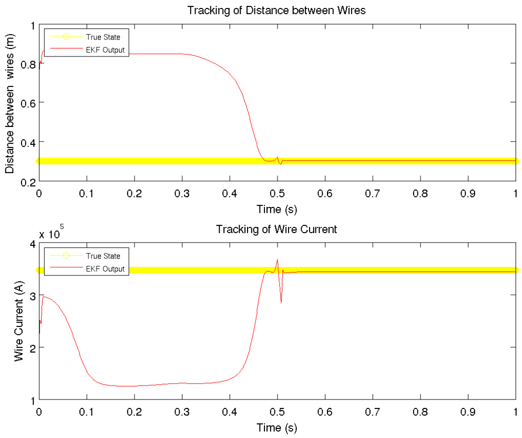

Figure 13.4: Wire Spacing and Current Convergence

the catenary curve, which is merely a hyperbolic cosine, can be approximated as a parabola using a second order Taylor series expansion. This approximation can be seen in Figure 13.5. By rewriting the current carrying element in the Biot-Savart Law to take into consideration this curve, an updated magnetic field model can be developed as follows:

$$\vec{l} = y\hat{\jmath} + acosh(\frac{y}{a} - a)\hat{k} \tag{13.2}$$

By carrying out a Taylor series expansion to the second order, the above curve can be approximated as:

$$\vec{l} = y\hat{\jmath} + \frac{y^2}{2a}\hat{k} \tag{13.3}$$

We now can proceed with the magnetic field derivation as before:

$$d\vec{l} = (\hat{\jmath} + \frac{y/a}{\hat{k}})dy \tag{13.4}$$

$$\vec{r} = x_0\hat{\imath} + (y_0 - y)\hat{\jmath} + (z_0 - \frac{y^2}{2a})\hat{k} \tag{13.5}$$

Taking the cross product between $d\vec{l}$ and $\vec{r}$ yields the following:

$$\vec{r} = ((z_0 + \frac{y^2}{2a} - \frac{yy_0}{a})\hat{\imath} + (\frac{y}{a}x_0)\hat{\jmath} - x_0\hat{k})d\vec{l} \tag{13.6}$$

Substituting into the Biot-Savart Integral leads to:

$$\vec{B} = \int \frac{\mu_0 I d((z_0 + \frac{y^2}{2a} - \frac{yy_0}{a})\hat{\imath} + (\frac{y}{a}x_0)\hat{\jmath} - x_0\hat{k})d\vec{l}}{4\pi(\sqrt{x_0^2 + (y_0 - y)^2 + (z_0 - \frac{y^2}{2a})^2})^3} \tag{13.7}$$

The deflection of this curve could then be estimated on line as a slowly changing state, the same way the current and wire spacing were estimated in simulation. Furthermore, the catenary curve is going to provide an increased field magnitude along the y-axis, which could allow for control over the aircraft's lateral dimension.

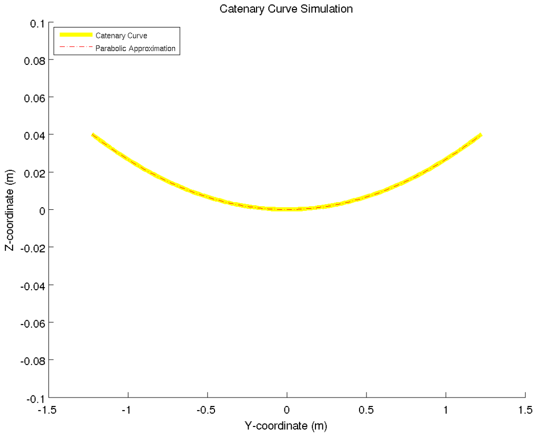

Figure 13.5: Catenary Curve Parabolic Approximation

13.2.3 Poly-Phase Systems

One of the last real-world aspects to be dealt with in regards to the power-line state estimation is localizing the aircraft in a magnetic field generated by poly-phase currents. As mentioned earlier in the report, many powerlines exhibit a system which uses three parallel wires carrying three-phase current. Because of the spacing between the wires, the field will not sum to zero, but each wire will contribute a separate faction of field, which is 120 degrees out of phase with the field generated by the other conductors. These powerline characteristics can be observed in Figure 13.6.

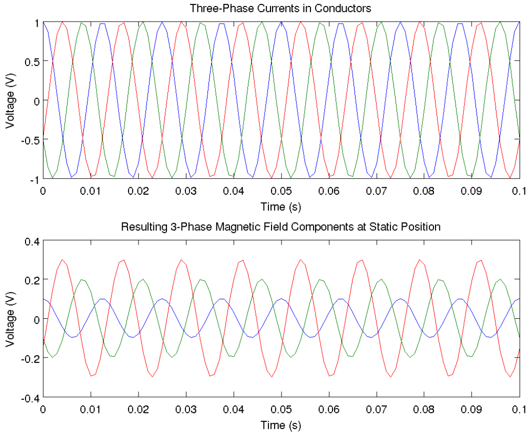

Figure 13.6: Three Phase Current and Magnetic Field Components

Fortunately, this phenomena can be approached in the same manner as a two-conductor system whose wires are 180 degrees out of phase. By carrying out the mathematics in the complex plane, it can be observed that the magnetic field generated by a three-phase current system is actually only single phase.

From Figure 13.6, one can see how the magnetic field generated by a three phase current system at a single point in space can be represented in phasor notation as

$$B = ae^{\Theta_1} + be^{i\Theta_2} + ce^{i\Theta_3} \tag{13.8}$$

Where a, b, and c represent the peak field magnitude contributed by each of the three wires, and the phases, Θ_1 Θ_2 Θ_3 are 0, $\frac{2\pi}{3}$, and $\frac{4\pi}{3}$ respectively.

This field can then be represented in the complex plane as :

$$B = (a\cos\Theta_1 + b\cos\Theta_2 + c\cos\Theta_3) + (a\sin\Theta_1 + b\sin\Theta_2 + c\sin\Theta_3)i \tag{13.9}$$

We now can transform this complex vector back into a phasor as follows:

$$|B| = \sqrt{(a\cos\Theta_1 + b\cos\Theta_2 + c\cos\Theta_3)^2 + (a\sin\Theta_1 + b\sin\Theta_2 + c\sin\Theta_3)^2} \tag{13.10}$$

$$\angle B = \Phi = atan(\frac{a\sin\Theta_1 + b\sin\Theta_2 + c\sin\Theta_3}{a\cos\Theta_1 + b\cos\Theta_2 + c\cos\Theta_3}) \tag{13.11}$$

Substituting in for Θ_1, Θ_2, and Θ_3 then yields:

$$|B| = \sqrt{(a + (b+c)(-\frac{1}{2}))^2 + ((b-c)\sqrt{\frac{3}{2}})^2} \tag{13.12}$$

$$\angle B = \Phi = atan(\frac{(b-c)\sqrt{\frac{3}{2}}}{a + (b+c)(\frac{1}{2})}) \tag{13.13}$$

The single phase magnetic field signal can now be written as:

$$B = |B|cos(\omega t + \Phi); \tag{13.14}$$

13.3 Interference from Motors

To move from indoor to outdoor experiments, a propeller will most certainly be necessary to reject wind gusts. It is highly likely that the DC brushless motor used to drive this propeller will create a magnetic field which will interfere with magnetometer-based state estimation. There are two ways one might be able to go about addressing this problem. The first would involve building a model of the the magnetic field generated by the motor and incorporate this model into the state estimator. Although this may seem complicated, it might prove to be practical. The magnetic field of the motor could be modeled as a function of the motor commands, and these commands could then be fed into the state estimator to correct the position measurements. It could be the case that at very far distances from the wire, the magnetic field from the motor might completely overpower the field from the powerline. A clever solution for this might be to turn off the motor for the initial approach and then turn it on when the aircraft is close to the wire- just when the magnetic field from the wire begins to dominate the signal. Since the aircraft will be most vulnerable at the end of the perching trajectory, only using the propeller when needed might prevent unnecessary interference at far distances from the wire.

Chapter 14

Conclusion and Future Work

By systemically answering four research questions, this thesis has demonstrated that it is possible to track an aircraft during a perching maneuver using the magnetic field generated by a powerline, even when the signal values are extremely low. It has also shown, through simulation, that the position measurement distortions inherent in the system should not impact the accuracy of the closed loop perching algorithms if the x-coordinate velocities are underestimated. Moreover, by using the real and imaginary components output by the complex synchronous demodulation algorithm, and by writing the measurement model such that all magnetometer axes have the same phase, it has been demonstrated that the aircraft can be robustly tracked with only a double integrator process model. This is a substantial advantage since disturbances to the process model, such as wind gusts will not adversely affect the state estimation.

Another key advantage of the method outlined in this thesis is in the system architecture. By separating the demodulation process and the state estimation process, the system architecture outlined in this thesis has allowed for high fidelity sinusoidal signal measurement as well as the online implementation of estimation algorithms at reasonable update rates. The estimation algorithms can be executed at rates on the order of the system dynamics while the synchronous demodulation can be executed on a DSP above the required rate of 4x the carrier frequency.

In addition to the magnetic field-based state estimation, this thesis has also shown that by generating a standard system modeling method for the perching aircraft, a nonlinear perching controller can be generated for an aircraft with varying mass parameters. This is important because the electronics change the weight, inertia, and center of mass enough to cause the original controller to fail. By ensuring that the aircraft can perch with onboard electronics, this thesis has made a significant step towards generalizing the original perching control algorithms for arbitrary aircrafts.

In the future, one goal of this work is to finally close the loop on the fixed-wing perching maneuver using magnetic field measurements. Once this has been accomplished indoors, the next goal is to transition to outdoor perching experiments. Outdoor flight will provide for a number of interesting investigations into wind gust rejection and the development of controllers which will reason about the stochastic nature of the disturbances. Another important future task will be using the magnetic field sensing system in the vicinity of an DC brushless aircraft motor. As mentioned previously, transitioning to outdoor flight will inevitably require the use of the propeller, and this will no doubt add interference to the magnetic field measurements. Whether or not this interference can be shielded effectively or compensated for has yet to be determined.

Appendix A

Magnetic Sensing Schematics

This appendix contains the GOSHAWK magnetic sensing board schematics.

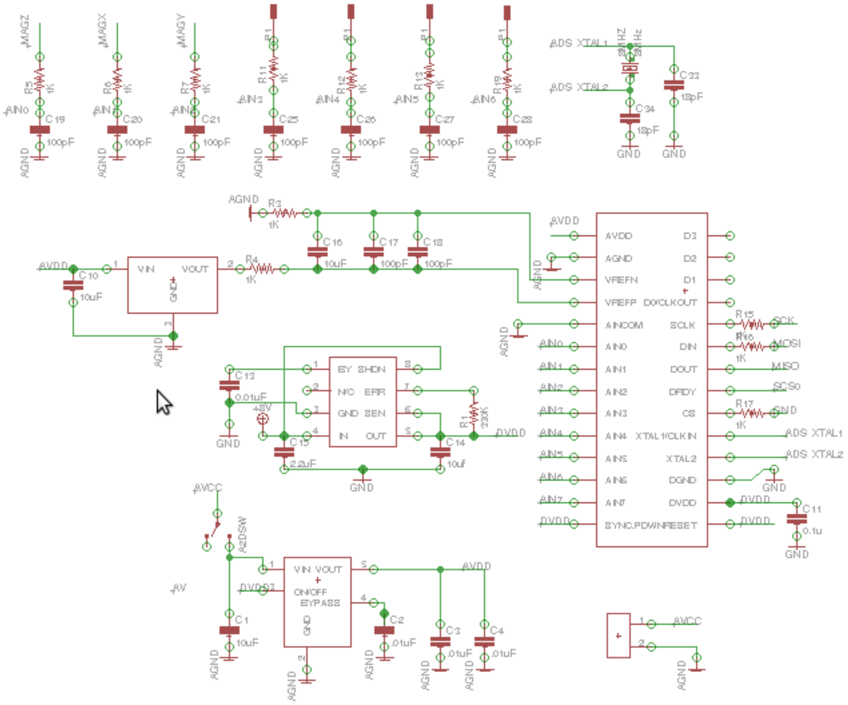

Figure A.1: Analog to Digital Converter and Supporting Circuitry

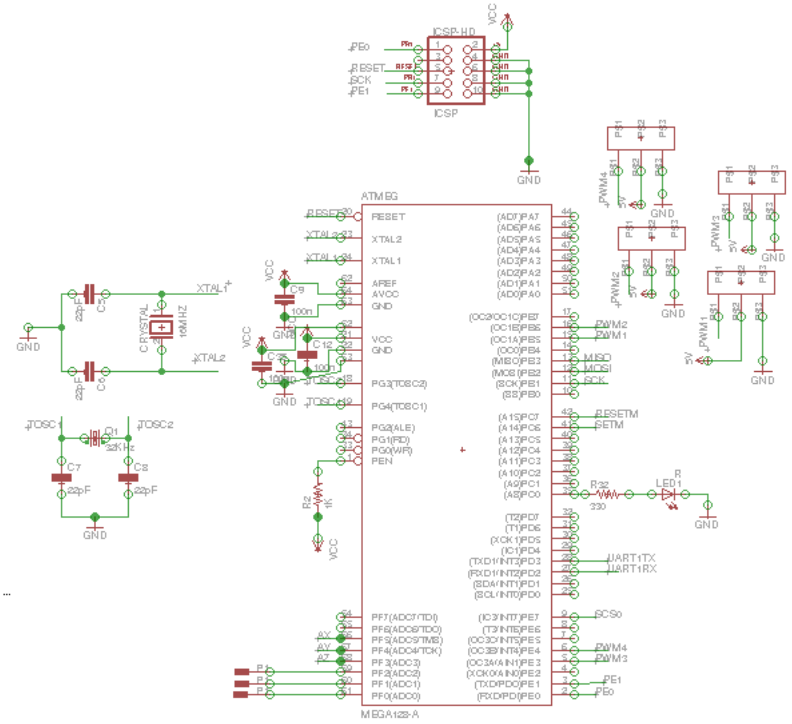

Figure A.2: ATMEGA Microcontroller Supporting Circuitry

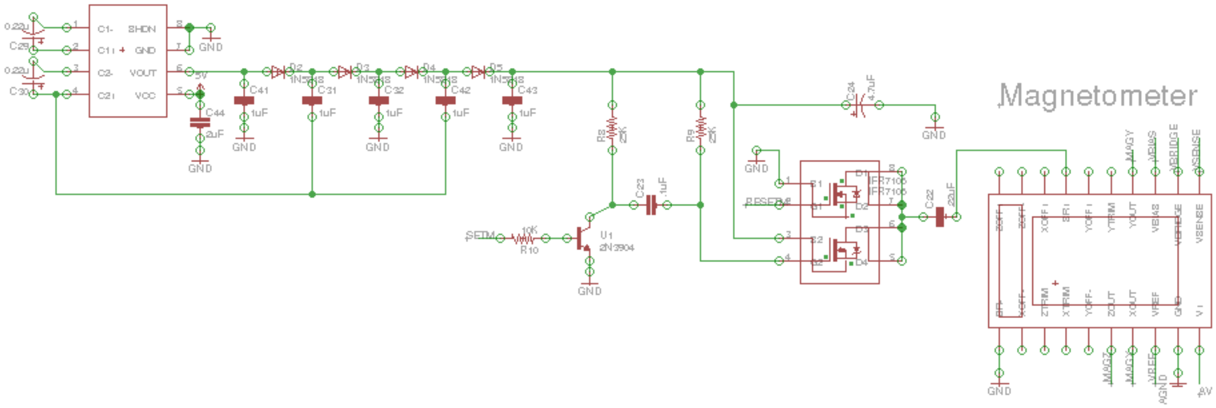

Figure A.3: Magnetometer Supporting Circuitry

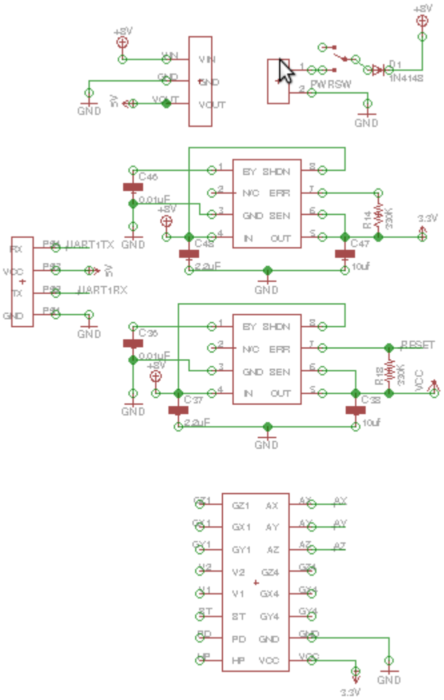

Figure A.4: Power Supply Circuitry

Appendix B

Rectangular Current Loop Magnetic Field Model Derivation

To model the rectangular current loop, we use the Biot-Savart law which is given as,

$$\mathbf{B} = \int \frac{\mu_0 I d\mathbf{l} \times \mathbf{r}}{4\pi r^3} \tag{B.1}$$

where μ_0 is the magnetic permeability of free space, I is the current in the wire, $\mathbf{l}$ is the vector from the origin of the wire to the infinitesimal wire segment of interest in the direction of the current, and $\mathbf{r}$ is the vector from the infinitesimal wire segment to the aircraft location.

B.1 Wire 1

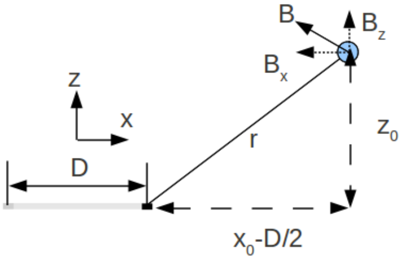

Figure B.1: Side View of Rectangular Current Loop

To model the field from the first wire, we use Figures B.1 and B.2. In these figures, x_0, y_0, and z_0 define the position of the aircraft, and $\hat{\mathbf{i}}$, $\hat{\mathbf{j}}$, and $\hat{\mathbf{k}}$ represent the Cartesian unit

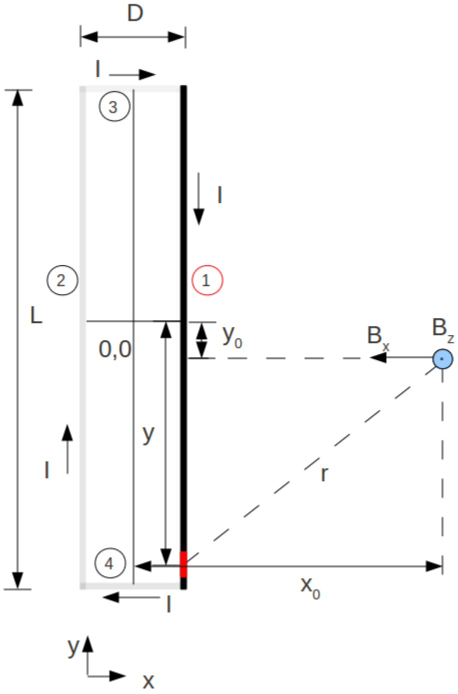

Figure B.2: Top View of Wire 1 Analysis

vectors. as shown in Figure B.2

$$\mathbf{l} = -y\hat{\mathbf{j}} \tag{B.2}$$

$$d\mathbf{l} = -dy\hat{\mathbf{j}} \tag{B.3}$$

$$\mathbf{r} = (x_0 - \tfrac{D}{2})\hat{\mathbf{i}} + (y_0 - y)\hat{\mathbf{j}} + z_0\hat{\mathbf{k}} \tag{B.4}$$

$$d\mathbf{l} \times \mathbf{r} = (-z_0\hat{\mathbf{i}} + (x_0 - \tfrac{D}{2})\hat{\mathbf{k}})dy \tag{B.5}$$

Substituting into the Biot-Savart Integral gives,

$$\mathbf{B_1} = \int_{-\frac{L}{2}}^{\frac{L}{2}} \frac{\mu_0 I(-z_0\hat{\mathbf{i}} + (x_0 - \frac{D}{2})\hat{\mathbf{k}})dy}{4\pi(\sqrt{(x_0 - \frac{D}{2})^2 + (y_0 - y)^2 + z_0^2})^3} \tag{B.6}$$

For simplicity, let

$$H = \frac{\mu_0 I}{4\pi} \tag{B.7}$$

We can separate the vector field $\mathbf{B_1}$ into its x and z components as follows:

$$B_{x,1} = \int_{-\frac{L}{2}}^{\frac{L}{2}} \frac{-Hz_0dy}{(\sqrt{(x_0 - \frac{D}{2})^2 + (y_0 - y)^2 + z_0^2})^3} \tag{B.8}$$

$$B_{z,1} = \int_{-\frac{L}{2}}^{\frac{L}{2}} \frac{H(x_0 - \frac{D}{2})dy}{(\sqrt{(x_0 - \frac{D}{2})^2 + (y_0 - y)^2 + z_0^2})^3} \tag{B.9}$$

Since we know the integral relation

$$\int \frac{dX}{(\sqrt{a^2 + X^2})^3} = \frac{X}{a^2\sqrt{a^2 + X^2}} + C \tag{B.10}$$

We can let

$$X = (y_0 - y) \tag{B.11}$$

$$dX = -dy \tag{B.12}$$

$$a^2 = \left(x_0 - \frac{D}{2}\right)^2 + z_0^2 \tag{B.13}$$

and solve for the integrals analytically as follows:

$$B_{x,1} = \left[\frac{Hz_0(y_0 - y)}{((x_0 - \frac{D}{2})^2 + z_0^2)\sqrt{(x_0 - \frac{D}{2})^2 + (y_0 - y)^2 + z_0^2}}\right]_{-\frac{L}{2}}^{\frac{L}{2}} \tag{B.14}$$

$$B_{z,1} = \left[\frac{-H(x_0 - \frac{D}{2})(y_0 - y)}{((x_0 - \frac{D}{2})^2 + z_0^2)\sqrt{(x_0 - \frac{D}{2})^2 + (y_0 - y)^2 + z_0^2}}\right]_{-\frac{L}{2}}^{\frac{L}{2}} \tag{B.15}$$

Evaluating the bounds yields

$$B_{x,1} = \frac{Hz_0}{z_0^2 + (x_0 - \frac{D}{2})^2} M_1 \tag{B.16}$$

$$B_{z,1} = \frac{-H(x_0 - \frac{D}{2})}{z_0^2 + (x_0 - \frac{D}{2})^2} M_1 \tag{B.17}$$

where M_1 equals

$$M_1 = \frac{(y_0 - \frac{L}{2})}{\sqrt{(x_0 - \frac{D}{2})^2 + (y_0 - \frac{L}{2})^2 + z_0^2}} - \frac{(y_0 + \frac{L}{2})}{\sqrt{(x_0 - \frac{D}{2})^2 + (y_0 + \frac{L}{2})^2 + z_0^2}} \tag{B.18}$$

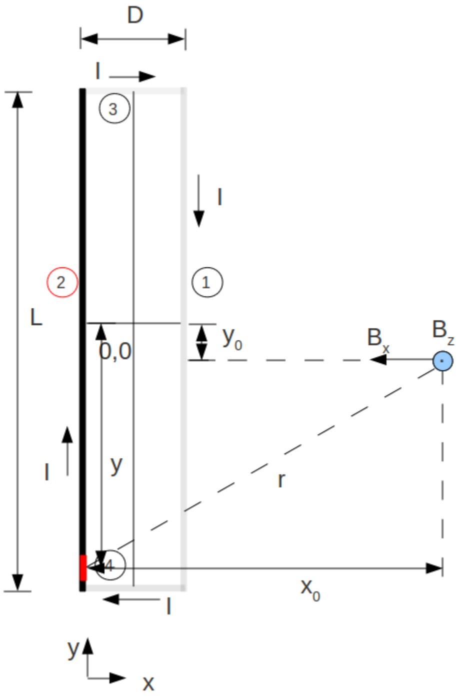

Figure B.3: Top View of Wire 2 Analysis

B.2 Wire 2

For for the second wire, we use Figure B.3 and let

$$\mathbf{l} = y\hat{\mathbf{j}} \tag{B.19}$$

$$d\mathbf{l} = dy\hat{\mathbf{j}} \tag{B.20}$$

$$\mathbf{r} = (x_0 + \tfrac{D}{2})\hat{\mathbf{i}} + (y_0 - y)\hat{\mathbf{j}} + z_0\hat{\mathbf{k}} \tag{B.21}$$

$$d\mathbf{l} \times \mathbf{r} = (z_0\hat{\mathbf{i}} - (x_0 + \tfrac{D}{2})\hat{\mathbf{k}})dy \tag{B.22}$$

Then, substitute into the Biot-Savart law to get

$$\mathbf{B_2} = \int_{-\frac{L}{2}}^{\frac{L}{2}} \frac{H(z_0\hat{\mathbf{i}} - (x_0 + \frac{D}{2})\hat{\mathbf{k}})dy}{(\sqrt{(x_0 + \frac{D}{2})^2 + (y_0 - y)^2 + z_0^2})^3} \tag{B.23}$$

Separating this vector field into two components yields

$$B_{x,2} = \int_{-\frac{L}{2}}^{\frac{L}{2}} \frac{Hz_0dy}{(\sqrt{(x_0 + \frac{D}{2})^2 + (y_0 - y)^2 + z_0^2})^3} \tag{B.24}$$

$$B_{z,2} = \int_{-\frac{L}{2}}^{\frac{L}{2}} \frac{-H(x_0 + \frac{D}{2})dy}{(\sqrt{(x_0 + \frac{D}{2})^2 + (y_0 - y)^2 + z_0^2})^3} \tag{B.25}$$

Using the integral relation in B.10, let

$$X = (y_0 - y) \tag{B.26}$$

$$dX = -dy \tag{B.27}$$

$$a^2 = \left(x_0 + \frac{D}{2}\right)^2 + z_0^2 \tag{B.28}$$

Substituting into the integral relation gives

$$B_{x,2} = \left[\frac{-Hz_0(y_0 - y)}{((x_0 + \frac{D}{2})^2 + z_0^2)\sqrt{(x_0 + \frac{D}{2})^2 + (y_0 - y)^2 + z_0^2}} \right]_{-\frac{L}{2}}^{\frac{L}{2}} \tag{B.29}$$

$$B_{z,2} = \left[\frac{H(x_0 + \frac{D}{2})(y_0 - y)}{((x_0 + \frac{D}{2})^2 + z_0^2)\sqrt{(x_0 + \frac{D}{2})^2 + (y_0 - y)^2 + z_0^2}} \right]_{-\frac{L}{2}}^{\frac{L}{2}} \tag{B.30}$$

Finally, evaluating over the bounds yields

$$B_{x,2} = \frac{-Hz_0}{z_0^2 + (x_0 + \frac{D}{2})^2} M_2 \tag{B.31}$$

$$B_{z,2} = \frac{H(x_0 + \frac{D}{2})}{z_0^2 + (x_0 + \frac{D}{2})^2} M_2 \tag{B.32}$$

where M_2 equals

$$M_2 = \frac{(y_0 - \frac{L}{2})}{\sqrt{(x_0 + \frac{D}{2})^2 + (y_0 - \frac{L}{2})^2 + z_0^2}} - \frac{(y_0 + \frac{L}{2})}{\sqrt{(x_0 + \frac{D}{2})^2 + (y_0 + \frac{L}{2})^2 + z_0^2}} \tag{B.33}$$

B.3 Wire 3

For for the third wire, we use Figure B.4 and let

$$\mathbf{l} = -x\hat{\mathbf{i}} \tag{B.34}$$

$$d\mathbf{l} = -dx\hat{\mathbf{i}} \tag{B.35}$$

$$\mathbf{r} = (x_0 - x)\hat{\mathbf{i}} + (y_0 + \tfrac{L}{2})\hat{\mathbf{j}} + z_0\hat{\mathbf{k}} \tag{B.36}$$

$$d\mathbf{l} \times \mathbf{r} = (z_0\hat{\mathbf{i}} - (y_0 + \tfrac{L}{2})\hat{\mathbf{k}})dy \tag{B.37}$$

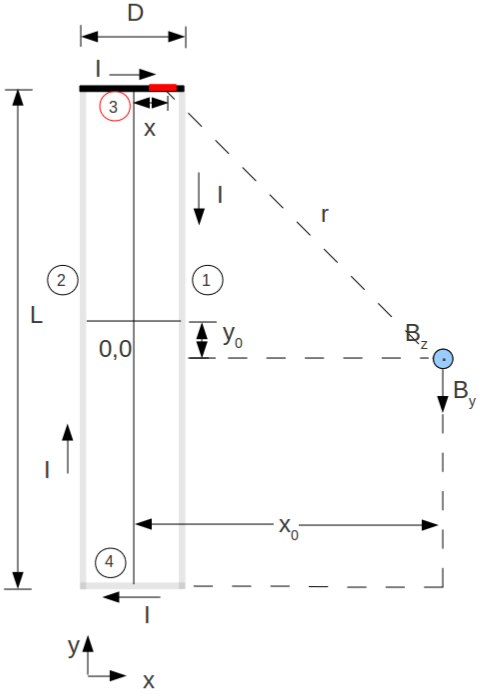

Figure B.4: Top View of Wire 3 Analysis

Then, substitute into the Biot-Savart law to get

$$\mathbf{B_3} = \int_{-\frac{D}{2}}^{\frac{D}{2}} \frac{H(z_0\hat{\mathbf{j}} - (y_0 + \frac{L}{2})\hat{\mathbf{k}})dx}{(\sqrt{(x_0 - x)^2 + (y_0 + \frac{L}{2})^2 + z_0^2})^3} \tag{B.38}$$

Separating this vector field into two components yields

$$B_{y,3} = \int_{-\frac{D}{2}}^{\frac{D}{2}} \frac{Hz_0dx}{(\sqrt{(x_0 - x)^2 + (y_0 + \frac{L}{2})^2 + z_0^2})^3} \tag{B.39}$$

$$B_{z,3} = \int_{-\frac{D}{2}}^{\frac{D}{2}} \frac{-H(y_0 + \frac{L}{2})dx}{(\sqrt{(x_0 - x)^2 + (y_0 + \frac{L}{2})^2 + z_0^2})^3} \tag{B.40}$$

Again, use the integral relation by letting

$$X = (x_0 - x) \tag{B.41}$$

$$dX = -dx \tag{B.42}$$

$$a^2 = \left(y_0 + \frac{L}{2}\right)^2 + z_0^2 \tag{B.43}$$

Substituting into the integral relation yields:

$$B_{y,3} = \left[\frac{-Hz_0(x_0 - x)}{((y_0 + \frac{L}{2})^2 + z_0^2)\sqrt{(x_0 - x)^2 + (y_0 + \frac{L}{2})^2 + z_0^2}} \right]_{-\frac{D}{2}}^{\frac{D}{2}} \tag{B.44}$$

$$B_{z,3} = \left[\frac{H(y_0 + \frac{L}{2})(x_0 - x)}{((y_0 + \frac{L}{2})^2 + z_0^2)\sqrt{(x_0 - x)^2 + (y_0 + \frac{L}{2})^2 + z_0^2}} \right]_{-\frac{D}{2}}^{\frac{D}{2}} \tag{B.45}$$

Evaluating the bounds yields

$$B_{y,3} = \frac{-Hz_0}{z_0^2 + (y_0 + \frac{L}{2})^2} M_3 \tag{B.46}$$

$$B_{z,3} = \frac{H(y_0 + \frac{L}{2})}{z_0^2 + (y_0 + \frac{L}{2})^2} M_3 \tag{B.47}$$

where M_3 equals

$$M_3 = \frac{(x_0 - \frac{D}{2})}{\sqrt{(x_0 - \frac{D}{2})^2 + (y_0 + \frac{L}{2})^2 + z_0^2}} - \frac{(x_0 + \frac{D}{2})}{\sqrt{(x_0 + \frac{D}{2})^2 + (y_0 + \frac{L}{2})^2 + z_0^2}} \tag{B.48}$$

B.4 Wire 4

For for the fourth wire, we use Figure B.5 and let

$$\mathbf{l} = x\hat{\mathbf{i}} \tag{B.49}$$

$$d\mathbf{l} = dx\hat{\mathbf{i}} \tag{B.50}$$

$$\mathbf{r} = (x_0 - x)\hat{\mathbf{i}} + (y_0 - \tfrac{L}{2})\hat{\mathbf{j}} + z_0\hat{\mathbf{k}} \tag{B.51}$$

$$d\mathbf{l} \times \mathbf{r} = (-z_0\hat{\mathbf{i}} + (y_0 - \tfrac{L}{2})\hat{\mathbf{k}})dy \tag{B.52}$$

Then, substitute into the Biot-Savart law to get

$$\mathbf{B_4} = \int_{-\frac{D}{2}}^{\frac{D}{2}} \frac{H(-z_0\hat{\mathbf{j}} + (y_0 - \frac{L}{2})\hat{\mathbf{k}})dx}{(\sqrt{(x_0 - x)^2 + (y_0 - \frac{L}{2})^2 + z_0^2})^3} \tag{B.53}$$

Separating the vector field into components yields

$$B_{y,4} = \int_{-\frac{D}{2}}^{\frac{D}{2}} \frac{-Hz_0 dx}{(\sqrt{(x_0 - x)^2 + (y_0 - \frac{L}{2})^2 + z_0^2})^3} \tag{B.54}$$

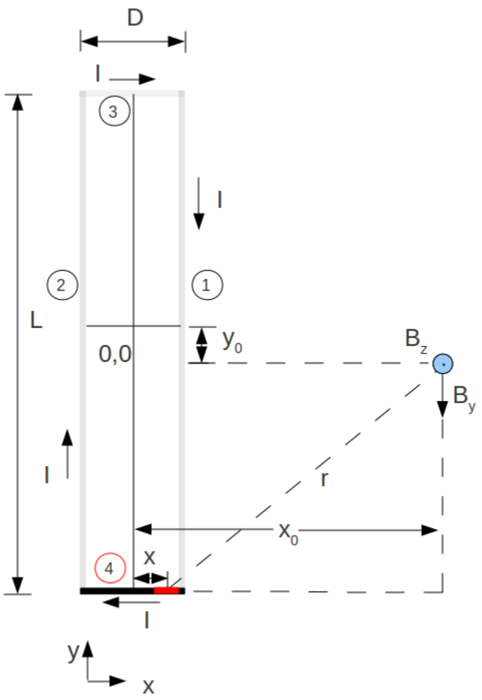

Figure B.5: Top View of Wire 4 Analysis

$$B_{z,4} = \int_{-\frac{D}{2}}^{\frac{D}{2}} \frac{H(y_0-\frac{L}{2})dx}{(\sqrt{(x_0-x)^2+(y_0-\frac{L}{2})^2+z_0^2})^3} \tag{B.55}$$

Employing the integral relation, let

$$X = (x_0 - x) \tag{B.56}$$

$$dX = -dx \tag{B.57}$$

$$a^2 = \left(y_0 - \frac{L}{2}\right)^2 + z_0^2 \tag{B.58}$$

Substituting in to the integral relation yields:

$$B_{y,4} = \left[\frac{Hz_0(x_0-x)}{((y_0-\frac{L}{2})^2+z_0^2)\sqrt{(x_0-x)^2+(y_0-\frac{L}{2})^2+z_0^2}}\right]_{-\frac{D}{2}}^{\frac{D}{2}} \tag{B.59}$$

$$B_{z,4} = \left[\frac{-H(y_0-\frac{L}{2})(x_0-x)}{((y_0-\frac{L}{2})^2+z_0^2)\sqrt{(x_0-x)^2+(y_0-\frac{L}{2})^2+z_0^2}}\right]_{-\frac{D}{2}}^{\frac{D}{2}} \tag{B.60}$$

Evaluating the bounds yields:

$$B_{y,4} = \frac{Hz_0}{z_0^2 + (y_0 - \frac{L}{2})^2} M_4 \tag{B.61}$$

$$B_{z,4} = \frac{-H(y_0 - \frac{L}{2})}{z_0^2 + (y_0 - \frac{L}{2})^2} M_4 \tag{B.62}$$

where M_4 equals

$$M_4 = \frac{(x_0 - \frac{D}{2})}{\sqrt{(x_0 - \frac{D}{2})^2 + (y_0 - \frac{L}{2})^2 + z_0^2}} - \frac{(x_0 + \frac{D}{2})}{\sqrt{(x_0 + \frac{D}{2})^2 + (y_0 - \frac{L}{2})^2 + z_0^2}} \tag{B.63}$$

The full magnetic field equations then become

$$B_x = B_{x,1} + B_{x,2} \tag{B.64}$$

$$B_y = B_{y,3} + B_{y,4} \tag{B.65}$$

$$B_z = B_{z,1} + B_{z,2} + B_{z,3} + B_{z,4} \tag{B.66}$$

Last of all, we must take into consideration the rotation of the sensor, where R_ϕ is the rotation matrix representing roll, R_θ represents pitch, and R_ψ represents yaw.

$$\mathbf{B'} = R_\phi R_\theta R_\psi \vec{B} \tag{B.67}$$

Bibliography

[1] Lamont V. Blake. *Antennas.* John Wiley and Sons, 1966.

[2] Steven W. Blume. *Electric Power System Basics.* Institute of Electrical and Electronics Engineers, 2007.

[3] Theodore R. Bosela. *Introduction to Electrical Power System Technology.* Prentice-Hall, 1997.

[4] Michael J. Caruso, Tamara Bratlant, Carl H. Smith, and Rober Schneider. A new prospective on magnetic field sensing. *Honeywell*, May 1998.

[5] Salvatore Celozzi, Rodolfo Araneo, and Giampiero Lovat. *Electromagnetic Shielding.* John Wiley and Sons, 2008.

[6] Rick Cory and Russ Tedrake. Experiments in fixed-wing UAV perching. In *Proceedings of the AIAA Guidance, Navigation, and Control Conference.* AIAA, 2008.

[7] Rick Cory and Russ Tedrake. Landing on a dime: control of bird-inspired perching manoeuvres for fixed-wing aircraft. *Submitted to (IOP) Biomimetics & Bioinspiration Special Issue on Bioinspired Flight*, 2010.

[8] Alexis Lussier Desbiens, Alan Asbeck, and Mark Cutkosky. Hybrid aerial and scansorial robotics. *ICRA*, May 2010.

[9] G. Frulla. Preliminary reliability design of a solar-powered high-altitude very long endurance unmanned air vehicle. *Journal of Aerospace Engineering*, 216, 2002.

[10] Alberto Geri, Ambrogio Locatelli, and Giuseppe Maria Veca. Magnetic fields generated by power lines. *Transactions on Magnetics*, 31(3):1508–1511, May 1995.

[11] Gordon, N.J.; Salmond, and D.J.; Smith. Novel approach to nonlinear/non-Gaussian Bayesian state estimation. *IEE Proceedings F Radar and Signal Processing*, 140(2):107–113, April 1993.

[12] Michael Guillory. The complete uav field guide: Know your reapers from your global hawks. *Popular Science*, February 2010.

[13] Adam Hadhazy. Air force invests in 'batman' technologies for special forces. *TechNewsDaily*, January 2011.

[14] Alfred Hine. *Magnetic Compasses and Magnetometers.* Higler, 1968.

[15] Warren Hoburg, John William Roberts, Joseph Moore, and Russ Tedrake. The perching number: A dimensionless analysis of post-stall maneuvering in birds and planes. *Working Draft*, 2009.

[16] Warren Hoburg and Russ Tedrake. System identification of post stall aerodynamics for UAV perching. In *Proceedings of the AIAA Infotech@Aerospace Conference*, Seattle, WA, April 2009. AIAA.

[17] Honeywell. Magnetoresistive sensors industry: Position and solid state sensing. Application Note, 2003.

[18] Honeywell. Three-axis magnetic sensor hybrid. Specfications Document, Rev. E, 2004.

[19] Albert S. Huang, Edwin Olson, and David C. Moore. Lcm: Lightweight communications and marshalling. *International Conference on Intelligent Robots and Systems (IROS), 2010 IEEE/RSJ*, pages 4057–4062, October 2010.

[20] S. J. Julier and J.K. Uhlmann. A general method for approximating nonlinear transformations of probability distributions. 1994.

[21] S.J. Julier and J.K. Uhlmann. A new extension of the kalman filter to nonlinear systems. In *Proceedings of AeroSense: The 11th International Symposium of Aerospace/Defense Sensing, Simulation and Controls*, April 1997.

[22] Kalman, Rudolph, and Emil. A new approach to linear filtering and prediction problems. *Transactions of the ASME–Journal of Basic Engineering*, 82(Series D):35–45, 1960.

[23] Joseph F. Keithley. *The Story of Electrical and Magnetic Measurements.* IEEE Press, 1999.

[24] James E. Lenz. A review of magnetic sensors. *Proceedings of the IEEE*, 78(6), June 1990.

[25] A.V. Mamishev and B.D. Russell. Measurement of magnetic fields in the direct proximity of power line conductors. *IEEE Transactions of Power Delivery*, 10(3):1211–1216, July 1995.

[26] Philippe Martin and Erwan Salaun. Invariant observers for attitude and heading estimation from low cost inertial and magnetic sensors. *Proceedings of the IEEE on Decision and Control*, December 2007.

[27] Daniel C Mattis. *The Theory of Magnetism Made Simple.* World Scientific, March 2006.

[28] Thomas H. Maugh. Victor vacquier sr. dies at 101; geophysicist was a master of magnetics. *Los Angeles Times*, January 2009.

[29] Joseph Moore and Russ Tedrake. Powerline perching with a fixed-wing UAV. In *Proceedings of the AIAA Infotech@Aerospace Conference*, Seattle, WA, April 2009. AIAA.

[30] Joseph Moore and Russ Tedrake. Magnetic localization for perching uavs on powerlines. *Under Review*, September 2011.

[31] A.V. Oppenheim, A.S. Willsky, and S. Hamid. *Signals and Systems.* Prentice Hall, 2nd edition, August 1996.

[32] Henry W. Ott. *Electromagnetic Compatibility Engineering.* John Wiley and Sons, 2009.

[33] Clayton R. Paul. *Introduction to Electromagnetic Compatibility.* John Wiley and Sons, 2006.

[34] Eric A. Prigge and Johnathan P. How. Signal architecture for a distributed magnetic local positioning system. *IEEE Sensors Journal*, 4(6), December 2004.

[35] Mark L. Psiaki, Francois Martel, and Parimal K. Pal. Three-axis attitude determination via kalman filtering of magnetometer data. *Guidance, Navigation and Control*, 13(3):506–514, May 1989.

[36] Kitt C. Reinhardt, Thomas R. Lamp, and Jack W. Geis. Solar-powered unmanned aerial vehicles. *Energy Conversion Engineering Conference*, 1996.

[37] Philipp Reist and Russ Tedrake. Simulation-based LQR-trees with input and state constraints. In *Proceedings of the International Conference on Robotics and Automation (ICRA)*, 2010.

[38] John W. Roberts, Rick Cory, and Russ Tedrake. On the controllability of fixed-wing perching. In *Proceedings of the American Controls Conference (ACC)*, 2009.

[39] J. J. Rodden and L. D. Montague. Design of an attitude control system with magnetometer sensors. *American Institute of Aeronautics and Astronautics*, 1(6):1422–1424, 1962.

[40] Stanley F. Schmidt. The kalman filter: Its recognition and development for aerospace applications. *American Institute of Aeronautics and Astronautics*, 1980.

[41] K. Sigurd and J. How. Uav trajectory design using total field collision avoidance. In *AIAA Guidance, Navigation, and Control Conference and Exhibit*, August 11-14 2003.

[42] H.W. Sorenson. Least-squares estimation from gauss to kalman. *IEEE Spectrum*, July 1970.

[43] Russ Tedrake. LQR-Trees: Feedback motion planning on sparse randomized trees. In *Proceedings of Robotics: Science and Systems (RSS)*, page 8, 2009.

[44] Russ Tedrake, Ian R. Manchester, Mark M. Tobenkin, and John W. Roberts. LQR-Trees: Feedback motion planning via sums of squares verification. *International Journal of Robotics Research*, 29:1038–1052, July 2010.

[45] S. Thrun, W. Burgard, and D. Fox. *Probabilistic Robotics.* MIT Press, 2005.

[46] Barry E. Tossman. Magnetic attitude control system for the radio astronomy explorer-a satellite. *Spacecraft and Rockets*, 6(3):239–244, 1969.

[47] Fawwaz T. Ulaby. *Fundamentals of Applied Electromagnetics.* Prentice-Hall, 1999.

[48] K. Wassef, V.V. Varadan, and V.K. Varadan. Magnetic field shielding concepts for power transmission lines. *IEEE Transactions on Magnetics*, 34:649, May 1998.

[49] John M. Wharington. Heuristic control of dynamic soaring. *5th Asian Control Conference*, 2005.

[50] Adam M. Wickenheiser and Ephrahim Garcia. Longitudinal dynamics of a perching aircraft. *Journal of Aircraft*, 43(5):1386–1392, 2006.

[51] Adam M. Wickenheiser and Ephrahim Garcia. Optimization of perching maneuvers through vehicle morphing. *Journal of Guidance, Control, and Dynamics*, 31(4):815–824, July-August 2008.

[52] Norbert Wiener. *Extrapolation, Interpolation, and Smoothing of Stationary Time Series.* New York: Wiley, 1949.